CONCEPTUAL FORMULATION FOR CRACK MAPPING PREDICTION USING STOCHASTIC MODELLING

CHUAH PEI LIM

A project report submitted in partial fulfilment of the requirements for the award of Bachelor of Engineering (Honours) Civil Engineering

Lee Kong Chian Faculty of Engineering and Science
Universiti Tunku Abdul Rahman

April 2021

DECLARATION

I hereby declare that this project report is based on my original work except for citations and quotations which have been duly acknowledged. I also declare that it has not been previously and concurrently submitted for any other degree or award at UTAR or other institutions.

Signature :

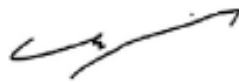Name   : CHUAH PEI LIM

ID No.   : 16UEB02974

Date   : 6 MAY 2021

APPROVAL FOR SUBMISSION

I certify that this project report entitled **CONCEPTUAL FORMULATION FOR CRACK MAPPING PREDICTION USING STOCHASTIC MODELLING** was prepared by **CHUAH PEI LIM** has met the required standard for submission in partial fulfilment of the requirements for the award of Bachelor of Engineering (Honours) Civil Engineering at Universiti Tunku Abdul Rahman.

Approved by,

Signature   :

Supervisor   :   IR TS DR. KWONG KOK ZEE

Date   :   7 MAY 2021

ACKNOWLEDGEMENTS

ABSTRACT

Non-destructive testing (NDT) is an analysis method employed to assess material or structure properties without causing damage to the part. The Impact-echo method is widely used in the construction field, featuring Rayleigh wave and pressure wave exploitation. Although the evaluation of concrete defection has been carried out using NDT, the crack mapping model is rarely used due to the infantile methodology. Hence, this study aims to develop an integrated three-dimensional crack mapping prediction model using stochastic processes. In this study, the elastic wave propagation in a concrete medium was replicated using the Delta method and ABAQUS simulation. The proposed crack mapping model included ellipse-based interpolation and beta reflection methods for surface and cross-section analysis. The surface crack mapping identifies the crack's location and provides variance of wave velocities (beta value). The cross-section analysis correlates to the beta value showing a three-dimensional crack mapping prediction model with corresponding depth. The simulation result from the crack mapping model agrees well with the theoretical sample with the slightest discrepancies. This finding also considered the heterogeneity properties of concrete, which exhibits the lognormal distribution of Young's modulus and Poisson ratio. Both deterministic and stochastic results confirmed that the model has high reliability to detect the concrete flaw despite the random distribution of engineering properties. In a nutshell, the conception formulation for crack mapping predicting using stochastic modelling is developed with higher accuracy and the least iterations of NDT needed.

TABLE OF CONTENTS

LIST OF TABLES

LIST OF FIGURES

LIST OF SYMBOLS / ABBREVIATIONS

E	Modulus of elasticity, GPa
ρ	Density, kg/m^3
v	Poisson's Ratio
f	Frequency, Hz
λ_k	Eigenvalues of the covariance matrix
ψ_k	Eigenvectors of the covariance matrix
C_{xg}	Vector to the centre of the surface
ξ	Independent standard normal variables
λ	First lame constant, GPa
μ	Second lame constant, GPa
β	Beta Value (Variance between Velocities)
DT	Destructive Test
NDT	Non-destructive test
IE	Impact-Echo
SEC	Soft Elastomeric Capacitor
SAFT	Synthetic Aperture Focusing Technique
2D	Two-dimension
3D	Three Dimension
ASTM	American Society for Testing and Material
SIBIE	Stack Imaging based on Impact-Echo
R-wave	Rayleigh Wave
P-wave	Pressure Wave
S-wave	Shear Wave
FFT	Fast Fourier Transform

LIST OF APPENDICES

CHAPTER 1

INTRODUCTION

1.1   General Introduction

Concrete is extensively employed in the construction field as it produces the lowest carbon footprint for a building structure over its lifecycle and provides high durability regardless of the surrounding condition. In the reinforcement concrete structure, concrete gives the compressive strength on the actual load-bearing capacity and cover to provide inherent protection over the rebars from the corrosion attack.

Concrete surfaces are vulnerable to crack at any stage over the lifecycle. The concrete crack seldom directly causes structural failure of the building structure. It generally creates some detrimental effect on the serviceability of concrete where the appearance and the reassurance of occupants are affected. For example, the leakage from the roof might cause some discomfort to the occupants. However, if the crack of concrete is left unchecked, it may lead to long-term maintenance issues. The cracking of concrete gives rise to the carbonation and chloride attack that cause corrosion of the reinforcement bar. Steel corrosion is considered the biggest durability problem for reinforcement structures. The damage affects the integrity and aesthetics of all types of structures, such as beam, column, slab, and wall. Therefore, it is essential to regularly inspect the building structure on the defection to evaluate its serviceability.

The slab is the most dominant element in the typical reinforced concrete structure, where it develops more than 60 % of the building construction (Building and Constuction Authority, 2012). Hence, appropriate crack detection and monitoring of the slab element are vital to optimize a building's serviceability. Cracking can arise when the slabs are wholly loaded. Overloading issues might cause the crack during the construction stage due to self-weight without the support by the scaffold. The steel reinforcement in concrete must resist the significant flexural or direct tensile stresses that may cause imposed or restrained deformation. However, excessive tensile stress over

the tensile strength can prompt many narrow cracks. These cracks are visible and result in poor aesthetics for the structure (Patrick and Bridge, 2004).

Virtually, surface cracks in all types of structural elements are indispensable indicators of damage and durability. Due to the mandates for structural health control and sustainability in the construction field, a developing market of the non-destructive testing approach has grown. For example, wireless crack detection, using radio frequency identification technology by Pour-Ghaz, et al. (2014), is employed to evaluate the structural health of buildings. The non-destructive test is an approach to detect flaws in concrete structures by relying on various types of mechanical or electromagnetic radiation. This paper reviewed and discussed the impact-echo method to obtain the crack data, such as depth, width, and crack mapping of a slab structure. The illustration for the impact-echo method is shown in Figure 1.1. For the prediction of crack propagation using the impact-echo method, stress waves such as pressure wave, Rayleigh wave, and shear wave need to be studied to construct a crack propagation model.
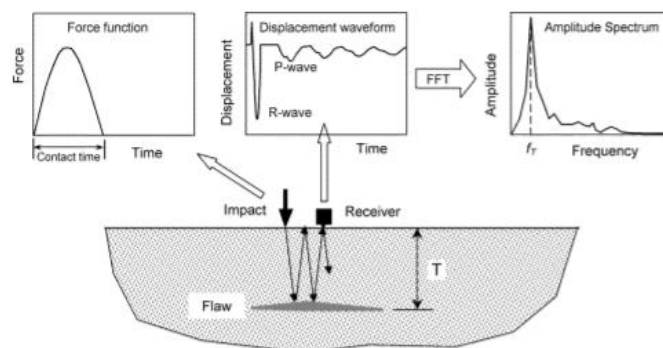
Figure 1.1: Schematic Diagram for Impact-echo Method (Carino, 2015).

In the construction site, the location of the concrete crack is significant for remedy work. Hence, there are tons of internal flaw detecting approaches in engineering practice, and the position of surface crack was traced manually on the drawing for diagnosis. The whole process is time-consuming and might subject to error, which brings wastage in cost and delay in projects. Therefore, researchers had proposed an automated crack detecting approach to improve the repairing work efficiency, including the image processing approach (Rabah, et al., 2013) and stress wave tomography (Du, et al., 2015). This paper reviews all

methods regarding time efficiency, computational cost, and limitation on the equipment available. Two-dimensional and three-dimensional models were designed and verified with the artificial crack initialized in the concrete specimen to examine the model's reliability.

The crack mapping approach in this model utilizes the distinction of waveform parameters such as velocity and amplitude to create a region that indicates the defected area. Nevertheless, the composition of the concrete medium varies based on the scale of interest. Several papers had suggested the concrete is heterogeneous at the microscale and mesoscale level (Sagar and Prasad, 2009). In this study, a numerical model associates with the mesoscale level is considered to identify the random distribution of aggregate and cement paste. The waveform parameter fluctuates in the different transmission mediums. This phenomenon is due to the variability of the Young modulus and Poisson ratio in the concrete specimen, which affects the value of hypothetical longitudinal wave speed in each mesh element. Therefore, a function of random field distribution was proposed in this paper to estimate the value of Young's modulus and Poisson ratio that affect the waveform parameters. The stochastic and deterministic models were acquired to compare the time efficiency and the error percentage between numerical and experimental outcomes.

1.2 Importance of Study

This paper presents an integrated three-dimensional crack predicting model to assess the concrete condition. This research may significantly impact the usage of the non-destructive test (NDT) by providing a guideline to relay the conventional NDT with the artificial intelligence model. The Impact-echo method is the commonly employed technique for rapid defection and thickness evaluation for structural materials. Impact-echo generates three types of waves, including Rayleigh wave, pressure wave and shear wave, that provide information on the concrete condition. Hence, the conceptual formulation is crucial to visually present data by converting the signal into a crack imaging model. The data interpretation can be carried out efficiently and generate the information that facilitates concrete and masonry structure evaluation. The major advantage of the proposed model is to enhance the performance of the non-destructive test in terms of reliability, accuracy, and effectiveness.

Construction of building structures is handled by several parties, including contractors, consultants, technician, and engineers. However, it is indisputable where deterioration of concrete occurs during construction and post-construction stages. Consequently, immediate remedy work is required to ensure the transcendence of construction work. Repairing work could be time-wasting and costly due to the unidentified source of defections. Hence, crack mapping is necessary to detect the precise location of the concrete flaw. This conceptual algorithm aims to provide the imaging of concrete flaw prediction so that the time and resources can be lessened. The developed model delivers surface and cross-section illustration of predicted crack propagation sufficient for a comprehensive evaluation of the concrete condition. The accuracy of the crack mapping model is an imperative parameter to improve the reliability of results. If the result is subjected to a high discrepancy, it might lead to longer remedy duration or wastage of financial and non-financial resources. Therefore, the conceptual formulation is modified and optimized to improve the non-destructive test performance and the remedy procedures.

This conceptual formulation employs a non-destructive test to provide the basic information of concrete structure using elastic wave. The non-destructive test is required when the structure's hardened properties or structural stability is disturbed by the indecisions considering the workmanship level under construction operation. The non-destructive test is preferred over the destructive test as the completeness of structure could remain and minimize the wastage of materials. The selection of testing method commonly depends on suitability and effectiveness. Therefore, this conceptual formulation is augmented to provide a precise crack imaging model with the least field test required. It involves a stochastic process that allows the estimation of crack propagation using the spatial interpolation method. With the conceptual formulation associated with the stochastic model, an integrated three-dimensional crack mapping prediction model is developed to assess the concrete structure accurately and effectively.

1.3   Problem Statement

Several researchers advocated non-destructive testing involving image processing (Rabah, et al., 2013), Radio Frequency Identification Technology (Pour-Ghaz, et al., 2014), and elastic wave tomography (Du, et al., 2015). Besides, ASTM C1283-15 (2015) provides a straightforward methodology to evaluate the concrete condition using Impact-Echo Method. The parameters, such as velocity and frequency, correlate to the elastic wave from the hammer strike and identify the concrete slab thickness. A question remains whether the existing procedure could effectively distinguish the defected region when minimal information is presented. The crack mapping model is rarely seen in the non-destructive test to provide a complete assessment of concrete either under construction or existing structure. A crack mapping model is desirable to evaluate the sample and provide a clear visualization for remedy work.

Although researchers propose several crack mapping models to predict the location of concrete defections, the methodology is limited by a few restrictions. The intended models require early identification of crack location before the test is initiated. The crack must be positioned at the centre between two sensors. Therefore, the models fail to carry out an independent crack detection without the aid of other detecting approaches.

Moreover, the stack image based on impact-echo (SIBIE) method perceives the crack imaging by determining the variation of frequency due to the reflection of the wave at the crack boundary. Nevertheless, the results show a symmetrical result at both sides of the crack image due to the one-point detection. The misleading result might lead to high discrepancies and affect the model's reliability against the practical crack detecting approach. It is of interest to improve and develop a crack imaging model that allows precise detection independently compared to previous models.

The concrete exhibits the heterogeneity properties at the microscopic and mesoscopic level, which consists of different parameters throughout the medium and affect the assessment of concrete crack. Researchers have conducted tons of study on stochastic modelling on focusing the random parameters on modelling the fracture process of the concrete structure. Stochastic models such as mixed-mode I-II crack propagation criterion (Wu, et al., 2013), multi-parameter random field, and meshless discretization (Most and

Bucher, 2006) was reviewed to improve the understanding of random field distribution of the concrete parameter in Chapter 2. The random field distribution in concrete influences the characteristics of the waveform introduced by the elastic wave measurement equipment. Therefore, the stochastic model is contemplated in the crack mapping prediction.

1.4 Aim and Objectives

For this entire research conducted, the aim is to formulate a feasible crack mapping prediction method for concrete monitoring using stochastic modelling. The objectives that are required to comply with the topic of this research:

i.   To review and construct an integrated crack mapping model associated with non-destructive test approaches to evaluate concrete defection.

ii.   To build a stochastic model considering the random distribution of engineering properties in the heterogenous interest of concrete structures.

iii. To optimize the crack mapping model's performance in terms of reliability, accuracy, and effectiveness compared to the existing models from researchers.

1.5 Scope and Limitation of the Study

This study predominantly focuses on the topic related to the mapping of the surface crack and sub-surface defection of concrete structure using the non-destructive test. The scope of this study includes the generation of a random field, the prediction of crack mapping, analyzing the characteristic wave input into a designed numerical model using software such as Python, MATLAB, Microsoft Excel, and ABAQUS.

Apart from that, this research adopted Rayleigh wave and Pressure wave to present a three-dimensional crack mapping analysis. Therefore, the author proposed two numerical models, including the Delta method, which characterizes the R-wave velocity and ABAQUS simulation, allowing more extensive elastic wave simulation in the proposed model. The parameters such as time-of-flight data and wave frequency were attained and put into the proposed model. Comparison and verification were made between numerical

and theoretical results to determine the benefit of models. The advantages of the model were identified by contrasting with the preceding model, and recommendations were provided.

Nevertheless, the experiment result was neglect for the verification of the model due to the pandemic condition of COVID-19. This paper discusses the result and compares the numerical models and theoretical assumption. Besides, the simulation is challenging as there is the absence of standard guideline for the elastic wave simulation in ABAQUS. The methodology of the simulation is discussed among researchers online to provide a successful numerical simulation. Lastly, the crack imaging model is rarely available in research. Hence, this study referred to and reviewed the model for another field, such as wood defections. The technique was modified and improved in this paper to provide a feasible crack mapping formulation.

1.6   Contribution of Study

The outcome of this paper provides a new alternative for the crack imaging model associated with a non-destructive test using the stochastic model. The model aims to improve the methodology of non-destructive test in terms of capability, accuracy and effectiveness. Moreover, this is the first study considering the heterogeneity of concrete in the numerical simulation to predict the crack mapping in actual concrete structure precisely.

1.7   Outline of the Report

This report is made up of 5 chapters in total. The first chapter provides a vision into the general knowledge of concrete crack, the importance of the non-destructive test, the application of crack mapping, and the introduction of the stochastic model. Chapter 1 also includes the importance of the study, problem statement, aim, objectives and the scope and limitation.

For Chapter 2, literature reviews are done based on the classification of cracking in the solid structure. The non-destructive test is reviewed to identify a suitable approach for the numerical design model. The stochastic process on random field distribution is discussed and contrasted. This topic also focused on the numerical method of crack mapping by utilizing elastic wave propagation.

Chapter 3 discusses the methodology and workflow from designing a numerical model, conducting an experiment, verifying the result, and recommendation. The developed numerical model includes two-dimensional and three-dimensional crack mapping prediction. The simulation of wave propagation is proposed, including the Delta Method and ABAQUS simulation. The generation of random field distribution is discussed.

Chapter 4 discusses the elastic wave properties towards the crack presence in the concrete sample and the adaptation for newly developed crack imaging algorithms. The random field distribution is obtained and reviewed. Finally, all the required information is put into the proposed model, and the result is compared with the preceding model to determine the reliability, accuracy, and effectiveness.

Chapter 5 summarizes the findings with conclusive remarks and provides recommendations for future studies.

CHAPTER 2

LITERATURE REVIEW

2.1 Introduction

Control of cracking is crucial to provide the serviceability of building in the construction field. In Eurocode 2, concrete defection controls are discussed in parts 7.2 and 7.3, respectively (Department of Standard Malaysia, 2010). The crack can be controlled by determining the minimum area of reinforcement and limiting the maximum bar diameter and maximum bar spacing. However, the crack still occurs in the construction field due to other factors such as thermal changes of surrounding areas, plastic shrinkage, elastic deformation of building, foundation movement, and soil settlement. When the design follows an appropriate measure under the code, the concrete crack formation is minimized. The dormant crack does not affect structural stability and durability. However, concrete crack weakens the serviceability of the structure and might cause acute structural failures in extreme cases.

Crack detection is well known in various engineering practices. The detection methods are classified into two factions: the destructive and non-destructive tests. The former is usually employed in the laboratory, where specimen properties are examined under critical conditions. For example, aggressive environment testing, corrosion testing, fracture, mechanical testing, fatigue testing, and residual stress measurement are typical destructive tests used in determining concrete's properties. The American Society of Civil Engineering suggests the non-destructive test to analyze the fracture damage or defect. The comparisons between the destructive test and the non-destructive test are tabulated in Table 2.1.

Table 2.1: Comparison between destructive test and non-destructive test
(Godfrey and Henry, 2016).

Destructive Test	Non-Destructive Test
The test is limited to a small portion of the specimen obtained from the whole production part. The stimulation of properties is considered partiality.	The test is made on the whole part of the structure or entire critical region. Subsequently, the evaluation of properties applies to the pieces.
A single destructive test might only assess one or a few properties of a specimen under critical condition.	Multiple non-destructive tests can be carried out correlating to different properties. As a result, different properties according to various service conditions can be obtained.
The destructive test does not assess the properties of specimens under service conditions. The accuracy of the testing may differ from the actual serviceability state.	The non-destructive test can be performed directly upon the specimen used in service. The result of the testing represents the actual properties of the specimen.
With high replacement and fabrication costs on the specimen, the amount and variation of the destructive test are limited.	Repeated non-destructive tests can be carried out without replacing the material if the test is economically and practically validated.

2.2 Non-Destructive Test

Several non-destructive test approaches were discussed and reviewed on the reliability and other factors such as expected outcome, computational cost, the time required, and equipment employed in this study. The tests included in this sub-chapter were sensors such as radio frequency identification technology and soft elastomeric capacitor, image processing method from the laser scanner, and elastic wave or stress wave assessment involving ultrasonic pulse wave and impact echo.

2.2.1 Radio Frequency Identification Technology

An electrically conductive material is also known as the conductive surface sensor, which was employed to detect the cracking in the concrete element. The shift in electrical resistance provides information on the concrete crack. When the structure is loaded, the sensor detects a noticeably increase in strain. The concrete crack was detected when a sudden drop was noticed from the sensor.

Pour-Ghaz (2013) had conducted a study on the wireless crack detection technique using Radio Frequency Identification Technology that operates at 125 Hz. The rudimentary process of passive Radio Frequency Identification Technology tags requires the interrogator signal's conduction from the reader to the transponder, and an independent transmission is done to respondents from the transponder. Besides, the sensors were powered by electromagnetic induction by the alternating current in the reader coil. The relationship between Radio Frequency Identification Technology and specific parameters was studied using restrained ring tests. However, at a high degree of restraint, an extremely least amount of strain develops in the specimen, which caused problems in crack detection (Pour-Ghaz, et al., 2014). Hence, another methodology is required to evaluate the defection. Figure 2.1 has illustrated the experiment setup for restraint ring testing.
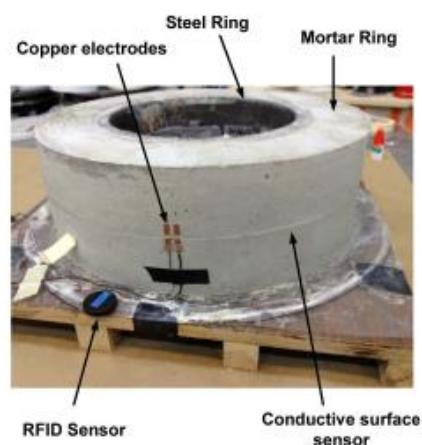
Figure 2.1: Instrumented ring for Restrained Ring Test (Pour-Ghaz, et al., 2014).

Two sets of experiments were conducted using the restraint ring tests. Firstly, the relationship between crack width and resistance increase of sensor

was defined. The second set was assessed to identify the use of Radio Frequency Identification Technology in correlating with the response of the sensor while targeting 0.10 mm crack. As mentioned above, the crack width was obtained using digital image analysis.

The result of the first set experiment showed a significant increase in electrical resistance and the crack width of the concrete sample. The crack width, as slight as 0.02 mm, could be detected using a sensor. The relationship between the electrical resistance of the sensor was statistically interpreted to determine crack width. With the vital information obtained, the sensitivity of the sensor can be controlled. By manipulating the extent of the resistor in the sensor, the sensor could detect crack of any size in concrete elements. Figure 2.2 has clearly illustrated the movement of the strain of automated crack detection using Radio Frequency Identification Technology. The mortar ring's crack was undoubtedly shown when the sudden drop occurs after the concrete element was strained. The alteration of the signal was delayed beyond 5 minutes intervals. Hence, it failed to recognize small crack at the early stage. The sensor was set to detect 0.10 mm crack width; thus, the electrical resistance increases until it was identified at the electrical resistance pre-set.
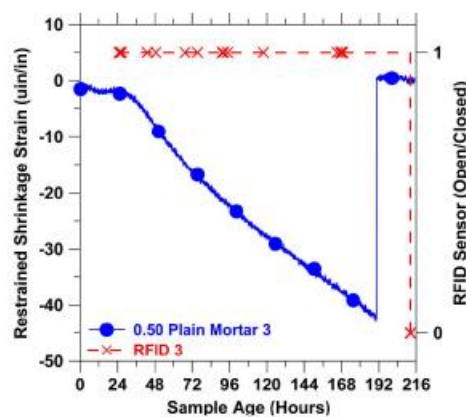
Figure 2.2: Automated Crack Detection using Radio Frequency Identification Technology sensor (Pour-Ghaz, et al., 2014).

2.2.2   Soft Elastomeric Capacitors

Yan, et al., (2019) had conducted a study on evaluating concrete defection using a dense capacitive sensor. A sensing surface technology using Soft Elastomeric

Capacitors (SECs) was proposed to detect strain on a large surface area. The SECs was implied among all automated crack detection sensor due to its cost and durability. The SECs comprises a flexible parallel plate capacitor that can transmit a significant change in capacitance when a flexural crack occurs on supervised surface geometry. The implementation of SECs on evaluating and localizing the crack propagation in concrete elements through strain measurement was assessed on concrete prototypes with a network of strip-shaped SECs.

The application of SECs was well-defined in the experiment consisting of two small-scale reinforced concrete specimens. The three-point loading test with SECs array was performed to detect the concrete crack. The SECs predominantly captured the behaviour on the concrete samples against the bending test. The statistical result is shown in Figure 2.3, and the relationship between crack growth and time was illustrated. The crack initialization was indicated through the slight drop in relative capacitance, along with a shear crack opening noticed when a loss of capacity around 1.9 mm was detected. The performance of SECs was concluded from the time series analysis plan in maximum, residual and average relative change in capacitance (Yan, et al., 2019).

This method presented precise time-series data on the crack initialization with the change of capacitance of sensors. However, it did not consider the crack parameters such as crack location, width, and depth. It is only suitable for the crack monitoring process, where the time of crack initialization is essential. Besides, the SECs only provided crack detection on the structure's surface, which is insufficient for an overall evaluation of concrete damage.
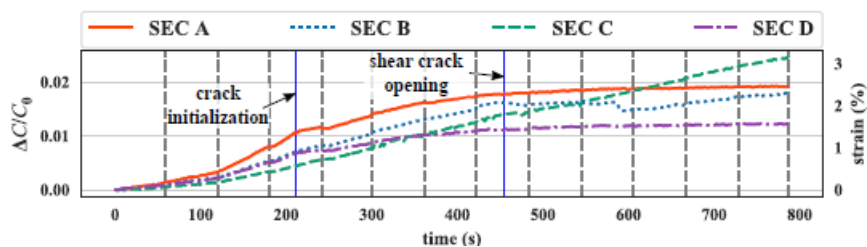
Figure 2.3: Time series data for Evaluation of SECs (Yan, et al., 2019).

2.2.3 Concrete Surface Image Surveying

Automated crack mapping on concrete surface surveying provides high efficiency for non-destructive testing. Rabah, et al. (2013) researched Terrestrial Laser-Scanner's application on crack detection and mapping. Terrestrial Laser-Scanner is equipment that generates a three-dimensional coordinate of an object by originating the scanner centre point and compute the distance of the object point on the surface horizontally and vertically. Due to the limitation on the laser measuring unit's spatial resolution, the current laser scanner was combined with both distance gauging units and an additional digital camera unit to provide a full surrounding image.

Rabah, et al. (2013) carried out crack propagation detection in three steps. The image was required to filter and remove noise, consisting of shading, stains, blebs, and non-uniform light distribution, during obtaining photos using the digital unit. The corrective image was administered by applying a non-linear digital filtering technique called the median filter. A smoother version of the input image can be attained by detracting the slight variation between the output image and the corrective image (Fujita and Hamamoto, 2011). Next, the crack is traced manually from the initiation point to the termination point. Fujita and Hamamoto (2011) have proposed probabilistic relaxation in labelling the crack propagation from noisy data. The simplified probability of the crack is designated to logarithmic transformation and updated:

The neighbouring region was divided into four sub-regions, and non-ambiguity estimation is employed for each sub-region. Four estimates were carried out along four different directions (0 °, 90 °, 180 °, 270 °), and the maximum value of estimation is used to update the probability of crack detected. Figure 2.4 has shown the probabilistic relaxation method on crack mapping.

After the crack was detected, it was redefined into a pixel coordination system. The imaging approach requires data from the lenses, pixel, principal point, and the digital unit to determine the position and orientation of the crack. Rabah, et al. (2013) had proposed an inverse perspective transformation considering a pixel coordination system (*i, j*) in image space. The auxiliary coordination system (X', Y,' Z') was applied as a reference for the linear array progression, and the object space coordination system (X, Y, Z) is used to determine the Terrestrial exterior orientation constraints Laser-Scanner.
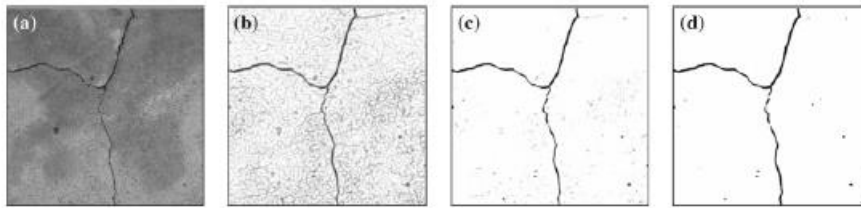
Figure 2.4: (a) Input image (b) Pre-processing Image (c) Result of Relaxation (t = 0) (d) Result of Relaxation (t = 10) (Fujita and Hamamoto, 2011).

Hoang (2018) had proposed an improved Otsu method that can spontaneously detect crack from the input image by identifying the local minimum. Min-Max Gray Level Discrimination (M2GLD) distinguished the noise of the image from the pixel of crack. It intensified the grey intensity of the estimated non-crack pixel and reduced the severity of the determined crack pixel. The crack pixel appears to be lighter and noticeable among non-crack pixels. The study was conducted using a model in the MATLAB environment. The noisy pixel and non-crack elements were processed in the image binarization method by removing objects that were less than a certain number of pixels and restricted the axis ratio index's threshold amount. After the crack pixel is detected, the image boundary extraction process was carried out to analyze the crack parameter, including perimeter, area, width, and length. The image thinning is followed to compute the orientation of crack propagation. The results of M2GLD were statistically interpreted and compared with the result of the conventional Otsu method. The M2GLD had shown a higher accuracy in detecting the crack, and no error detection was found in the experimental assessment.

In a nutshell, the image surveying method was a direct non-destructive test on evaluating the surface crack. The crack mapping was imaged on an auxiliary coordinate system while the noise was removed using several algorithms. This approach was very accurate compared to actual site conditions. However, the imaging approach only focused on the localization of surface crack while the concrete's internal defect was ignored. The bypassed internal crack of concrete affects the corrosion of the reinforcement steel bar and other severability impacts. Besides, the crack data such as depth or inclination were

insufficient to evaluate the concrete's overall damage. Hence, other approaches were discussed to design a model that can predict the crack mapping of concrete.

2.2.4 Ultrasonic Pulse Velocity Test

Ultrasonic pulse velocity (UPV) evaluates the concrete crack in a solid medium by utilizing ultrasonic waves. The ultrasonic waves are classified as an acoustic wave that can transmit through a medium. The experiment equipment consists of a pulse generator, transmitter, and a pair of piezoelectric sensors. The electronic pulse was generated and introduced into the concrete. Then, the time travelled of pulse in the concrete medium was measured to obtain the UPV. The procedure of UPV tests can be classified into three groups: direct, indirect, and semi-direct depends on the location of sensors (Kumar and Santhanam, 2006). The pulse experienced low energy when passing through an air medium. The pulse is diffracted when it travelled through the air-filled crack in the concrete. Hence, the travel time of the pulse between the two sensors increased.

By using the UPV method, the crack can be analyzed and localized in the concrete specimen. Both vertical and horizontal crack detections were carried out in the experiment. The experimental setup is illustrated in Figure 2.5 and Figure 2.6. The accuracy of crack depth measurement was conducted by Ari, et al. (2014). An artificial crack was constituted using a zinc plate at a specific position. The accuracy was obtained by comparing the average crack depth from UPV and actual crack depth. The accuracy was proven higher in unreinforced concrete or concrete with a smaller cover.
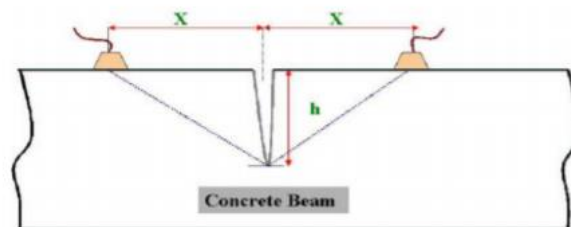
Figure 2.5: Vertical Crack Depth Estimation (Ari, et al., 2014).
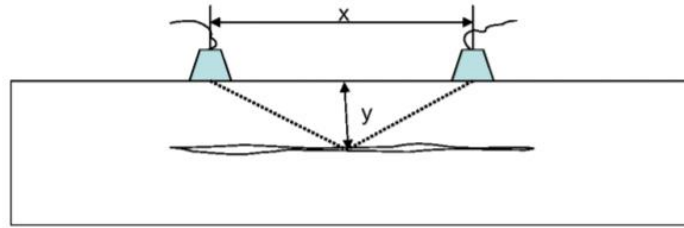
Figure 2.6: Horizontal Crack Depth Estimation (Ari, et al., 2014).

2.2.5   Impact-Echo Method

Impact-echo is a non-destructive test for evaluating the properties and internal defects of the concrete structure. This approach employs a stress wave generated from the hammering of concrete using an impactor and logs the reflections and refraction from an internal crack or other boundaries. The pulse is generated by an impact from a single point and transmit through the concrete in all directions. The difference between the impact-echo method with UPV is the lack of transmission orientation generated by a large transducer. As a result, impact-echo is most applicable in a slender concrete element such as piles. However, the applications of impact-echo on evaluating the concrete properties were discussed by many researchers. Impact-echo is a highly sensible testing solution with a wide variety of demands in assessing the concrete structure.

The mechanism of the device was by impacting the surface of the concrete specimen, and the reader of the echo signal transforms the acoustic signal into an electrical signal (Hlavac, 2009). Generally, a microphone is employed as a transducer of the signal. Amplifier and noise filter are necessary to magnify the signal. Lastly, the signal is compiled and analyzed using Fast Fourier Transformation with various frequencies and amplitudes. The illustration of the result is given as a time-series graph, spectrum, or spectrogram. The time series shows the instantaneous amplitude of the signal and the changes against time. The range of frequencies provides the amplitude caused by echo imposed by a short impact representing different frequencies. The spectrogram provides amplitudes of signal with corresponding frequency and time axis. It shows the actual intensities of different frequencies against time. The fundamental theorem employed to evaluate flaw in concrete is given in Equation 2.1 (Hlavac, 2009):

$$d = \frac{v}{2f} \hspace{3cm} (2.1)$$

where

d $\hspace{1cm}$ = the depth of flaw within concrete element/thickness of the concrete slab, m

v $\hspace{1cm}$ = the wave velocity, m/s

f $\hspace{1cm}$ = the frequency, Hz

The concrete flaw detection using an automatic oscillating impact-echo device was conducted (Chou, 2019). The impact-echo device was modified to perform automated oscillation tests, deal with signal quickly, and carried out flaw analysis for the concrete structure to determine crack depth. The study involved both hardware and software design. An adjustable automatic oscillator circuit was designed to induce electromagnetic force to activate the oscillating impact echo device. The induced electromagnetic wave prompted the electromotive force that provides power to the adapted wooden hammer. The device produced stable impacting forces of 0.03 kg for every cycle.

Onto the software design, the echo soundwave was measured using a microphone and transferred to the computer through a sound card. The impact-echo signals were stored and analysed using MATLAB. The signal was translated into the time domain and frequency domain programs to evaluate wave velocity and assess internal flaws. The incident impact point wave and the first reflected wave graph were employed to determine the impact time and first reflected wave receiving time for the analysis of the result. The time obtained was used to calculate the wave velocity, which was vital to assess the crack depth. Two pronounced frequencies were obtained from the spectrogram using Fast Fourier transform. The thickness and crack characteristics were acquired using those parameters. The average value of crack depth obtained from the experiment was matched with the actual crack depth of the concrete specimen prepared.

In this study, the impact-echo method was employed to evaluate concrete flaw properties. Most of the researchers whose work on this topic assessed the concrete based on the concrete crack's location and depth. The data

obtained from this test was insufficient for localizing the concrete crack. The behaviour of the stress waves is studied to modify the impact-echo method for the crack mapping application. A stochastic model is required to predict the crack propagation on the concrete surface with limited data available.

2.3   Elastic Wave

In the past centuries, a wide range of stress wave applications was introduced in various engineering practices. For example, plate thickness measurement according to ASTM C1383 (Nicholas, 2001), concrete strength evaluation (Lim, et al., 2016), and, most importantly, internal flaw detection of concrete structures was implementing non-destructive test to evaluate the condition of building construction. Nevertheless, the stress wave properties need to be explored and assessed to design an autogenous flaw detection model using the impact-echo method.

When an impactor strikes on the surface of a solid concrete specimen, a form of the acoustic wave that travels at finite velocity was introduced into the system. It induces a circumstance called disequilibrium, which originates the material particles to vibrate on its equilibrium location. The stress wave can be classified into pressure wave, shear wave, and Rayleigh wave. The motion of elastic wave propagating in the medium is illustrated in Figure 2.7. The P-wave and S-wave expand as spherical wavefronts through the concrete specimen, while R-wave travels from the impact near the surface region. The P-wave travels at the highest speed associating with normal stress. The particle motion is parallel to the propagation direction when the P-waves pass through the point. The S-wave moves slower and is accompanied by shear stress. The particle motion is perpendicular to the propagation direction when the S-wave passes through the point. Among all the waves, the R-wave has a lower speed but higher frequency. The particle motion is more complicated compare to another wave. It moves in a backward elliptical motion when R-wave passes through the point (Carino, 2001). The comparison between different types of the elastic wave is discussed in Table 2.2.

Table 2.2: Specification of Elastic Wave (Lee and Oh, 2016).

Wave Type	Particle Motion	Wave Speed	Energy Content, %
P-wave	Parallel to the propagation direction	$C_P = \sqrt{\dfrac{E(1-v)}{\rho(1+v)(1-2v)}}$	7
S-wave	Perpendicular to the propagation direction	$C_s = \sqrt{\dfrac{E}{2\rho(1+v)}}$	36
R-wave	Retrograde Elliptical	$C_r = C_s \dfrac{0.87 + 1.12\,v}{1+v}$	67

where

E   = Modulus of elasticity, GPa

ρ = density, kg/m^3

v = Poisson's Ratio
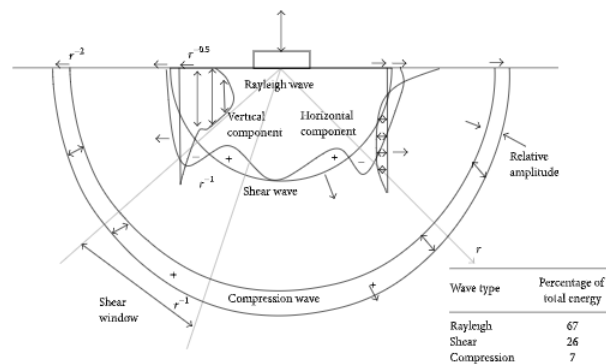
Figure 2.7: The Propagation of Stress Wave in the Solid Medium (Lee and Oh, 2016).

2.3.1   Surface Wave (Rayleigh Wave)

Rayleigh wave is widely used to assess the surface-breaking crack in concrete due to its unique features, including low attenuation and high possession energy.

The R-wave effect is apparent in the time-domain waveform, where the massive surface displacement at the beginning of the waveform. The depth of the R-wave depends on the propagating frequencies. For example, the higher the frequency, the lower the wavelength, the R-wave intensity is reduced eventually (Carino, 2001). R-wave shows evidence of an assertive dispersion behaviour where the wave velocity depends on the frequency. R-wave dispersion and diffraction properties provide vital information on the existence of a flaw in the propagation medium.

Generally, the R-wave velocity is measured based on the time difference between the first burst peak of two receivers. However, the peak point is difficult to identify, and the result of the concrete characteristic evaluation is affected. Ryden, et al. (2004) proposed using the dispersion curve of Lamb wave with multi-channel analysis of surface waves. The waves were collected along with a linear array of sensors which equally spaced from the source of high-frequency impact. The data collected was processed by each sensor and transformed into the frequency-phase velocity domain using the Fourier Transform. The surface wave interpreted in the dispersion wave represented R-wave, which was very useful in material characterization, including wave velocity, Poisson ratio, and plate thickness.

The R-wave is generally detectable as it produces a stiff peak following the first arrival of the lower amplitude P-wave. The R-wave velocity was computed, adopting the time difference between the first burst amplitude detected from the sensor before and after the crack (Lee and Oh, 2016). The results showed a noticeable delay and reduction of the amplitude of the first burst peak of the R-wave among two sensors. The crack functioned as a void that overturning the propagation of stress waves. The study also presented the behaviour of the stress wave against the inclinations of surface-breaking cracks. The composition of waveforms was compared among vertical crack, 30-degree inclination crack, and 150-degree inclination crack. A consistent delay was observed in the vertical crack, while a distorted arrangement and reversible arrangement of waveform were noted in the corresponding inclination crack. The variety of wave frequencies were discussed in the study. A lower frequency wave experience variation in amplitude as the subsequent wave's wavelength

was higher than the crack depth. Hence, it passed directly underneath the crack and barely experience delay and attenuation in amplitude.

Two waveform parameters were introduced in correlation with the crack specimen. The velocity indices represented the ratio of the summation of wave velocity in the crack model to the sound model. The velocity index was a proper parameter in evaluating concrete crack and quantifying its depth. When the velocity indices indicated 1.0, it showed absences of crack existence identical to the sound model. The velocity indices decreased when the ratio of crack depth-to-wavelength increased. This phenomenon can be explained as the crack depth amplified corresponding to the wavelength and the effect on wave velocity become less disturbance by the void. A greater excitation frequency also resulted in higher velocity indices. However, a dissimilar trend was observed where the crack inclined more than 90 degrees (Lee, et al., 2016).

While evaluating the effect on the amplitude of the R-wave, the amplitude index was introduced. The amplitude index defined as the ratio of summation of amplitude detected after crack went into the amplitude before the crack of the crack model to the sound model. The amplitude indices became lower in all inclination cases when the ratio of crack depth-to-wavelength increased. The amplitude index also decreased in connection with the increase of the inclination rate of crack. As a result, the obstruction of energy in the R-wave increased as the crack's inclination rate increased. Both velocity and amplitude indices exhibited insufficient sensitivity towards detecting crack with a depth of 150 mm. This phenomenon denoted that R-wave was more suitable to detect the surface crack as it propagated near the surface.

In conclusion, the study is advantageous because the energy of the elastic wave decreased subject to the crack. The dissipation of energy was affected by the depth and inclination of concrete depth. However, the Rayleigh wave's inability to detect the crack with an immense depth is considered. Other forms of the elastic wave are discussed to achieve a more comprehensive crack detection with the slightest inconsistencies.

2.3.2 Bulk Wave (Pressure Wave)

Bulk wave, is also known as bulk acoustic waves, are the elastic waves propagating in the medium, including solid and liquid. They are classified into

the longitudinal wave and transverse wave, represented by pressure wave and shear wave. The longitudinal wave is categorized as P-wave, whereas the transverse wave is classified as S-wave, as shown in Figure 2.8.

(a) Pressure wave

(b) Shear Wave

Figure 2.8: Bulk Wave in Solids (HyperPhysics, n.d.).

P-wave is widely applied in the construction field for evaluating the concrete condition. Non-destructive tests such as ultrasonic testing had studied the resonance frequency of P-wave transmission in a medium to identify the surface crack depth of a specimen (Tokai and Ohtsu, n.d.). In ASTM C1383, the standard test method was shown where P-wave velocity was measured to identify the thickness of the concrete slab. The application was further modified by Kruger and GmbH (2006) to determine the crack depth of a steel-reinforced test specimen. The transmission mode of P-wave is classified into direct, semi-direct, and indirect transmission. The direct transmission illustrates the initiation of the wave on one side of the structure by the impactor. Hence, the transducer was attached to the opposite side to receive the signal wave. The semi-direct is seldom employed based on the access to the surface of the testing specimen. Lastly, the indirect transmission mode is mainly used when the tomographic survey is necessary. The P-wave's reflection coefficient due to the boundary or internal defect is examined to provide the crack mapping information for the concrete specimen.

As the internal defect partially reflects the propagating P-wave in the solids, the wave's reflection characteristic is employed to detect the crack. The location and size of cack in a finite concrete specimen are assessed based on wave reflection intensity amplitudes. The reflection intensity was computed from the signal information obtained from the experiment. The crack's magnitude was examined according to the correlation between the dynamic

parameter of the crack (Fan, et al., 2012). The scanning SIBIE method produces a two-dimensional image of the crack region by applying this mechanism.

With the aid of the pressure wave, the crack with more significant depth may be detected. Hence, the proposed model is utilizing R-wave and P-wave to achieve an integrated crack mapping prediction model. The R-wave is employed to detect the crack location, while the P-wave is used to identify the crack tip location.

2.4   Interpretation of Elastic Wave

As the time domain signals only provide the signal's value at any given instance, the information about the rate of the varying signal is absent. Thus, the signal requires processing and arising to another domain, illustrating the rate at which the signals vary. A transform is required to convert the signal from time domains to frequency domains to obtain the distribution of signals' energy over a series of frequencies. The frequency-domain analysis is broadly used to signal processing applications in structural health monitoring of concrete structures and image processing of defection. Frequency-domain analysis is a vital key for crack detection as it provides information on the phase shift of the signal.

2.4.1   Fast Fourier Transform

Fast Fourier Transform (FFT) as a time-frequency analysis tool has been generally employed to study the frequency content of stress wave propagation in the impact-echo method. An impact echo always provides a volatile signal with various frequency due to the wave's short impact time and attenuation. The frequency peak is difficult to identify directly from the impact-echo spectrum from multiple reflectors. Hence, FFT is a complementary process for analyzing complex and intricate IE signals by illustrating the data into a two-dimensional time-frequency plan. With this approach, the noise or echoes caused by the geometrical boundaries and concrete heterogeneity can be distinguished as the FFT-based spectrum ignores those noises (Shokouhi, et al., 2006).

2.4.2   Depth Spectral

Yeh and Liu (2009) intended a spectral imaging method to enhance the evaluation of the damage model by the impact-echo method. The B-scan and C-

scan method based on ultrasonic testing was employed to produce the image of the cross-section of the concrete specimen. The B-scan involved a sequence of impact-echo test on a test line, and the amplitude of the spectrum was represented by colour scale against frequency. The boundaries of the colour scale were set within a range of maximum and minimum amplitudes. Besides, the C-scan provided an image of a horizontal cross-section on a square mesh. By applying the coordination approach and frequencies of each axis, a three-dimensional matrix was constructed. The frequency was determined using Equation 2.1, and the corresponding amplitude of the spectrum was computed to present as colour scale in a two-dimension image like B-scan.

Nevertheless, a frequency-depth transformation was required to transform the horizontal axis into depth, as shown in Figure 2.9. A constant change in depth was nominated, and the corresponding frequency was converted into depth using Equation 2.1. Besides, there was a possibility that the burst peak at the original spectrum was omitted when it felt between the subsequent frequencies. Hence, the amplitude of each frequency was calculated using interpolation. This approach delivered a range of constant depth interval, which was necessary for volume visualization.
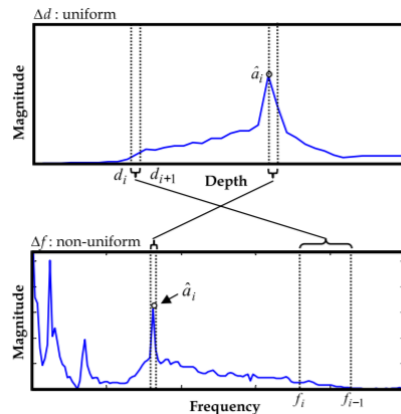
Figure 2.9: Frequency-Depth Transformation (Yeh and Liu, 2009).

2.5   Stochastic Model on Heterogeneity

Theoretically, the concrete structure is homogenous on a macro-scale, and the engineering properties of concrete is assumed to be uniform along with the element. However, several researchers have conducted testing and an assessment of the engineering properties of the concrete structure and consider

the fact that the assumption on the homogeneity of concrete properties is overly enthusiastic. Since concrete is a mixture of cement powder, water, fine and coarse aggregate, and admixture, it is very tough to ensure uniform mixing of the compound when the concrete is cast in situ. Stawiski (2012) had conducted a study by evaluating the compressive strength of the concrete cylinder. By penetrating the ultrasonic pulse through the specimen, the compressive strength throughout the specimen varied in depth, as shown in Figure 2.10. Therefore, the heterogeneity within a concrete medium was established, and random field distribution of concrete characteristics was discussed.
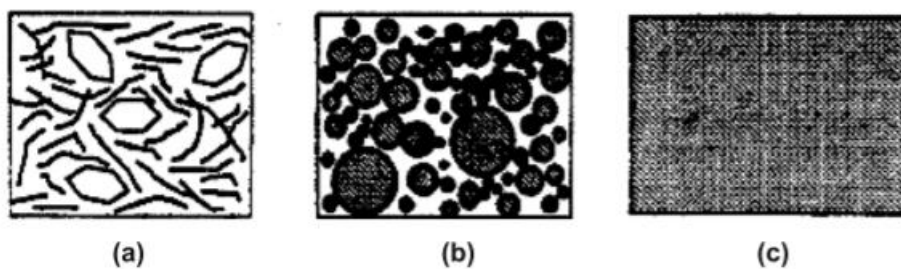
Figure 2.10: Heterogenous Properties of Concrete (a) Micro-level [10-8 m to 10-4 m] (b) Meso-level [10-4 m to 10-2 m] (a) Macro-level [10-1 m to 10-2 m] (Sagar and Prasad, 2009).

Most and Bucher (2006) had conducted research based on the simulation of random parameters distribution in the concrete medium using the stochastic model. Non-Gaussian distributed parameters represented the multi-parameter random field. In this study, the fluctuation of parameters was inferred as a multi-dimensional stochastic process by the autocorrelation process. The integration point method is employed, while discretized numerical interpretation in a finite element analysis was determined at the Gaussian integration point. The benefits of this method include the direct correlation of the covariance matrix and applicable to various models.

Nonetheless, the mesh size is restricted where it did not adequately account for small correlation lengths. For the simulation of heterogeneous solid structure, the relationship between various material parameters was considered. Therefore, the idea of a single-parameter random field was developed into a multi-parameter random field that considers young modulus, tensile strength,

and fracture strength in random fields. The covariance matrix for multi-parameter is extended from correlating the parameter covariance matrix with the geometrical correlation matrix.

The heterogeneity properties of concrete cause uncertainties in fracture properties, which result in the effect on dependability and actual load-bearing capacity of the concrete structure. Several researchers have established quasi-brittle material behaviour where the macro-cracks typically occur after a micro-crack is formed in the fracture process zone. After the macro-cracks occurred, a new micro-crack forms eventually where cohesive force is present. Zeng, et al. (2019) has proposed a stochastic model that considers heterogeneity properties and cracks growth in concrete. A concrete specimen division characterizes the stimulation of concrete structures into numerous representative volume elements (RVE). Due to the random distribution of elements such as sand, cement hydrate particle, and porosity, the mechanical properties of RVE vary along with the concrete specimen. The variation of engineering properties is studied using the statistical probability method.

The macroscopic engineering properties of concrete is illustrated in Figure 2.11. For example, elastic modulus, fracture energy, and tensile strength are represented by a numerical implementation of Weibull distribution with reasonable accuracy (Zeng, et al., 2019). Based on the theory, the distribution function and probability density function of Weibull Distribution can be used to determine the number of RVEs with engineering parameters (such as strength and elastic modulus) in every interval. The Monte Carlo Method creates a random number in the probability sampling scale to fix the range of mechanical properties of each RVE.
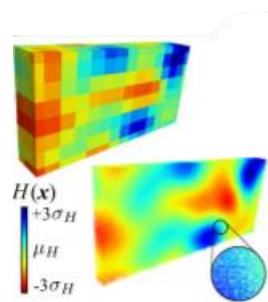
Figure 2.11: Random Distribution Sample on Mesh Grid (Eliáš, et al., 2015).

The materials' randomness caused fluctuation of material parameters in the concrete specimen, represented using a spatially auto-correlated random field (Eliáš, et al., 2015). In the mesoscale of concrete structure, the parameters were allocated into a random field with a coordinate system. The value of each grid element was attained randomly from the cumulative probability density function. In the study, the four constraints, including shear strength, shear modulus, tensile strength, and tensile fracture energy, had the same coefficient of variation, which were provided in the same field distribution. The researcher proposed an expansion optimal linear estimation method for evaluating the Gaussian field to reduce the computational time. The value of the random field at the surface of the specimen can be attained using Equation 2.7 (Eliáš, et al., 2015),

$$\widehat{H}(x) = \sum_{k=1}^{K} \frac{\xi_k}{\sqrt{\lambda_k}} \psi_k^T C_{xg} \qquad (2.2)$$

where

λ_k = eigenvalues of the covariance matrix,

ψ_k^T = eigenvectors of the covariance matrix,

C_{xg} = vector to the centre of the surface,

ξ = independent standard normal variables.

Equation 2.3 shows the value for the Gaussian random field respective to the centre of the specimen surface. The random distribution values required transformation to a non-Gaussian space to represent the variables in a random field. The conversion was expressed as follow (Eliáš, et al., 2015),

$$H(x) = \text{F}_H^{-1}(\emptyset(\widehat{H}(x)) \qquad (2.3)$$

where

$\emptyset$ = cumulative probability density function of Gaussian random field,

F_H^{-1} = variable from Gauss-Weibull distribution.

As in result, the random field distribution provides a good visualization of the heterogeneity properties of concrete. The outcome of the crack analysis using the random parameter model was practically identical to the experimental result. Therefore, the stochastic process was necessary for the crack mapping process. In this study, the elastic wave motion depended on the concrete parameter distribution in the concrete specimen. A random field distribution function was conducted in Python.

Researchers worked on the best representation of concrete population using lognormal distribution, including the computation of characteristic value under mechanical testing (Torrent, 1978) and providing information during the delivery and placement of concrete (Graham, 2005). The results drew a parallel between both studies where the lognormal distribution presents a sufficient flexible theoretical assumption in the properties of concrete. Normal distribution works well in simulating the properties of concrete when the coefficient of variation is small. However, when the coefficient of variation increases, the normal distribution fails to provide an accurate distribution of values. Hence, the lognormal distribution is assumed under the development of characteristic value.

2.6   Crack Mapping Approaches

In the structural health monitoring process, crack mapping is crucial as it provides the length, depth, and location of internal or surface defect on the concrete structure. The analysis of crack mapping allowed the identification of construction defects that potentially affect structural stability. Shah, et al. (2018) studied wave-based inspections, and a numerical technique was proposed for imaging the wave propagation through the concrete medium. A wave visualisation was vital to detect crack as the local cracks tended to scatter the approaching stress wave. The ultrasonic waves, which averagely exceed 20 kHz, were proven to effectively detect the damage in composite's steel concrete and plate-like structures. An efficient structure mapping was essential to determine the seriousness of the damage.

As a result, the finite difference discretization method was introduced to simulate the medium's ultrasonic wave propagation. Figure 2.12 illustrates the wave propagation of specimens with and without aggregate. By comparing the

results, the aggregate in the concrete medium considerably scattered the travelling wave. The reflections from the crack indicated the crack region of the concrete medium. However, the crack mapping accuracy was significantly reduced by the inclusion of aggregate in the crack image. The reflection subjected to the aggregate was displayed in the crack image, which might provide the wrong information for the concrete repair procedure.

In conclusion, some filtering parameters are required in the imaging equations to eliminate aggregate or other elements in the concrete medium. Therefore, different models or techniques were discussed to obtain a reliable crack mapping for viable concrete condition evaluation.
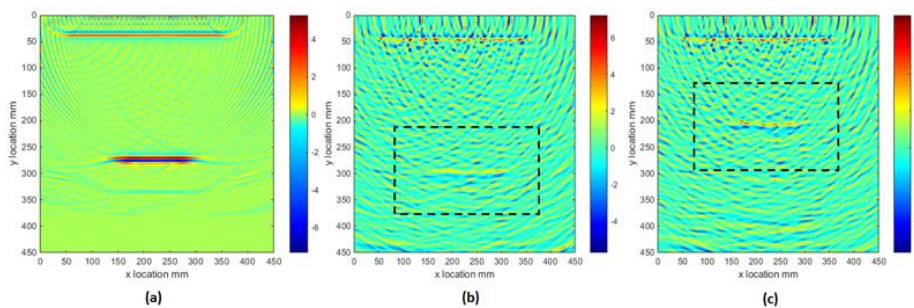
Figure 2.12: Crack Mapping for Concrete Sample: (a) Without aggregate, crack location 300mm (b) With aggregate, crack location: 300mm (v) With aggregate, crack location: 200mm (Shah, et al., 2018).

2.6.1 Synthetic Aperture Focusing Technique (SAFT)

A non-destructive test is a standard method for the detection of the internal defect in the concrete structure. Ganguli, et al. (2012) had proposed an algorithm called SAFT to identify the internal defect of concrete structure using the application of electromagnetic wave. The crack image is illustrated by the scattering of the elastic waves from the frequency-domain approach of SAFT. An impactor generated an elastodynamic field in the experiment, and an ultrasonic transducer received the reflection (echoes). The wave velocity transmitted in the medium was exploited to develop the image of a concrete cross-section from the obtained waveforms in the time domain.

This paper proposed the correlation between Finite Difference in the Time Domain with the Perfectly Matched Layer on defining the boundary

condition of the waveform imitation in the solid medium (Ganguli, et al., 2012). Some assumptions had been made: (a) the waves reflected by the boundary of the specimen were ignored; (b) only the first burst peak of the waveform was considered for the analysis. When the elastic wave was generated into the medium, four distinct wave arrivals were observed, as shown in Figure 2.13, including C-C (compressive to compressive), C-S (compressive to shear), S-C (shear to compressive), and S-S (shear to shear). The arriving sequence corresponded to a compressive wave then a shear wave due to higher velocity in the compressive wave.
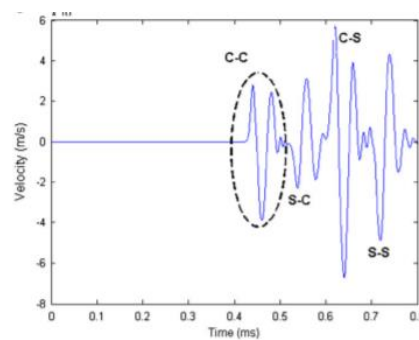
Figure 2.13: Various Elastic Wave Mode (Ganguli, et al., 2012).

SAFT reconstructed an interior structural image that discrete the concrete medium into a group of $m \times n$ pixel, which was represented by the potential point of the scatterer. The scattering point (internal void) was defined by two foci with transmitter and receiver positions in the two-dimensional medium. SAFT provided a pixel-based search of the internal void and focused the attained waveforms that spatially plotted as elliptical bands. The intersection area of the bands, called the focal spot, presented the internal defect's position. The dimension of the area was affected by the ultrasonic pulse width generated from the impact echo. The imaging of the scatterer was obtained by employing the cross-correlated function between the attained waveform and the reference point of the scatterer. Initially, the analyzed waveform covered only C-C wave; the images significantly affected by the noise, and the accuracy of the crack detection was reduced. Therefore, Ganguli, et al. (2012) considered entire segments of the scattered elastic wave, and the cross-correlation amplified the signature of the response in the whole scattered field. The intensity of noise was

reduced, and the reliability of imaging was increase drastically. The result from SAFT is shown in Figure 2.14.
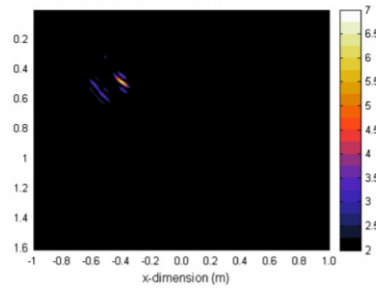
Figure 2.14: Combined Image Value after Thresholding (Ganguli, et al., 2012).

2.6.2   B-scan/C-Scan

Yeh and Liu (2009) proposed several imaging methods for crack detection by applying depth spectral on the waveform data. The approaches were employed to identify the dimension and position of the defection in the concrete specimen. A sequence of the impact-echo test was conducted on the structure's surface to achieve an accurate image rendering. The concrete sample surface was discrete into a Cartesian coordinate plane consisting of an x-y axis, as shown in Figure 2.15. The impact-echo test was performed at each grid of the mesh. The midpoint between the impactor and the receiver must be concurrent with the centre of the grid. The frequency spectra were transformed into depth spectra for crack tomography. The array $V[i,j, 1 \leq k \leq n_z]$ represented the amplitude of spectrum for each grid in the range of depth interval.

The spectral C-scan and B-scan generated the image of crack mapping for horizontal and vertical cross-section, respectively. For tomography, the array $V[i,j,k]$ required transformation into colour scale array $c[i,j,k]$. The conversion was demonstrated as (Yeh and Liu, 2009):

$$c[i,j,k] = \begin{cases} c_{\max} & V[i,j,k] > V_{\max} \\ c_{\max}\dfrac{V[i,j,k] - V_{\min}}{V_{\max} - V_{\min}} & V_{\min} < V[i,j,k] < V_{\max} \\ 0 & V[i,j,k] < V_{min} \end{cases} \quad (2.4)$$

where c_{max} was the upper limit of colour scale and $[V_{max} - V_{min}]$ represented the range of amplitude spectrum. The value of V_{min} was increased to reduce the noise and improve the reliability of the model.
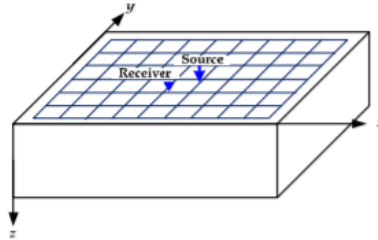
Figure 2.15: Test Mesh on the concrete specimen (Yeh and Liu, 2009).

For the horizontal cross-section, the B-scan required a single set of the impact-echo test along a test line. The image of the vertical section was attained by using a colour scale, and the 2D density plot was generated. The highest colour scale was noticed at the boundary, although a concrete crack was absent in the region. The lower mode vibrations induced this phenomenon. Figure 2.16 clearly illustrates the frequency spectra along the test line x = 16 cm and 40 cm. Depth spectral was necessary as the frequency spectra did not exhibit a clear cracking profile.

On the other hand, the spectral C-scan provided spectral amplitudes at any horizontal cross-section. Frequency spectral were transformed into depth spectral, so the amplitude peak in the depth interval range can be acquired. The red region depicted the location of the internal crack. A noticeable blue zone appeared in Figure 2.17 (c), while no crack was found in the region. This phenomenon was considered a shadow cast caused by the obstructing of the wave (Liu and Yeh, 2012).

However, this model has a significant drawback, which required a lot of impact echo test on the surface. The accuracy of the numerical model highly dependent on the number of tests conducted. The excessive amount of on-site testing leads to the low efficiency of remedy work.
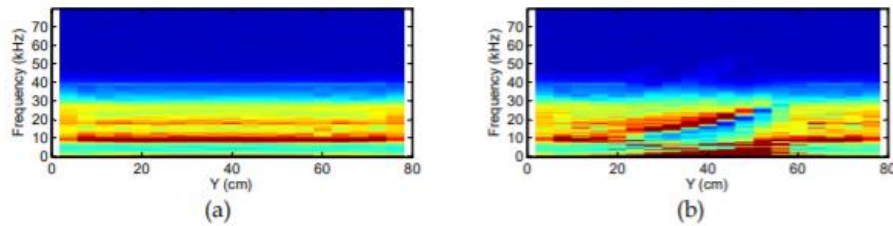
Figure 2.16: Spectral B-scan, the position of (a) 16 cm (b) 40 cm (Liu and
Yeh, 2012).
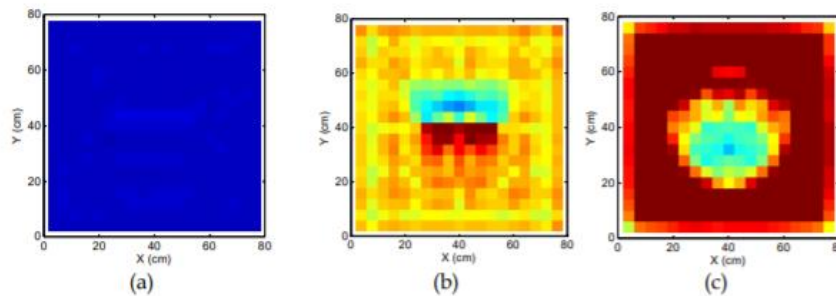
Figure 2.17: Spectral C-scan (a) z = 4 cm (b) z = 10 cm and (c) z = 20 cm (Liu
and Yeh, 2012).

2.6.3   Stack Image Based on Impact -Echo (SIBIE) model

Generally, the frequency response of the elastic wave using the non-destructive
test is highly dependent on the thickness of the specimen, the location of the
internal defect, and the velocity of the bulk wave. However, the recognition of
peak frequencies was demanding in the frequency spectrum. An imaging
procedure, called Stack Imaging of Spectral Amplitudes Based on Impact Echo
(SIBIE), was proposed to detect waveforms in the frequency domain. Firstly,
the cross-section of the selected test line was allocated into the square mesh.
The minimum dimension of each mesh for the SIBIE analysis was constrained
to $C_p \Delta t/2$, where C_p represents the velocity of P-wave, Δt represents the
sampling time. The resonance frequencies due to the reflections at each element
were obtained and computed. The spectral amplitudes corresponding to the
resonance frequencies were summed up to obtain the reflection intensity of each
element. The resonance frequency at a specific grid cell was expressed in
Equation 2.6 and Equation 2.7 (Tokai and Ohtsu, n.d.).

$$f_{crack} = \frac{C_p}{R} \tag{2.6}$$

$$f'_{crack} = \frac{C_p}{r_2} \tag{2.7}$$

where

f_{crack} = resonance frequency subjected to plate thickness, Hz

f'_{crack} = resonance frequency subjected to internal crack, Hz

R   = $r_1 + r_2$

r_1 = travel distance from the input, m

r_2 = travel distance from the output, m

However, the conventional SIBIE method came into a severe issue, where cracking in the cross-section depended on available output data. The two-dimensional image was expressed as symmetry because of the one-point detection of the impact echo method. Therefore, the scanning SIBIE procedure was proposed where the number of testing increases into three sets along the cross-section (Tokai, et al., 2009). The frequency spectrum was divided and arranged crosswise after the two-dimensional image was attained. The result illustrated the scanning SIBIE method's effectiveness in detecting non-vertical cracks such as zigzag crack and inclination crack. The crack tips and depths of the crack were detected compared to the conventional approach's symmetric image.

As a result, although the intensity of the grid at the proposed crack location was high, there were a few false messages given due to the symmetrical error. The scanning SIBIE method reduced the discrepancies by adding two more iterations of the impact-echo test. Nevertheless, the error from the image was apparent following with lower efficiency. Therefore, it is significant to consider the Rayleigh wave in detecting the crack location, potentially minimising the symmetrical error due to the reflective frequency. The result for the scanning SIBIE method is illustrated in Figure 2.18.

| (a) | (b) |
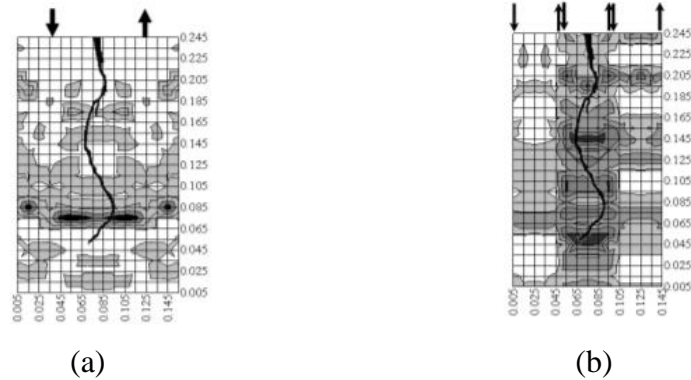
Figure 2.18: SIBIE images of zigzag type crack: (a) Conventional SIBIE; (b) Scanning SIBIE (Tokai, et al., 2009).

2.6.4 Stress Wave Tomography

Acoustic emission (AE) tomography analysis was employed in the repair analysis of the concrete structure. The internal defect in the concrete structure appeared as an obstruction against the propagation of the elastic wave. Hence, the slowness indicated the affected region in the concrete structure. AE tomography acquires the velocity distribution within the concrete specimen by finding the travel time between two sensors (Chai, et al., 2016). It demonstrates an assuring image of the damaged region, and the efficiency of repairing work was accelerated.

As shown in Figure 2.19, stress wave tomography was employed to evaluate the internal wood defect (Du, et al., 2015). Few assumptions were made in the study: the wave propagated in a straight line, and the affected zone was represented using a basic ellipse. The stress wave tomography method exemplified the defected region using spatial interpolation and velocity compensation based on flight data acquired from waveform data analysis. The ellipse-based spatial interpolation approach was employed to estimate the value of the grid cell nearby to the dissemination of velocity ray. Subsequently, the graph of the cross-section of the wood was reconstructed with the distinct value of velocity, which indicated the internal defect. The result showed the algorithm and the ellipse based spatial interpolation was simulating the motion of waveform in the medium. The velocity compensation was significant to understand the behaviour of propagating velocity respective to the parameters of the solid medium.
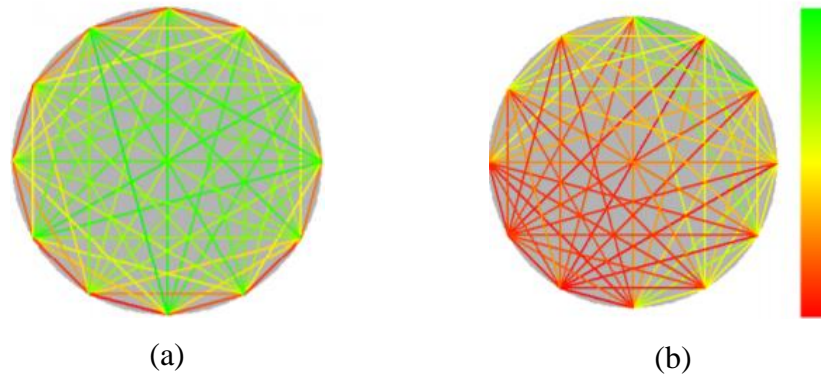
Figure 2.19: Stress Wave Tomography in (a) intact sample (b) damage sample (Du, et al., 2015).

2.7 Summary

In Chapter 2, the factors causing damage in the concrete structure were discussed. There are several non-destructive tests proposed by researchers with different equipment and computational approaches. Sensors such as Radio Frequency Identification Technology and Soft Elastomeric Capacitor only serve as a crack detection tool and fail to provide precise information about the crack size and position in the medium. The image processing method utilizing a Terrestrial Laser Scanner is an excellent way for crack mapping, but it is limited to surface crack. This approach is also questionable on the high computational cost, as stated by the author. Therefore, pulse wave detection method such as ultrasonic pulse velocity and impact echo is the most suitable crack mapping test method.

The type and behaviour of stress wave propagating in the medium were reviewed to improve the elastic wave method on crack mapping prediction. Rayleigh wave and pressure wave were studied for surface crack and internal crack detection, respectively. The simulation and numerical models were conferred and contrasted. Due to the limitation on the on-site test iteration and equipment available, stress wave tomography and the SIBIE method was employed and modified to achieve a reliable three-dimensional crack mapping model.

Lastly, the heterogeneity properties of concrete were respected in the simulation of the concrete specimen in mesoscale. The random distribution of concrete parameters such as Young modulus, tensile strength, and shear

modulus over the concrete medium was reviewed. The multiparameter correlated field can be simulated through Python to determine the value of each parameter on the grid mesh. The parameters such as lame constant, modulus of elasticity and shear modulus are crucial to the effect of a waveform propagating in the concrete medium. Table 2.3 summarizes all the proposed crack imaging model with their respective functions.

Table 2.3 Summary of Crack Mapping Models.

Author	Description	Crack Mapping Model
Shah, et al., 2018	Ultrasonic based crack imaging in concrete	Finite Difference Discretization Method
Ganguli, et al., 2012	Synthetic aperture imaging for flaw detection in a concrete medium	Synthetic Aperture Focusing Technique
Yeh and Liu, 2009	Imaging of internal cracks in concrete structures using the surface rendering technique	B-scan and C-scan
Tokai and Ohtsu, n.d.	Evaluation of the surface crack depth in concrete by Impact-Echo procedures (SIBIE)	SIBIE method
Tokai and Ohtsu, 2009	Estimation of surface-crack depth in concrete by scanning SIBIE procedure	Scanning SIBIE method
Chai, et al., 2016	Development of a tomography technique for assessment of the material condition of concrete using optimized elastic wave parameters	Stress Wave Tomography
Du, et al., 2015	Stress wave tomography of internal wood defects using ellipse-based spatial interpolation and velocity compensation	Stress Wave Tomography

CHAPTER 3

METHODOLOGY

3.1 Introduction

This chapter provides an in-depth illustration that demonstrates the details of the report. Firstly, two conceptual formulations were specified to ascertain the crack region of the concrete specimen in the surface and cross-section, respectively. A noble coefficient was introduced to integrate the models into a complete three-dimensional (3D) crack imaging algorithm. Since the mesoscale level of interest was considered in the analysis, the random distribution of Young's Modulus and Poisson Ratio were identified using Python. Furthermore, the simulation to obtain the time and frequency of the wave, including the delta method and wave simulation in ABAQUS, were discussed in this chapter. The flowchart of the methodology is illustrated in Figure 3.1.

3.2 Surface Crack Analytical Model

In the findings of crack detection approach by recent research such as the effect of crack on pressure wave (Wei, et al., 2013) and assessment of Rayleigh wave characteristic on sub-surface crack (Lee, et al., 2016), the characteristics in terms of velocity and amplitude of Rayleigh wave decrease subjected to crack. Therefore, the velocity difference of the Rayleigh wave was employed to determine the crack region.

The hammer strike at any sensor points, and the elastic wave is introduced into the concrete medium (ASTM C1383-15, 2015). All other sensors function as a receiver. The travel time of the surface wave was collected in a matrix form, as demonstrated in Figure 3.2, which was represented by the arrival time of the first burst peak observed. The procedure repeated for every location of sensors until every set of data was acquired. The time-of-flight data is illustrated in a matrix form as expressed in Equation 3.1 (Du, et al., 2015).

$$t_{ij} = \begin{bmatrix} t_{11} & t_{12} & ... & t_{1N} \\ t_{21} & t_{22} & ... & t_{2N} \\ ... & ... & ... & ... \\ t_{N1} & t_{N2} & ... & t_{NN} \end{bmatrix} \qquad (3.1)$$

where

N   = total number of sensors

t_{ij} = travel time from sensor *i* to sensor *j, s*
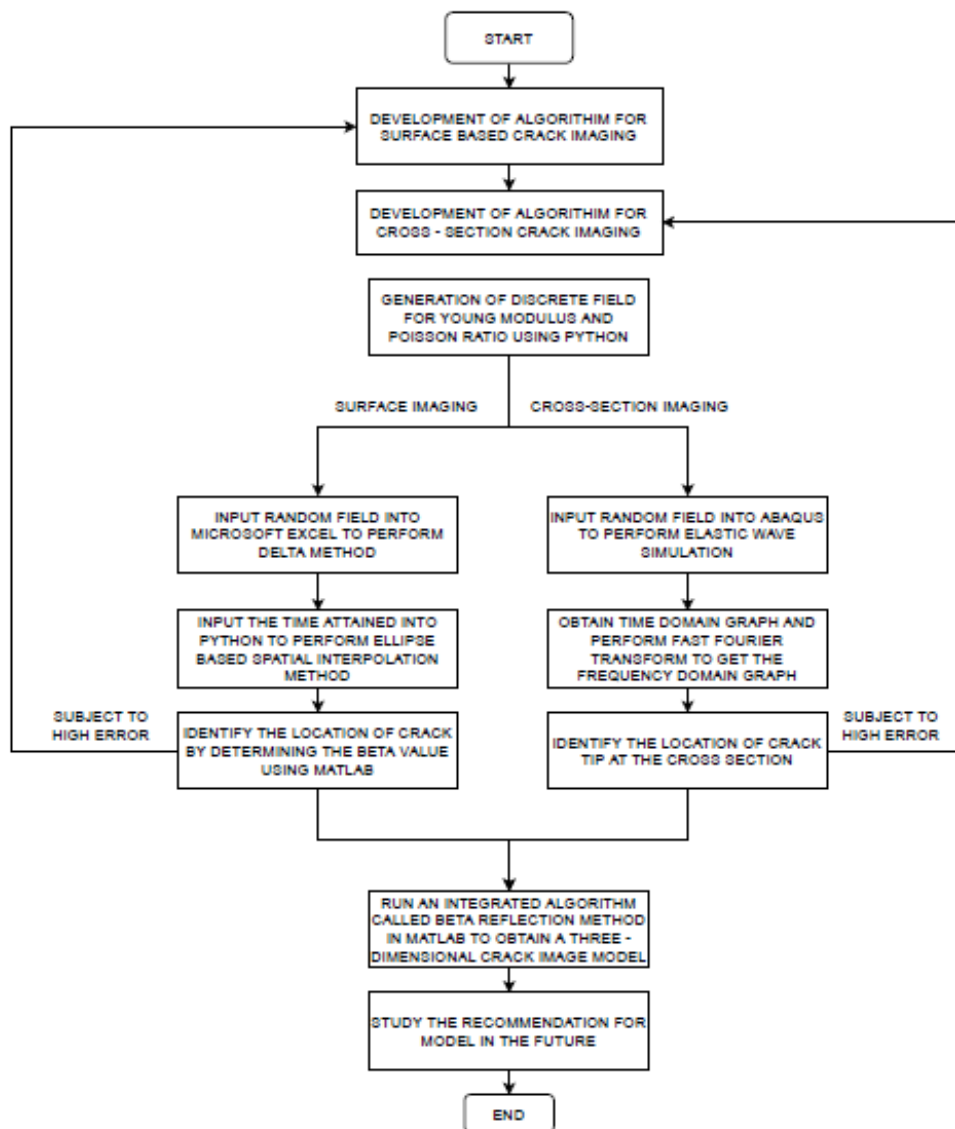
Figure 3.1: Flowchart of Methodology.
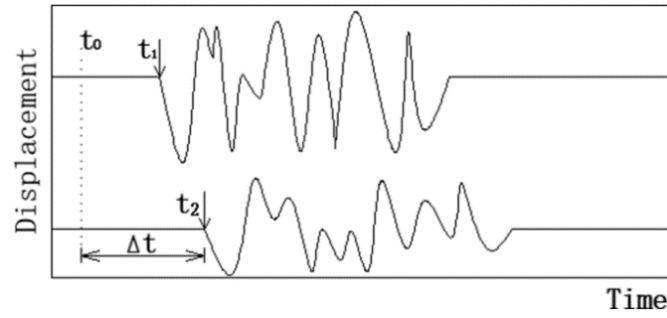
Figure 3.2: Arrival Time of Surface Wave (Rayleigh wave) (Sun, et al., 2018).

3.2.1 Velocity Tomography

The velocity of an elastic wave propagating in the concrete medium was computed in Equation 3.2.

$$v = \frac{\text{distance}}{\text{time}} \qquad (3.2)$$

By using Equation 3.3 (Du, et al., 2015), it presented the accumulated geometric information of the cross-section to achieve tomography. The transmission wave velocity between any two sensors was derived into matrix form and expressed as below (Du, et al., 2015).

$$v_{ij} = \begin{bmatrix} 0 & v_{12} & \dots & v_{1N} \\ v_{21} & 0 & \dots & v_{2N} \\ \dots & \dots & \dots & \dots \\ v_{N1} & v_{N2} & \dots & 0 \end{bmatrix} \qquad (3.3)$$

where

v_{ij} = propagation velocity from sensor i to sensor j, m/s

3.2.2 Ellipse-Based Spatial Interpolation

The ellipse-based spatial interpolation method is developed in Python, as shown in Appendix C. The flow of the entire algorithm is shown as follows:

i. The number and location of sensors were initialized on the surface of the specimen.

ii. The time-of-flight from the Impact-Echo method was stored as an input of data.

iii.   The shape of the ellipse (coverage) for each velocity ray was determined.

iv.   The experimental velocity was compared with the theoretical velocity to identify the presence of the crack in the grid cell.

v.   The variance was calculated and insert into the grid cell as a Beta value.

vi.   The surface tomography was constructed after the mean-variance of every grid cell was identified.

Each velocity ray between pairs of sensors intersected in a grid cell. Thus, spatial interpolation is a constructive approach to reconstruct the crack region image of the concrete surface by calculating the accumulated velocity in each grid (Du, et al., 2015). Spatial interpolation is denoted as an estimation of value at a discrete point using the known value points. According to the study of Feng, et al. (2014), the approximation of the new grid cell utilized the computation of every intersection between two velocity ray. The result was unsatisfying and failed to present the exact location of the internal defect.

Hence, a spatial interpolation method using ellipse was introduced where each velocity ray covered the affected zone, as shown in Figure 3.3. The form of the affected zone was based on a basic ellipse (Du, et al., 2015). If a specific grid cell was affected by velocity rays instantaneously, the velocity value for each grid cell was computed based on the weightage.
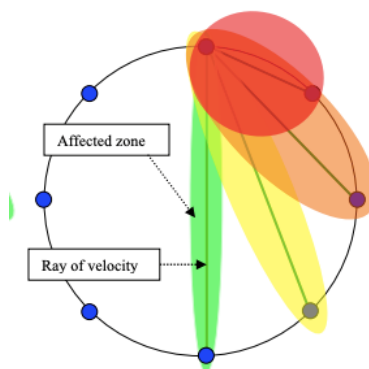
Figure 3.3: Fundamental Illustration of Spatial Interpolation using Ellipse (Du, et al., 2015).

The area of the basic ellipse altered was corresponding to the distance between two sensors. The area of the affected zone was subjected to a shorter ray that is more extensive. Thus, the shape of each affected zone was expressed in Equation 3.4 (Du, et al., 2015).

$$b_{ij} = c_{ij} \times a_{ij} \qquad (3.4)$$

where

b_{ij} = shorter axis of the basic ellipse, m

a_{ij} = longer axis of the basic ellipse, which is known as the distance between two sensors, m

c_{ij} = eccentricity of the basic ellipse, which acts as a controlling coefficient for a specific ray, given in Equation 3.5 (Du, et al., 2015).

$$c_{ij} = \begin{cases} 1 - [|j-1|]/(N-2) & |j-1| < (N/2) \\ 1 - [N - |j-1|]/(N-2) & |j-1| > (N/2) \\ 0.1 & |j-1| = (N/2) \end{cases} \qquad (3.5)$$

where

N = total number of sensors

Furthermore, the effect of velocity rays on a specific grid cell was computed in Equation 3.6 (Du, et al., 2015).

$$P_{ij} = \begin{cases} 0 & \dfrac{D_{xb}{}^2}{a^2} + \dfrac{D_{ya}{}^2}{b^2} \leq 1 \\ 1 & \dfrac{D_{xb}{}^2}{a^2} + \dfrac{D_{ya}{}^2}{b^2} > 1 \end{cases} \qquad (3.6)$$

where

D_{xb} = distance between a grid cell and short axis of the ellipse

D_{xb} = distance between a grid cell and the long axis of the ellipse

When an individual grid cell was affected by multiple velocity rays simultaneously, all corresponding rays were computed. However, the weightage of affected rays depended on the shortest distance between the grid cell to the velocity ray. Hence, the weighting coefficient is expressed in Equation 3.7 (Du, et al., 2015).

$$w_k = (\frac{1}{D_{ya}}) \sum_{k=1}^{m} \frac{1}{D_{ya}} \qquad (3.7)$$

where

l_k = length of particular ray, m

l_z = length of other corresponding rays, m

3.2.3 Variance of Velocities

When the velocity ray between each pair of sensors propagated through the crack, it was deflected, causing a delay in velocity. Hence, the velocity variance was crucial to determine the crack in a particular location of the specimen. The variance of each grid cell was computed using the Equation 3.8 below.

$$Variance = \frac{|V_{theoritical} - V_{experimental}|}{V_{experimental}} \qquad (3.8)$$

The variance was computed using the colour map function in Python. Hence, the grid cell with the maximum value of variance was coloured with red which defined the potential crack region. On the other hand, the low variance region was coloured with blue, which illustrated the intact region of the specimen.

3.3 Cross-Section Analytical Model

The determination of crack depth is a challenging work after the crack region was determined using velocity tomography. The C-scan technique and stack image based on Impact-Echo (SIBIE) approach were employed to identify the crack tip location in a defect specimen from the works of researchers. Hence,

the Pressure wave frequency is an important parameter to assess the concrete condition in the sub-surface. A newly developed algorithm was developed, which was called as beta reflection method. The result was discussed in terms of accuracy and efficiency.

3.3.1 Beta Reflection Method

The Beta reflection method was constructed in MATLAB to identify the crack depth. The flowchart for the whole model is illustrated as:

    i.   The Fast Fourier Transform graph was generated and plugged into the database.

    ii.   The beta value was extracted from the corresponding surface tomography.

    iii.   The relative frequency for each grid was identified with different depth.

    iv.   The relative amplitude was obtained from the corresponding relative frequency from the FFT graph.

    v.   The beta value was integrated with the relative amplitude to construct a three-dimensional crack imaging model.

    vi.   A cross-section image was attained from the 3D model to carry out the crack depth analysis.

The frequency of pressure wave is an important parameter to assess the condition within the concrete structure. When the wave propagates in the medium, the flaw of concrete deflects or reflect the direction of wave transmission. The relative frequency of each grid cell was expressed in Equation 3.9 (Tokai and Ohtsu, n.d.).

$$f_T = \frac{2C_p}{nd} \tag{3.9}$$

where

f_T = the relative frequency of each grid cell,

C_p = the velocity of the wave,

d   = the depth of each grid cell.

n   = boundary coefficient depending on the type of material

When the relative frequency of each grid cell was attained, the amplitude of each corresponding relative frequency was determined from the frequency domain graph. The location of the crack in the medium was determined. Hence, a complete three-dimensional crack imaging model was developed by integrating the relative amplitude with the variance obtained from the surface crack model.

3.4   Specification of Specimen

A concrete specimen was prepared with dimension (600 × 600 × 200 mm) for numerical model simulation, as shown in Figure 3.4. The wavelength produced by the impact echo is in the range of 50 mm to 2000 mm. Hence, the minimum thickness of the concrete slab is two times the wavelength which is 100 mm. Three types of concrete defect were proposed to contrast and verify the capability of this crack imaging model.

Three types of defect were proposed in the simulation, including 15 cm crack, 10 cm crack and 12.5 cm internal void, to study and verify the newly developed algorithm. The proposed defects mimicked the actual potential defects in the concrete, as shown in Figure 3.5.
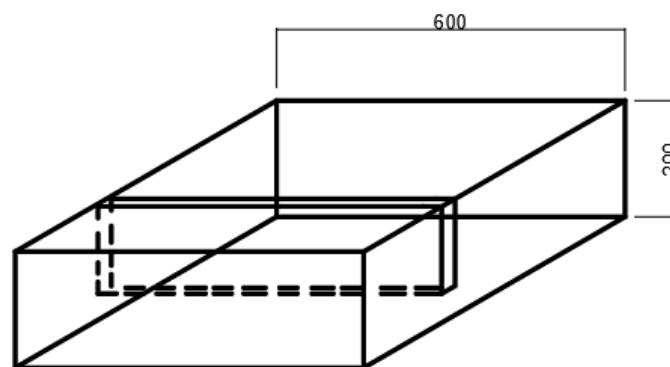
Figure 3.4: Specification of Concrete Specimen.

(a)

(b)

(c)
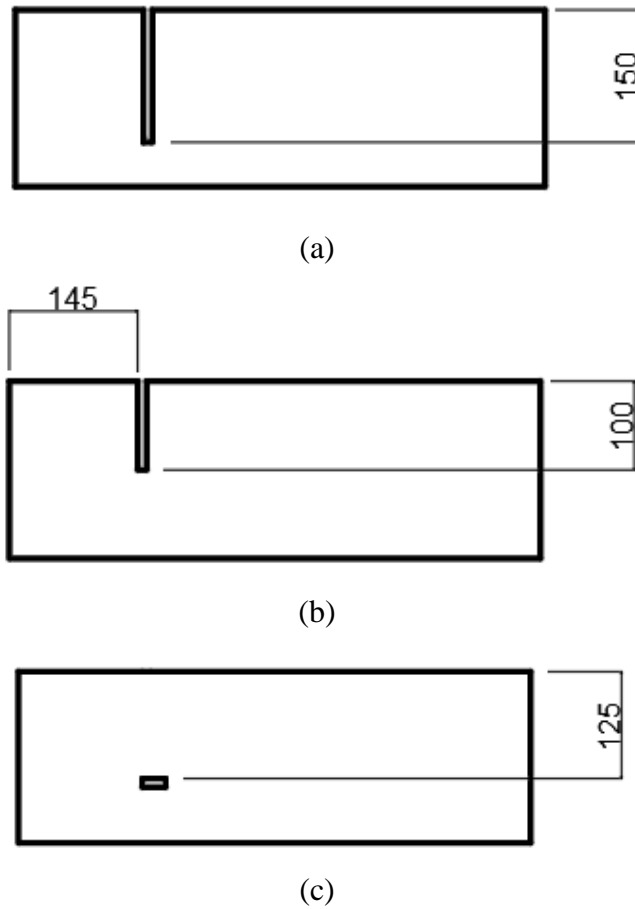
Figure 3.5: The Illustration of Artificial Crack: (a) 15 cm Crack, (b) 10 cm
Crack and (c) 12.5 cm Void

3.5   Delta Method

The time taken for wave transmitting along each pair of sensors is required to
carry out the velocity tomography for the surface crack imaging model.
Therefore, two numerical simulations were proposed: using the Delta method
and wave simulation in finite element analysis. Firstly, the configuration of
sensors on the surface of the concrete specimen was determined and
demonstrated in Figure 3.6.
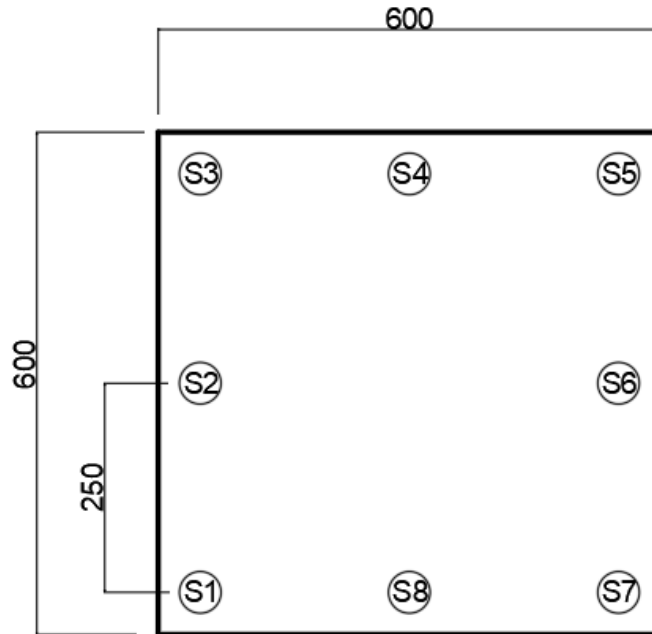
Figure 3.6: Arrangement of Sensors on the Concrete Specimen.

Delta method defines the transmission time by considering the crack between oscillator and receiver. Therefore, the reverse calculation method using try and error was carried out in Microsoft Excel to obtain the transmission time of elastic wave propagates between oscillator and receiver. The formula for the Delta method is expressed in Equation 3.10 (FPrimeC, 2019).

$$d \; = \; \sqrt{\frac{T^2 - R^2 + (V \times t)^2}{2V \times t} - T^2} \qquad (3.10)$$

where

T   = distance from crack to oscillator, mm,

R   = distance from crack to receiver, mm,

V   = speed of the elastic wave in the undamaged medium, mm/s,

t   = transmission time between oscillator and receiver, s.

3.6   Wave Simulation in ABAQUS

Researchers had shown that the modelling result agreed well with the predicted one-dimensional solutions connecting the numerical and theoretical studies on crack detecting approaches. In this paper, impact echo simulation of the intact

specimen was carried out and compared with the models with three different types of artificial crack. Various researchers performed the finite element method using ABAQUS due to its high capability on dynamic explicit solving.

3.6.1   Specification of Model

Finite element analysis was carried out to simulate elastic wave propagation in a concrete specimen using ABAQUS software. Two-dimensional planar models were employed to apply the impact loading on the surface of the solid specimen. The model's characterisation was necessary so the analysis of elastic wave properties in concrete specimen could be precisely simulated. The model parameters were tabulated in Table 3.1.

Table 3.1: Material Properties of Concrete in ABAQUS (The Engineering
          Toolbox, 2008).

	Density (tonne/mm^3)	Young's Modulus (N/mm^2)	Poisson Ratio
Concrete	2.4 E -5	2.9 E+9	0.2

The 2D constructed model in ABAQUS is presented in Figure 3.7. A 600 mm by 200 mm deformable solid was constructed to represent the concrete slab's cross-section with a 4-node bilinear plane stress quadrilateral (CPS4R). The distortion and hourglass control for the element was selected as default. An element size of 10 mm was employed uniformly throughout the model. For the defective models, the artificial cracks and void were extruded.
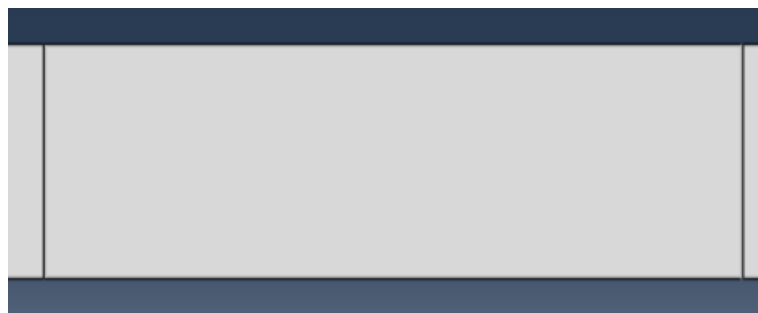
Figure 3.7: Two-Dimensional Planar Model in ABAQUS.

3.6.2 Loading and Boundary Conditions

In the loading stage, the explicit dynamic analysis method was employed. The total step time was 2.048 millisecond. Time increment size was limited to capture the smallest natural period of interest. The critical time increment size was commonly computed by using Equation 3.11 (Lee, 2019).

$$\text{Max Time Increment } = \frac{\text{Element size}}{\text{Velocity of wave}} \qquad (3.11)$$

The velocity of the wave in the simulation was 3626.6 m/s transmitting through 10 mm mesh. The maximum time step was 2.7 µs. Hence, 2048 increments were captured with 1 µs time increment. The impact duration was 32 µs, as shown in the amplitude graph below. The maximum load value of 8 N was applied as a point load on the surface of the solid specimen, as shown in Figure 3.8.
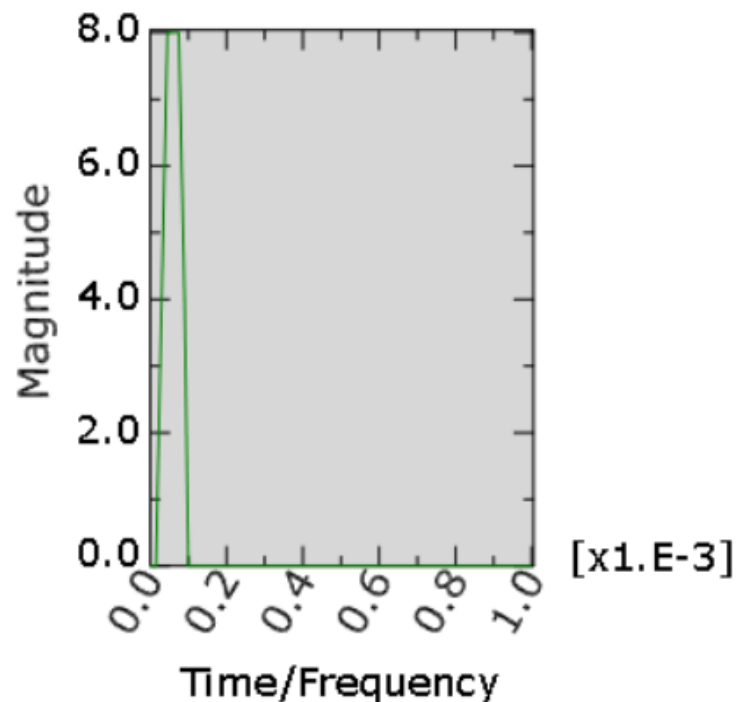
Figure 3.8: Impact Duration Graph.

Furthermore, the pinned boundary condition was established for the bottom of the specimen and the artificial crack, as shown in Figure 3.9. The boundary condition was crucial to reflect the wave at the boundary and crack in

the specimen. However, redundant reflections of the wave at both sides of the specimen tended to generate noises, resulting in high discrepancy. Both sides of the specimen were extended five times the specimen's width to create a non – reflective boundary. The non–reflective boundary condition was shown in Figure 3.9 below.

Figure 3.9: Boundary Condition.

3.6.3   Fast Fourier Transform

The Fast Fourier Transform is an optimized measurement method for acoustics wave measurement. It transforms the signal into frequency components and thereby provides the frequency domain information of the signal. The time-domain signal was sampled over the total time step and separated into the spectral components. Hence, the FFT is vital to convert the time domain graph of the wave signal into a frequency domain graph for analysis processes.

3.7   Random Field Distribution

The theoretical longitudinal velocity at a given grid cell is dependent on the first and second lame constant of the concrete specimen. In this experiment, the mesoscale level of interest was targeted to identify the distribution of parameters over the concrete. If the heterogeneity properties of concrete were considered, the longitudinal velocity of the elastic wave propagating in the concrete medium diverged along with the concrete medium. The materials properties of the elastic medium are tabulated in Table 3.2.

Table 3.2: Material Properties of Concrete (The Engineering Toolbox, 2008).

Material	Young modulus, E (GPa)	Poisson Ratio, v
Concrete	14 to 41	0.1 to 0.2

Therefore, a random field simulation was conducted using the function in the Python software to distribute the elastic modulus (E) and Poisson ratio (v) over the surface of the specimen (Constantine, 2012). The longitudinal velocity for each mesh was calculated using the first and second lame constant from Equation 3.12 and Equation 3.13 (Chai, et al., 2016).

$$\mu = \frac{E}{2(1 + v)} \tag{3.12}$$

$$\lambda = \frac{Ev}{(1 + v)(1 - 2v)} \tag{3.13}$$

The longitudinal wave speed in each medium was given as Equation 3.14 (Chai, et al., 2016):

$$V_L = \sqrt{\frac{\lambda + 2\mu}{p}} \tag{3.14}$$

3.8   Summary

The lognormal random field distribution was generated in Python for the surface and cross-section model. The Delta method and elastic wave simulation in ABAQUS were simulated to attain the Rayleigh wave velocity and Pressure wave frequency. Six models were constructed and compared in Chapter 4:

i.   15 cm crack deterministic and stochastic models.

ii.   10 cm crack deterministic and stochastic models.

iii.   12.5 cm void deterministic and stochastic models.

The surface tomography and cross-section crack image were integrated into a comprehensive three-dimensional model. The results were discussed and contrasted among the preceding model to verify the performance of the newly developed conceptual formulation.

CHAPTER 4

RESULTS AND DISCUSSION

4.1 Introduction

This paper studied the conceptual formulation of crack mapping prediction, which can be employed in the construction field. The ellipse-based spatial interpolation and beta reflection methods were used to image the surface and cross-section crack propagation. In this paper, four concrete specimens were probed, including an undamaged sample as the control experiment, concrete with 15 cm crack, 10 cm crack and 12.5 cm void. Besides, this study included a stochastic model considering the random field distribution of young modulus and Poisson ratio. The result was compared with the deterministic model to determine the importance of simulating the heterogeneity of the concrete. Due to the limitation of the Covid-19 pandemic condition, the elastic wave non-destructive test in the laboratory was replaced by numerical simulation such as the Delta method and elastic wave simulation in ABAQUS. With the aid of both imaging techniques, a comprehensive three-dimension crack imaging model was developed. However, the results of surface and cross-section crack image were discussed in a two-dimensional contour plot for ease of reading.

4.2 Random Field Distribution

In this study, the concrete specimen's numerical simulation was analysed deterministically and stochastically to identify the importance of heterogeneous concrete properties. Two correlated parameters, such as Young's modulus and Poisson ratio, were lognormally distributed using a Python random field program. The mean values and correlation length of these parameters have been taken as the deterministic value shown in Chapter 3. The lognormal random field was separated into surface and cross-section analysis.

4.2.1 Surface Random Field

An initial random field containing 3600 meshes (600 mm by 600 mm dimension with 10 mm meshes) was modelled, and the values of Young's modulus and Poisson ratio were assigned to each mesh. The stochastic analysis was performed by calculating the mean value of 10,000 plain Monte Carlo samples. Figure 4.1 shows the lognormally distributed random field of two correlated parameters.
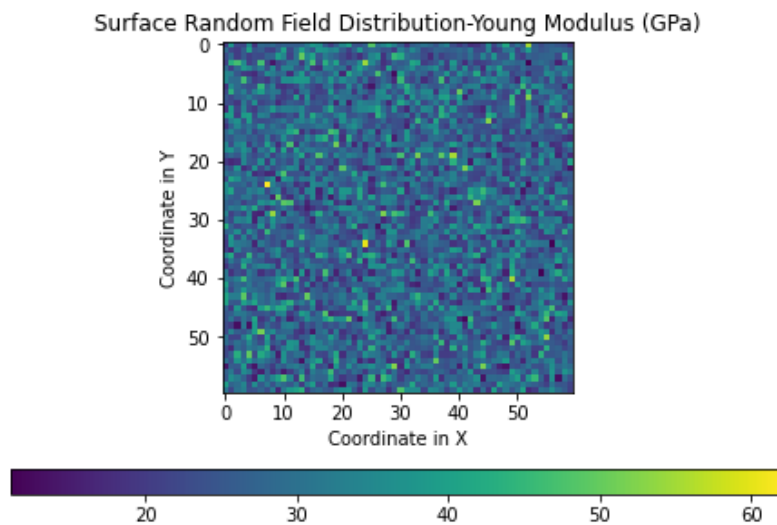
(a)
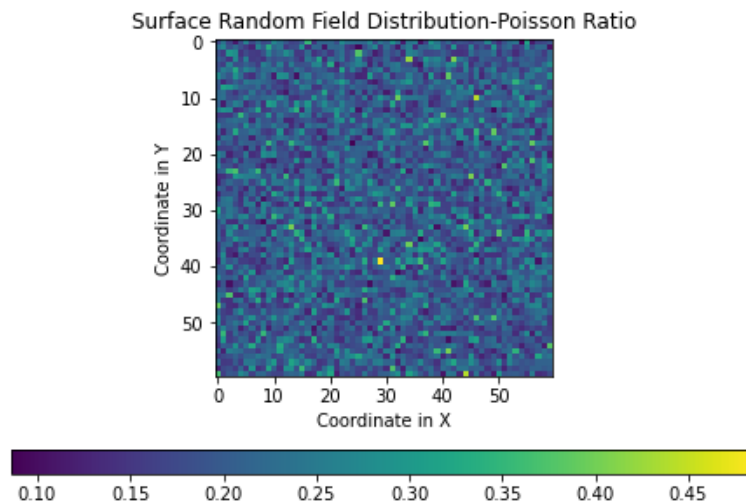
(b)

Figure 4.1: Lognormally Distributed Random Field of (a) Young's Modulus (in GPa) and (b) Poisson Ratio.

The range of Young's modulus felt between 12 GPa to 61 GPa while Poisson Ratio ranged between 0.086 to 0.486. The result indicates the random distribution of engineering properties for each mesh. Compared to a deterministic model, the engineering properties differ over the sample, simulating the heterogeneity properties of concrete due to the arbitrary distribution of cement particle, aggregate, and void. This field contributes to the comparison of wave propagation in the deterministic and stochastic models in the following methodology. The Probability Density Function (PDF) and histogram for both parameters are plotted in Figures 4.2 (a) and (b).
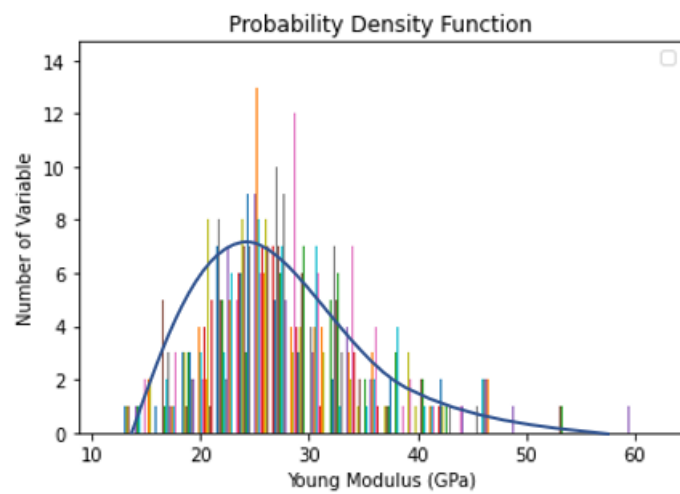
(a)
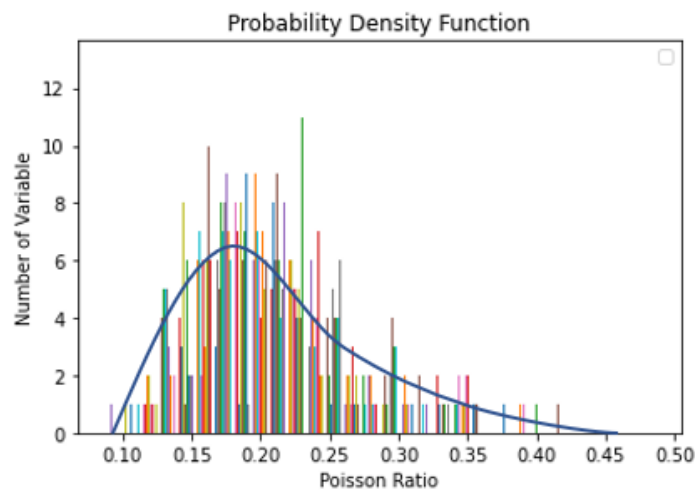
(b)

Figure 4.2: Histogram and Probability Density Function for (a) Young's Modulus (GPa) and (b) Poisson Ratio.

The mean value and the standard deviation of Young's modulus were 28.1886 GPa and 50.3527 GPa, where the corresponding values for the Poisson ratio were 0.2056 and 0.00263. The data appears to confirm the lognormal distribution of engineering properties from the simulation. The trend agrees well with the remarks from Torrent (1978), where the lognormal distribution is decent in representing the characteristic values of concrete.

4.2.2 Cross-Section Random Field

Figures 4.3 and 4.4 demonstrate the random field, PDF, and histogram of the engineering constant.
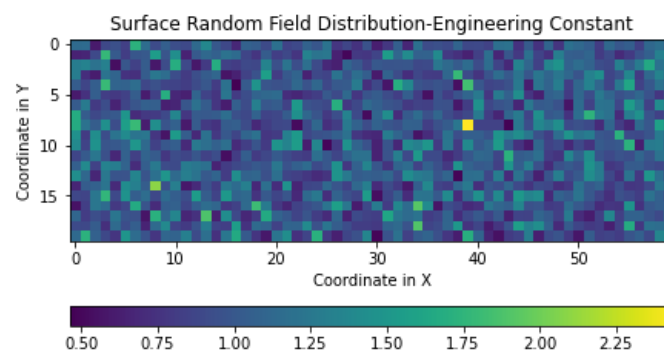
Figure 4.3: Lognormally Distributed Random Field of Engineering Constant.
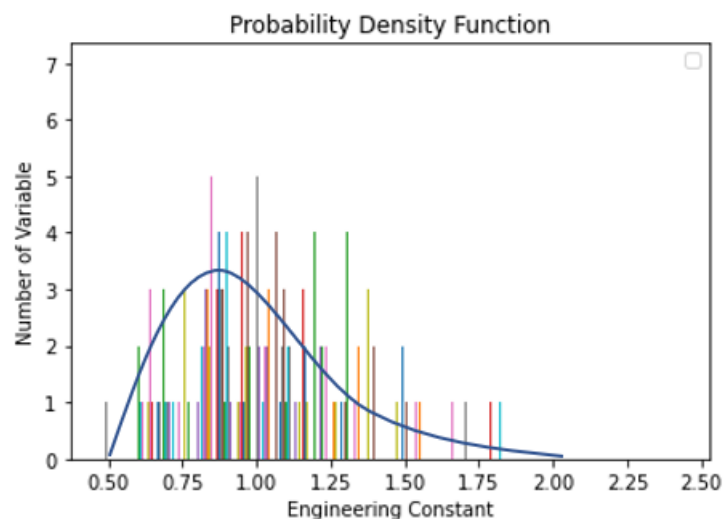
Figure 4.4: Histogram and Probability Density Function for Engineering Constant

The mean and variance of the engineering constant are 1.0242 and 0.06762, respectively. The PDF validates the lognormal distribution, which has a near-identical trend with the Young's Modulus and Poisson ratio. The engineering constant was utilized in the ABAQUS simulated model to characterize the random field distribution.

4.2.3 Summary

The deterministic and stochastic values of these concrete properties were analyzed and tabulated in Table 4.1. According to the table below, the percentage difference between deterministic and stochastic average value fell within 5 %, which had verified the lognormal distributed random distribution's validity. The stochastic material properties were substituted into the numerical model to acquire the time and frequency of wave simulation. It is essential to consider the random field distribution in the numerical model to enhance the numerical model towards actual concrete samples.

Table 4.1: Mean and Variance from Lognormal Distribution.

	Deterministic value	Stochastic Value			Percentage Difference between Mean
		Mean	Variance	Range	
Young's Modulus, GPa	27.5	28.1886	50.3527	12 to 61	4.21%
Poisson Ratio	0.2	0.20559	0.00263	0.086 to 0.486	2.72%
Engineering Constant	1.0	1.0242	0.06762	0.463 to 2.438	2.36%

4.3 Result from Delta Method

Delta method is a simple mathematical solution to acquire the wave transmitting time through the specimen medium. The input of theoretical velocity was calculated through the longitudinal wave formula and tabulated in Table 4.2 below.

Table 4.2: Input Velocity for Delta Method.

	Deterministic Model	Stochastic Model
Velocity (m/s)	3535.8	3251.2 to 4187.13

The time arrival for each set of sensors was calculated using the trial-and-error method in Microsoft Excel. By knowing the crack location based on the theoretical assumption, the arrival time was attained considering the velocity and distance between the two sensors. The stochastic model presented the fluctuation of velocity due to the random field. The results of the Delta method are presented in Appendix A. From Figure 4.5 to Figure 4.8, a discussion has been made comparing arrival time in different situations.
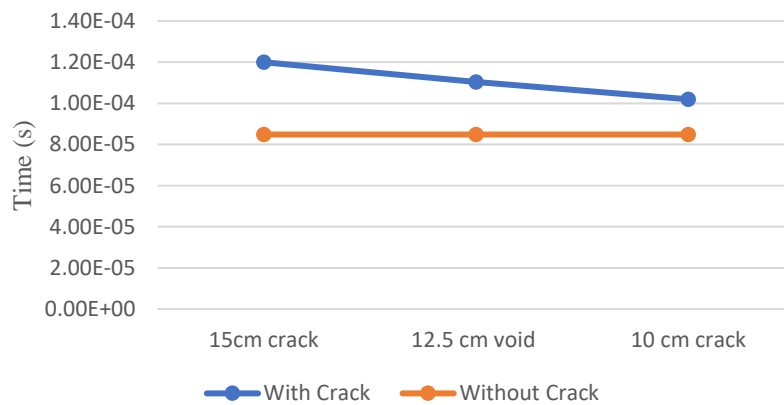
Figure 4.5: Comparison of Time Arrival (Deterministic Model).
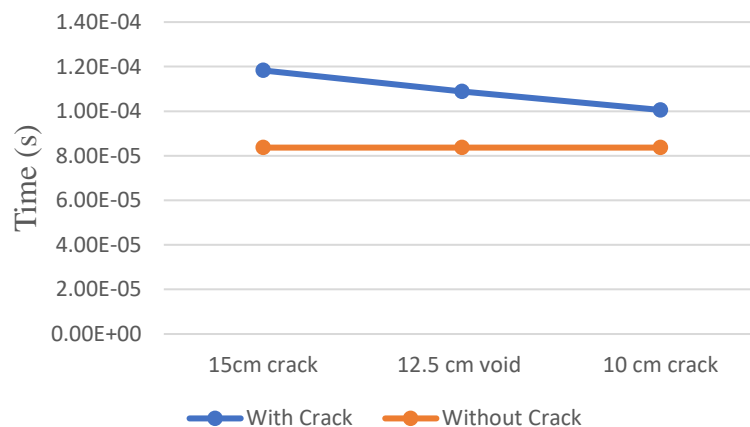
Figure 4.6: Comparison of Time Arrival (Stochastic Model).

As shown in Figure 4.5 and Figure 4.6, the wave propagating through the pathway with crack took a longer time when compared to the pathway without crack. These results appear to confirm that the flaw in concrete obstructs the motion of the wave in the medium. The identical trends are attained from both models showing that crack detection is significant over the external factors.
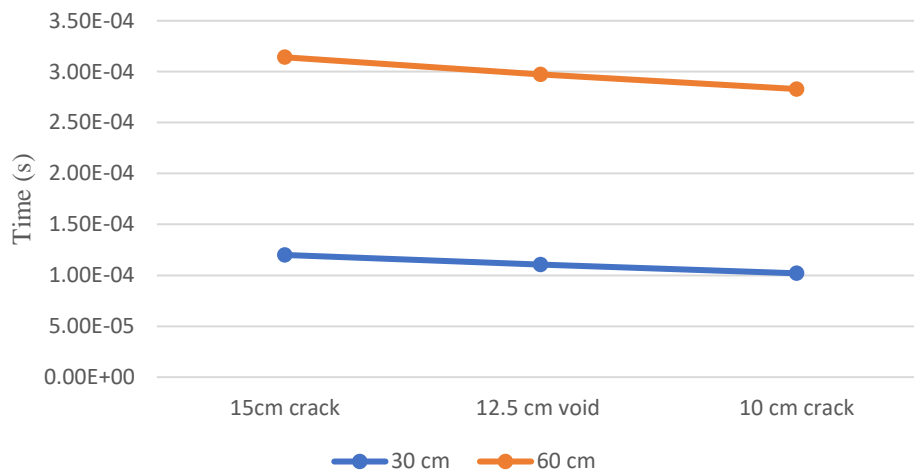
Figure 4.7: Comparison of Time Arrival with Different Distance between
Oscillator and Sensor (Deterministic Model).
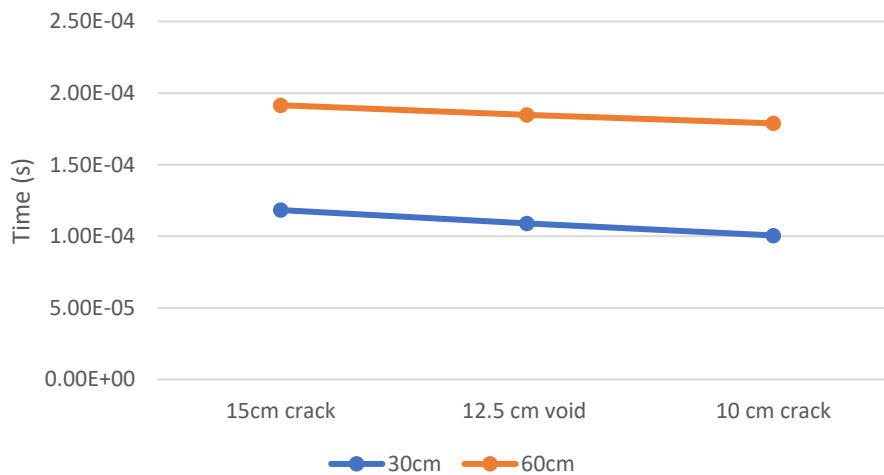
Figure 4.8: Comparison of Time Arrival with Different Distances between
Oscillator and Sensor (Stochastic Model).

Figure 4.7 and Figure 4.8 present the arrival time of the wave against the different crack depth. The difference in the arrival time between both cases increased with the defections' depth. It provides a shred of clear evidence that

the displacement of the wave propagating in the medium escalates with increasing depth. Contrary to expectations, the Delta Method results are agreeing and capable of employing in the proposed algorithm.

The fundamental idea considering the heterogeneity of concrete properties in this paper is to identify the legitimacy of this model against real-life crack mapping applications. The fluctuation of wave velocity transmitting through the concrete medium was acquired. However, the response of the wave against the subsurface crack or interval void was noticeable. For both deterministic and stochastic models, the arrival of the wave is delayed due to the crack among the wave transmission paths. Consequently, the estimation of crack presence in concrete could be attained by computing the wave propagating velocity across numerous sets of sensors. It is believed that the different crack depths could be observed in the numerical model.

4.4   Result from Finite Element Analysis (FEA) in ABAQUS

The determination of crack depth is a vital key in a three-dimensional imaging model. The crack tip location using the Rayleigh wave is challenging as it is way below the surface exceeding the penetration depth of the wave. The pressure wave is a decent option to identify the depth of internal defect in concrete specimen. The P-wave transmitted through the specimen and reflected at the boundary. The frequency of P-wave is an essential parameter to determine the reflection point within the medium. Hence, the ABAQUS software was employed in this paper to study the elastic wave propagation in different scenarios. Figure 4.9 illustrates the motion of wave simulation in the computational environment. (a) The elastic wave was triggered when the impulse load applied at the node and the contour of the wave. (b) When the P-wave extended to the edge of the structure, the movement of the wave reflected. (c) Therefore, as soon as the wave impacted at an internal defect, the wave replicated at the void structure boundary. As a result, the model of wave simulation in ABAQUS software agreed well with the law of elastic wave transmission, and the results of the simulation were employed to build up the crack imaging model.

(a)

(b)

(c)
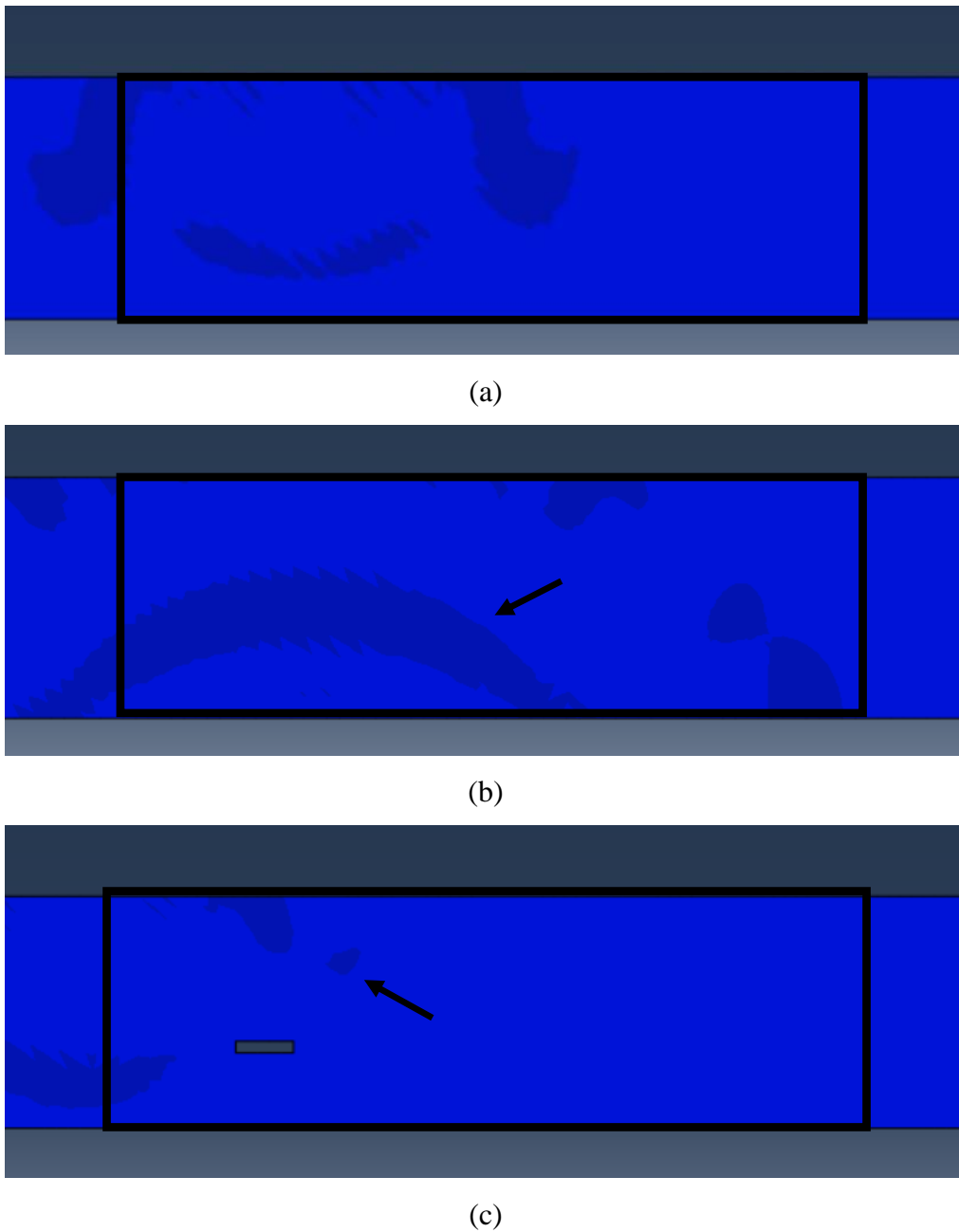
Figure 4.9: Simulation of Wave Propagation in ABAQUS: (a) Excitation Stage
(b) Reflection of Wave at Boundary (c) Reflection of Wave due to
Internal Defection.

4.4.1 Time Domain

Figure 4.10 to Figure 4.16 present the time-displacement graph of elastic wave
simulation in ABAQUS. The results were discussed by comparing the time
taken of the wave propagating through different mediums.
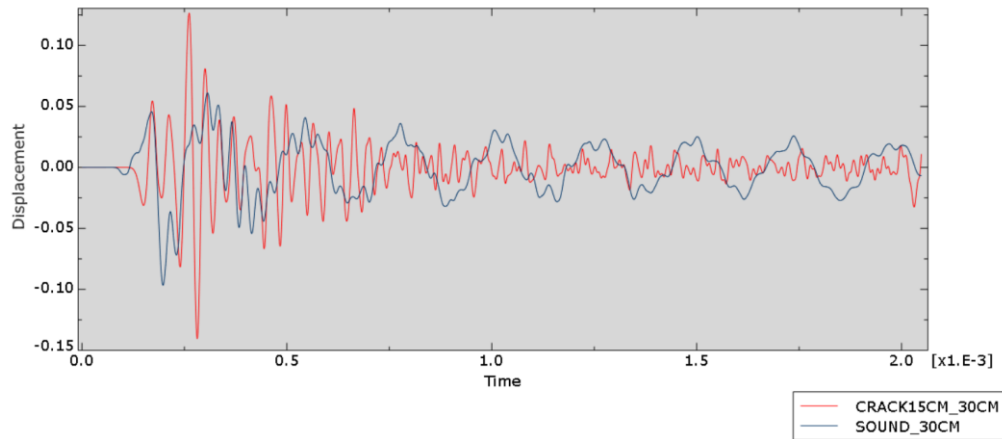
Figure 4.10: Time-Displacement Graph (Comparing Sound Specimen and 15 cm Crack Specimen).
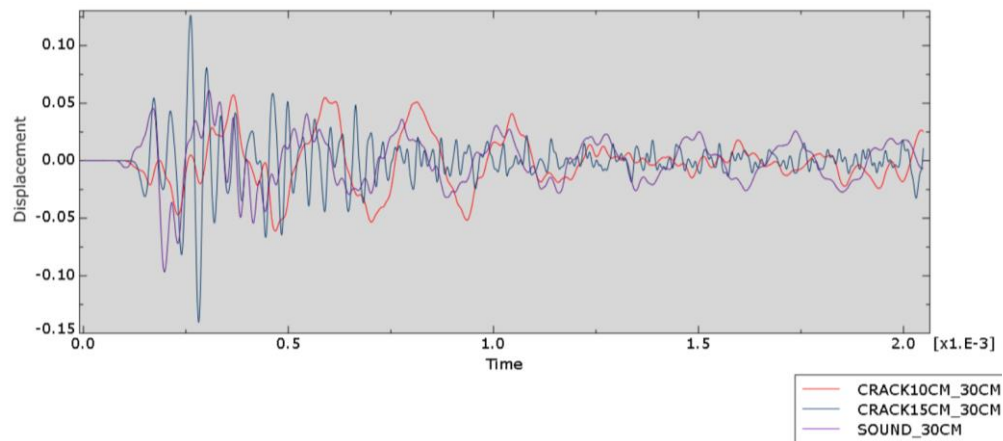
Figure 4.11: Time-Displacement Graph (Comparing Sound Specimen, 15 cm Crack Specimen and 10 cm crack specimen).

Figure 4.10 and Figure 4.11 compare the arrival time for the wave to propagate through different crack depths with a constant distance between two sensors which is 30 cm. The time taken for wave transmitting were 29 ms, 32 ms, and 41 ms for the intact, 10 cm crack and 15 cm crack samples. These data show that the crack obstructs the wave's propagation in the medium. The results are identical to the Delta method showing that the simulation of the wave is undoubted. Furthermore, it can be adequately explained that the velocity of the Rayleigh wave was impeded by the surface crack, which can be employed in the crack mapping application.
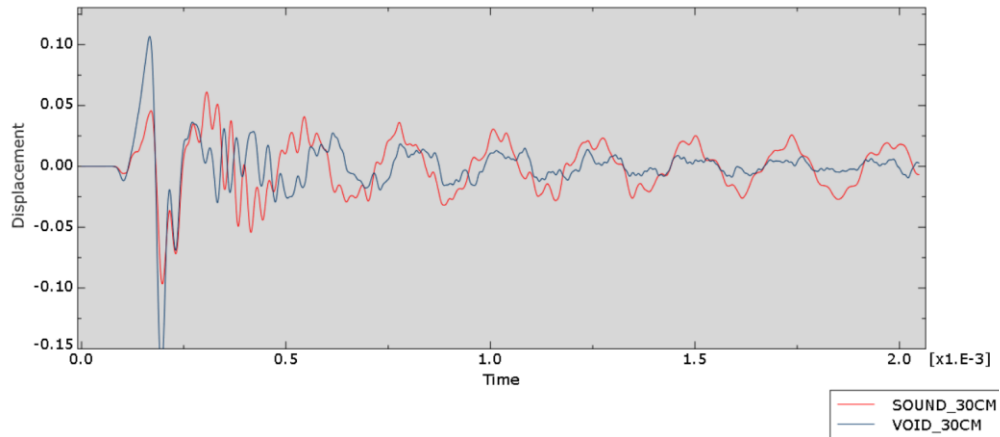
Figure 4.12: Time-Displacement Graph (Comparing Sound Specimen and 12.5 cm void specimen).

However, a specific event occurred in the time-displacement graph comparing intact and 12.5 cm void specimens, as shown in Figure 4.12. The time taken for a wave propagating through two sensors were 29 ms and 30 ms. The data confirm that the arrival time for both cases is nearly identical, showing the pathway of the Rayleigh wave was not affected by the sub-surface defection. A plausible explanation is that the wavelength of the wave is not significant enough to detect the void at 12.5 cm. Therefore, the result shows the inadequacy of wave velocity to detect a sub-surface crack. It is essential to consider the pressure wave frequency, which consists of broader coverage and detection of sub-surface defection in the concrete medium. The data draw a distinction between the Delta method and ABAQUS on the capability of wave velocity in detecting surface and embedded flaws in the structure.
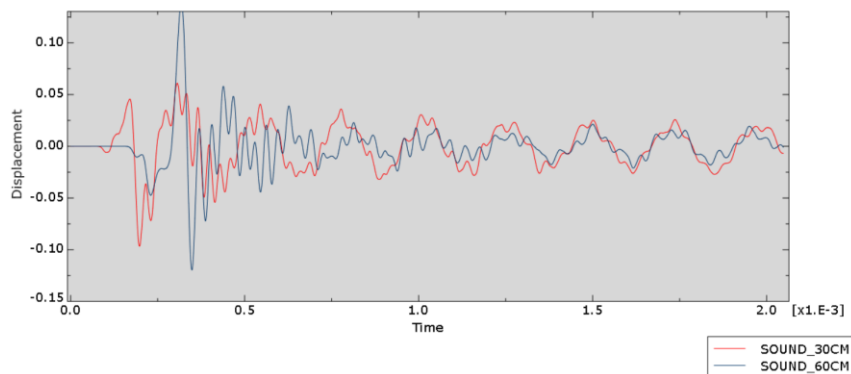
Figure 4.13: Time-Displacement Graph (Undamaged Specimen).
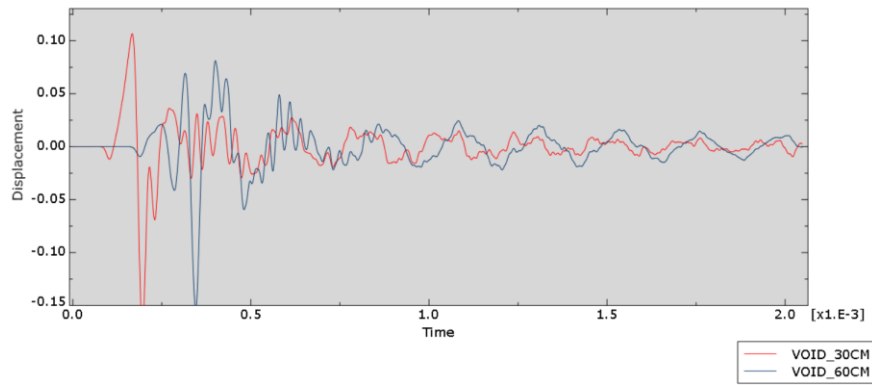
Figure 4.14: Time–Displacement Graph (12.5 cm Void Specimen).
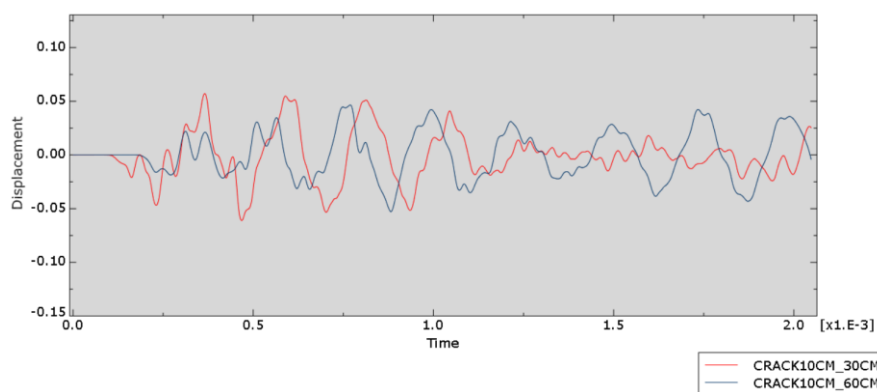
Figure 4.15: Time–Displacement Graph (10 cm Crack Specimen).
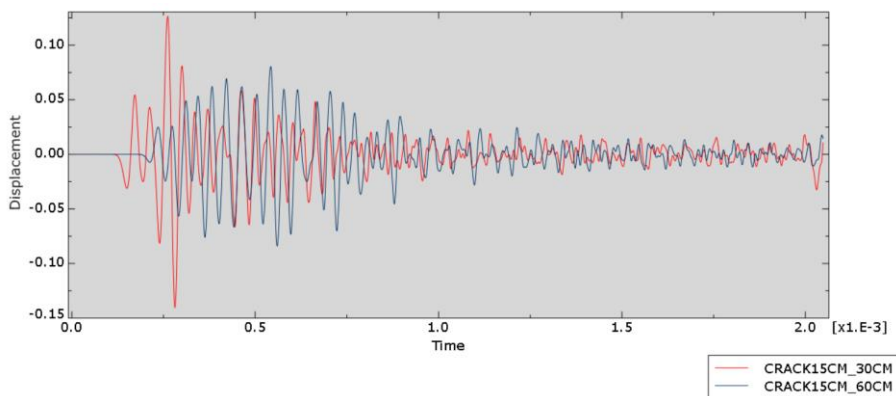
Figure 4.16: Time–Displacement Graph (15 cm Crack Specimen).

Figure 4.13 to Figure 4.16 show that the time–displacement graphs comparing the different distances of the set of oscillator and sensor. The time taken for a wave propagating through the 30 cm sensors set was longer than the 60 cm sensors set for all models. It provides clear evidence that the velocity is constant throughout the medium. It is similar to the Delta method, where the

time delayed by crack is significant and can be employed in crack imaging models.

4.4.2 Frequency Domain

The identification of flaw in concrete using P-wave relies on the frequency. As the P-wave contacted the defect boundary, it reflected and discretized the frequency of the wave. Appendix B presents the Fast Fourier Transform (FFT) graph of different types of crack. Figure 4.17 to Figure 4.24 highlighted the mode frequencies from the frequency domain graph obtaining from FFT plugins in ABAQUS.
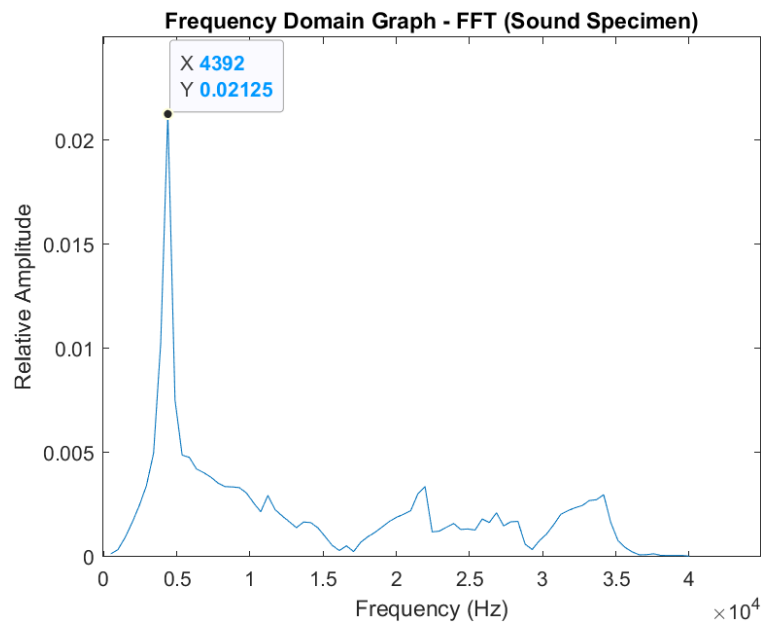
Figure 4.17: Frequency Domain Graph for Intact Specimen.

There are two cases for calculating the relative frequency: (a) Concrete Boundary and (b) Steel Boundary. Due to the uncertainty on the ABAQUS simulation's boundary condition, a reserve calculation was computed using an undamaged specimen, which acts as an experiment control. In Figure 4.17, the first mode frequency with 4392 Hz was found. As in result, the boundary condition for this simulation was likely to steel boundary, and the formula for depth estimation was expressed in Equation 4.1 (Tokai and Ohtsu, n.d.).

$$f_{crack} = \frac{velocity\ of\ P - wave}{4 \times depth} \qquad (4.1)$$
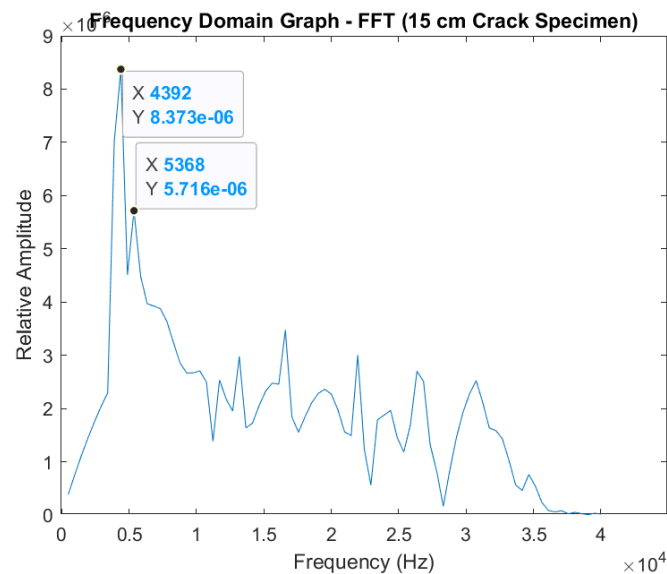
Figure 4.18: Frequency Domain Graph for 15 cm Crack Specimen.

Figure 4.18 presents the frequency domain graph for the 15 cm Crack specimen. Two-mode frequencies were falling within the range of 10 kHz, which were 4392 Hz and 5368 Hz. As an analogy, the first mode frequencies indicate P-wave reflection at the boundary of the specimen. The detection of crack at 15 cm is noticed at second mode frequencies. The mode frequencies larger than 10 kHz specifies the discrepancy of signal due to the deflection of wave in the simulation.
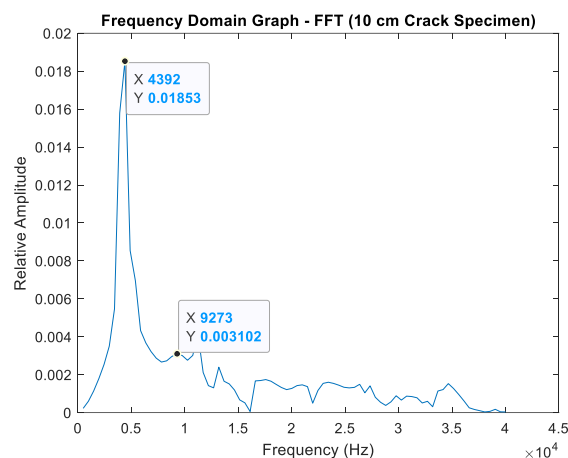
Figure 4.19: Frequency Domain Graph for 10 cm Crack Specimen.

From Figure 4.19, the mode frequencies within the 10 kHz were obtained at 4393 Hz and 9273 Hz. The first mode frequency indicates the depth of boundary, where the second mode frequency indicates the depth of the crack tip. Both mode frequencies agree well with the actual crack location in the specimen and are discussed in the summary of the result.
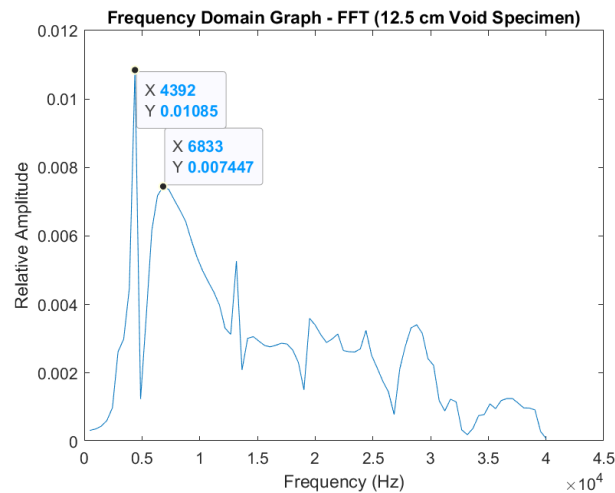
Figure 4.20: Frequency Domain Graph for 12.5 cm Void Specimen.

As discussed above, the arrival of the wave propagating in the 12.5 cm void specimen was equivalent to the arrival time in sound concrete due to the R-wave futility. However, in Figure 4.20, the P-wave frequency showed a piece of evidence where the wave reflected the wave and obtained the crack depth. The mode frequencies were found at 4392 Hz and 6833 Hz, representing the boundary and crack tip position.
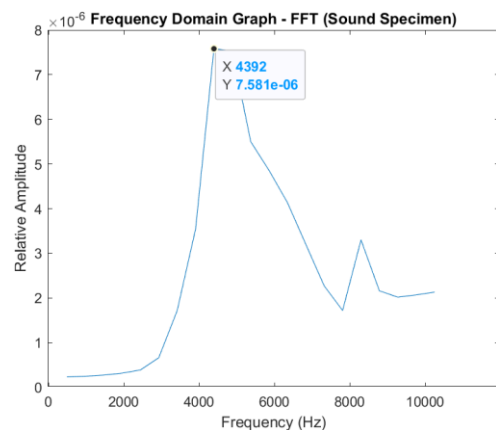
Figure 4.21: Frequency Domain Graph for Sound Specimen (Stochastic).

The stochastic model was generated in ABAQUS to simulate the virtual situation of the concrete specimen with heterogeneous properties. The average velocity of concrete was obtained with 3687.462 m/s. The discrepancy of the result was larger compared to the deterministic model. However, it still successfully presents the location of the crack with the least amount of error. The mode frequency attained from the reflection of the wave at the specimen boundary was found at 4393 Hz within the 10 kHz, as illustrated in Figure 4.21. Therefore, the thickness of the specimen was substantiated using the relative frequency computation.
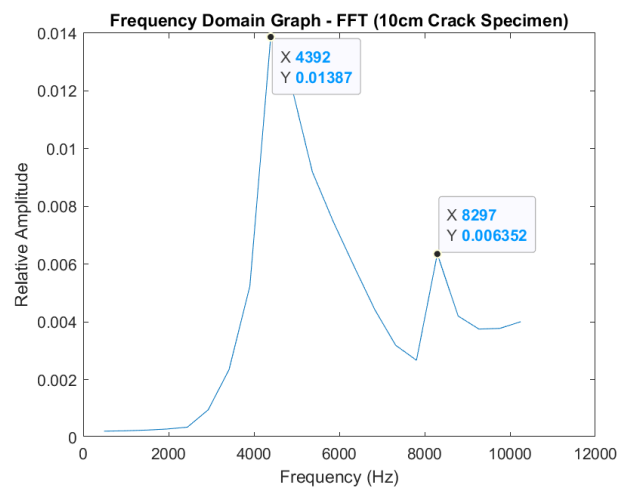
Figure 4.22: Frequency Domain Graph for 10 cm Crack Specimen
(Stochastic).
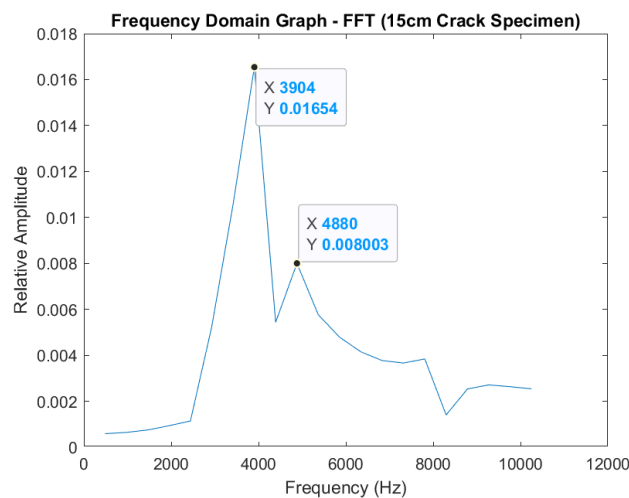
Figure 4.23: Frequency Domain Graph for 15 cm Crack Specimen
(Stochastic).

In Figure 4.22, two-mode frequencies within 10 kHz were acquired at 4392 Hz and 8297 Hz, representing the location of specimen boundary and crack tip. In Figure 4.23, the mode frequencies were attained at 3904 Hz and 4880 Hz.
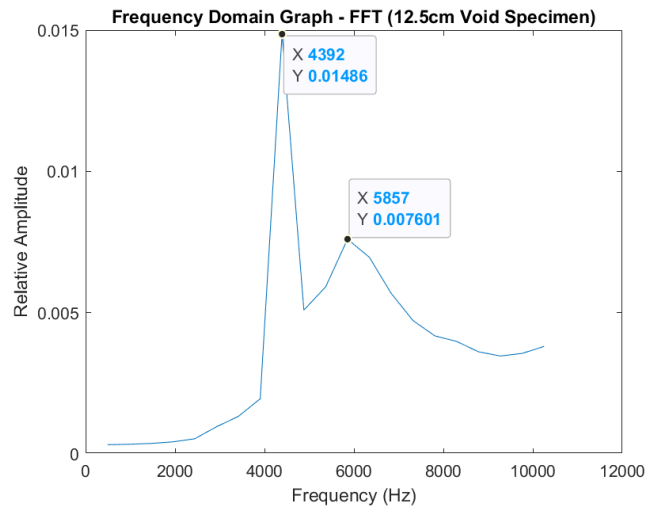
Figure 4.24: Frequency Domain Graph for 12.5 cm Void Specimen (Stochastic).

Finally, Figure 4.24 illustrated the frequency domain graph for 12.5 cm Void Specimen. The mode frequencies within 10 kHz were 4392 Hz and 5857 Hz.

In a nutshell, the detection of crack depth using reflection of P-wave was summarised and tabulated in Table 4.3 to further pursue the accuracy of crack detection. The thickness of the specimen was recognized in almost every model with a percentage error below 5 per cent. Nevertheless, a considerable discrepancy was attained in the stochastic 12.5 cm void model with a percentage error of 15.3%. An apparent advantage was noticed in the deterministic model for the finding of crack tip in each model. Each model's percentage error in the deterministic model was lower than the corresponding model in the stochastic model. A conclusion has been made from the result where the stochastic model consists of uncertainties caused by discrete field of aggregate, pore and cement grain. The wave might deflect the wave propagation and caused minor incongruity in the result. Regardless of the ambiguity caused by other concrete

Table 4.3: Summary of Result from ABAQUS simulation.

Specimen	Actual Depth (mm)	$f_1(Hz)$	Relative Depth (mm)	Percentage Error (%)	$f_2(Hz)$	Relative Depth (mm)	Percentage Error (%)
Deterministic Model							
Sound	200 (Boundary)	4392	206.43	3.12	-	-	-
10 cm Crack	100 (Crack)	4392	206.43	3.12	9273	97.77	2.28
12.5 cm Void	125 (Void)	4392	206.43	3.12	6833	132.69	5.78
15 cm Crack	150 (Crack)	4392	206.43	3.12	5368	168.90	11.19
Stochastic Model							
Sound	200 (Boundary)	4392	209.90	4.72	-	-	-
10 cm Crack	100 (Crack)	4392	209.90	4.72	8297	110.42	9.44
12.5 cm Void	125 (Void)	3904	236.13	15.30	5857	156.42	20.09
15 cm Crack	150 (Crack)	4392	209.90	4.72	4880	187.74	20.10

factors, both models worked well in detecting the internal flaw of the specimen with 20% disagreement. The results are discussed in Table 4.3 by comparing the predicted depth with the theoretical assumptions.

4.5   Crack Imaging

Crack imaging is rarely employed in the engineering field due to the inconsistency of wave propagation in the concrete specimen. In this paper, a noble crack mapping model was developed. The model was investigated among deterministic specimens and stochastic specimens to identify the practicality of the model for construction purposes. This model covers a three-dimensional approach that allows users to identify crack and crack tip location through surface and cross-section plots, respectively. A few advantages were pointed out in this discussion to compare with the models proposed by other researchers.

4.5.1   Surface Crack Imaging

Figure 4.25 to Figure 4.30 illustrate the surface tomography of different crack attained from the ellipse-based spatial interpolation. The results were compared among two distinct sensor's configurations for deterministic and stochastic models.

(a)   (b)
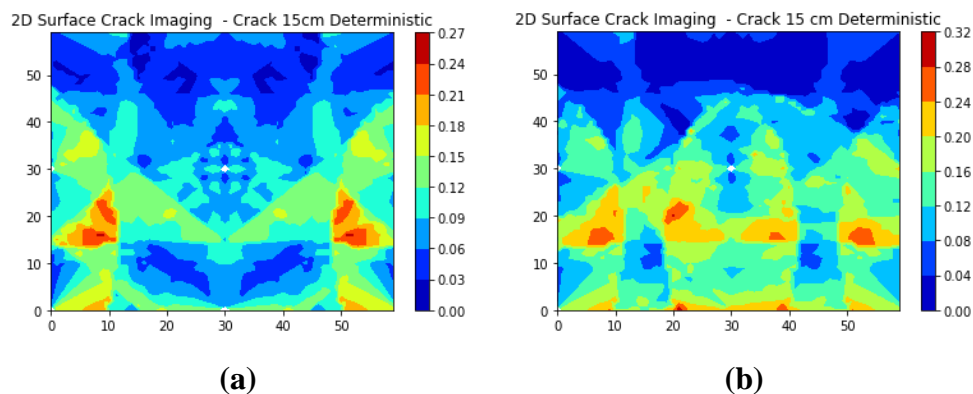
Figure 4.25 Surface Crack Imaging for 15 cm Crack Deterministic Model: (a) 8 Sensors Configuration and (b) 9 Sensors Configuration.

(a) (b)
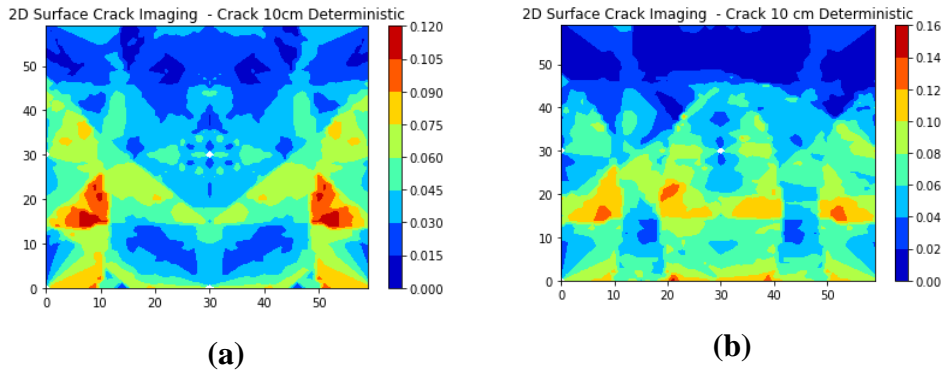
Figure 4.26: Surface Crack Imaging for 10 cm Crack Deterministic Model: (a)
8 Sensors Configuration and (b) 9 Sensors Configuration.

(a) (b)
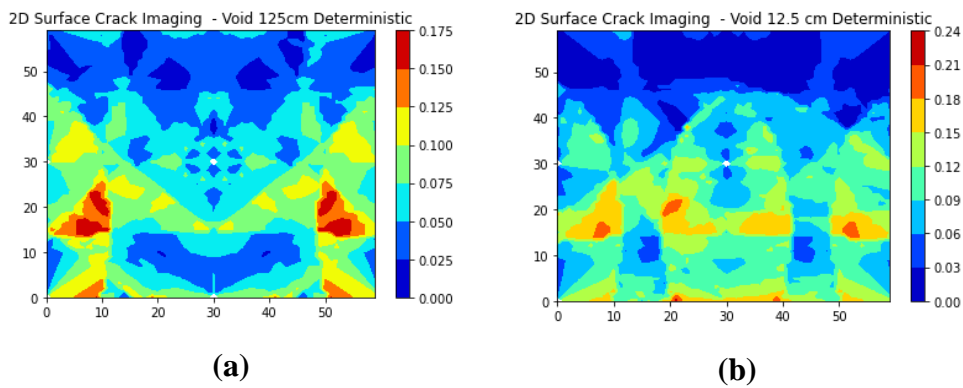
Figure 4.27: Surface Crack Imaging for 12.5 cm Void Deterministic Model:
(a) 8 Sensors Configuration and (b) 9 Sensors Configuration.

(a) (b)
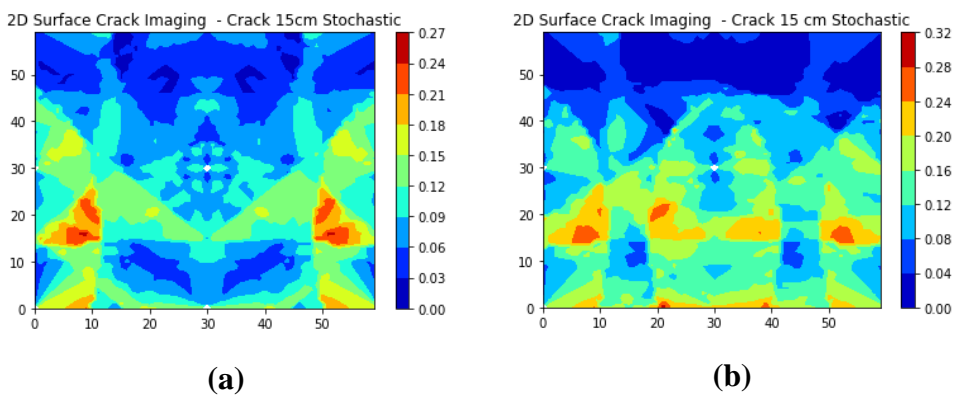
Figure 4.28 Surface Crack Imaging for 15 cm Crack Stochastic Model: (a) 8
Sensors Configuration and (b) 9 Sensors Configuration.
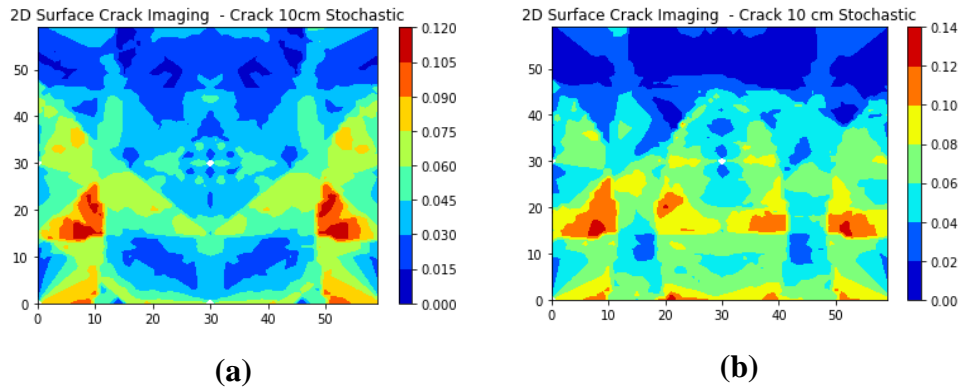
Figure 4.29: Surface Crack Imaging for 10 cm Crack Stochastic Model: (a) 8 Sensors Configuration and (b) 9 Sensors Configuration.
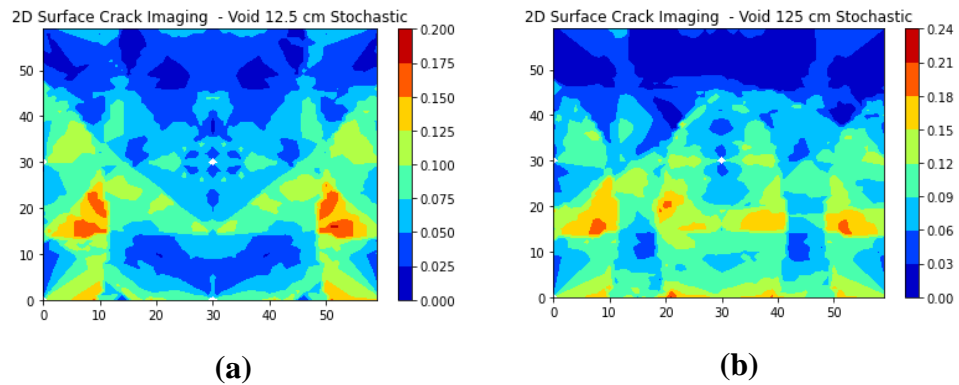
Figure 4.30:Surface Crack Imaging for 12.5 cm Void Stochastic Model: (a) Sensors Configuration and (b) 9 Sensors Configuration.

The surface cracks imaging model employed and modified the ellipse-based spatial interpolation method to estimate crack location. Rayleigh wave was used to detect the surface crack. Hence, the results from the Delta method are contributed to this model to identify the velocity of each grid cell. From the researcher's paper, the velocity in a medium varies with depth due to the deflection of wave beam by the crack tip (Lee, et al., 2016). Therefore, the variance of velocity was computed to evaluate the condition of the concrete. Due to the application of the spatial interpolation method, the deflected light beam was intersected into a healthy zone. Therefore, a slight amount of variance was observed at the unaffected zone. As a result, the crack location was assessed when the most significant variances were found among the surface plots.

Figure 4.31 illustrates the configuration of the specimen for simulation and crack detection. The artificial horizontal crack was created along Y = 50 cm

with 1 cm crack width. Figure 4.25 to Figure 4.30 have shown the result of surface crack detection in terms of the variance of experimental velocity and theoretical velocity. The variance indicated the presence of crack at the respective grid cell. For the 15 cm crack specimen, the maximum variance coefficient ranged from 0.27 to 0.32 for both stochastic and deterministic model. The maximum variance coefficient was attained between 0.2 and 0.24 for stochastic and deterministic 12.5 cm crack specimen. Lastly, the maximum variance for 10 cm crack specimen, the maximum variance coefficient gave the range of 0.12 to 0.16 for both models. The result shows an increasing fashion of variance with depth.

(a) (b)
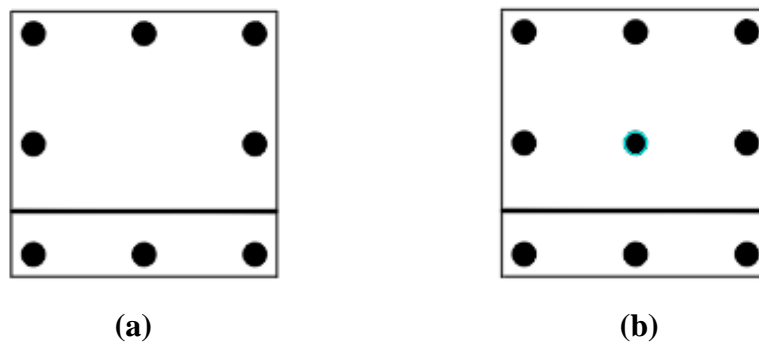
Figure 4.31: Specimen Configuration for (a) 8 Sensors and (b) 9 Sensors.

The surface crack detection model worked well to identify the location of the crack. It is undemanding that the highest variance coefficient occurred when Y felt between 145 and 155 cm. The minor incongruities might be caused by the interference of wave during the analysis stage. The discrepancy of result is also detected at the specimen's boundary as the wave is reflected and result in a noticeable difference between theoretical and experimental wave velocities. Although some discrepancies were attained from the models, the high colour zone shows an extensive line that establishes the locale of concrete defects.

The proposed algorithm utilized the variance coefficient, which considered both experimental and theoretical velocities. Researchers had projected various crack detecting models by identifying the low-velocity zone in the specimen. The accuracy of the approach could be disturbed by the heterogeneity of concrete considering the discrete distribution of aggregate and void. Therefore, the stochastic model was proposed by estimating the random

distribution of engineering properties and evaluating the variance coefficient to identify crack location. Hence, the results from both stochastic and deterministic model in this paper were in proximity to each other.

Initially, an eight sensors configuration was proposed to build the crack model by studying the reference from the crack imaging method by Du (2015). However, there were some shortcomings discovered along with the development of the algorithm. The suggested configuration was initially employed to detect the defection in wood that had a circular shape. The concrete specimens or elements tend to be quadrilateral, and there were some "grey areas" that failed to predict the velocity of specific grids precisely. Every velocity ray intersected at the centre of the specimen and caused a minor error in the model. Therefore, an additional sensor was used to improve the precision of the result, and the respective nine sensor configuration's model showed a clearer image of the crack line.

4.5.2 Beta (β) value

Figure 4.32 to Figure 4.34 illustrate the beta value of various crack specimens at the cross-section. In this paper, an integrated crack formulation was developed to identify the precise location of defection in the concrete structure. Time or velocity of Rayleigh wave was attained to identify the defection at the surface, and the frequency of the Pressure wave was used to determine the depth of defection. A noble coefficient was introduced, known as the beta (β) value.

(a)   (b)
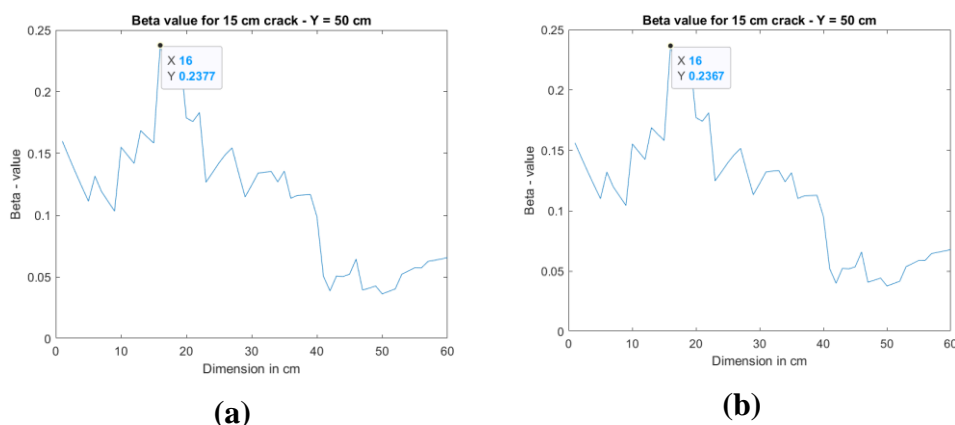
Figure 4.32: β–Value for 15 cm crack specimen at cross section (Y = 50 cm): (a) Deterministic model and (b) Stochastic Model.
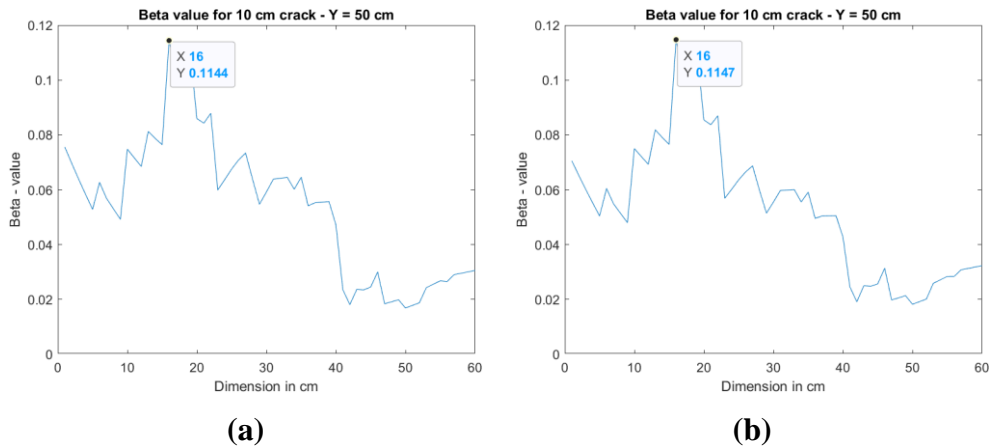
Figure 4.33: β–Value for 10 cm crack specimen at cross section (Y = 50 cm):
(a) Deterministic model and (b) Stochastic Model.
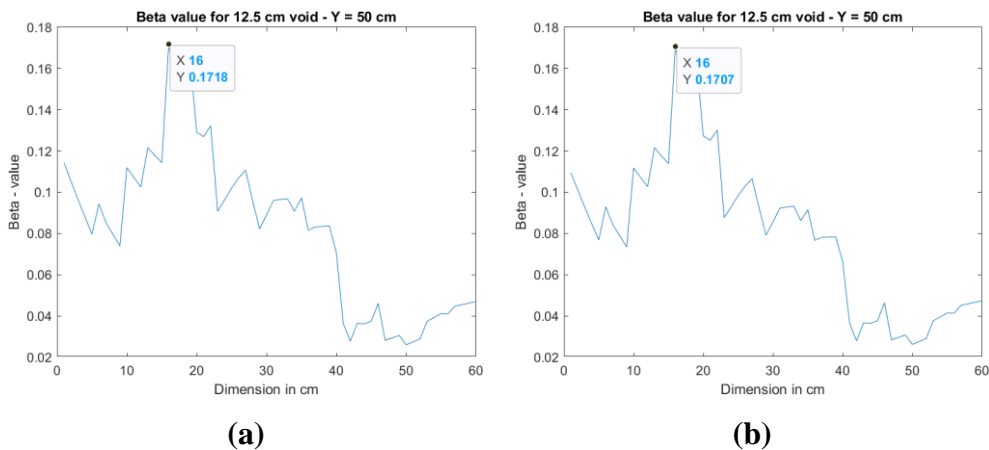
Figure 4.34: β–Value for 12.5 cm void specimen at cross section (Y = 50 cm):
(a) Deterministic model and (b) Stochastic Model.

The beta value is a coefficient representing the variance of the velocity of each grid cell, allowing the connection between both discrete computations. The obtained beta value was stored in a (60 by 60) matrix for each specimen. A cross-section is studied by extracting a row of beta values to proceed with the graphical analysis for discussion.

Instead of having the maximum value at 15 cm, the graph showed the highest value at 16 cm. The graphical presentation in MATLAB software causes a minor difference. The extracted beta value was stored in the (1 by 60) matrix where the first value initiated at X = 1 cm, as shown in Figure 4.35 below. Hence, the location of the crack is derived into $(x - 1)$ cm.

Figure 4.32 to Figure 4.34 illustrate the beta value for concrete specimen at the cross-section. The trend line of the graph began at 0.15 and declined slowly when X = 10 cm. The trend line rocket significantly and reached the highest point when X = 16 cm. Afterwards, the trend line went down moderately. Since the beta value denoted the velocities variance for each grid cell, the highest value defined crack location was stated at the location (x = 15 cm). The location of the crack is detected correctly without discrepancy. At the intact zone of the specimen where X = 31 cm to X = 60 cm, the beta value trend fell below the average line and indicated no defection within the area.
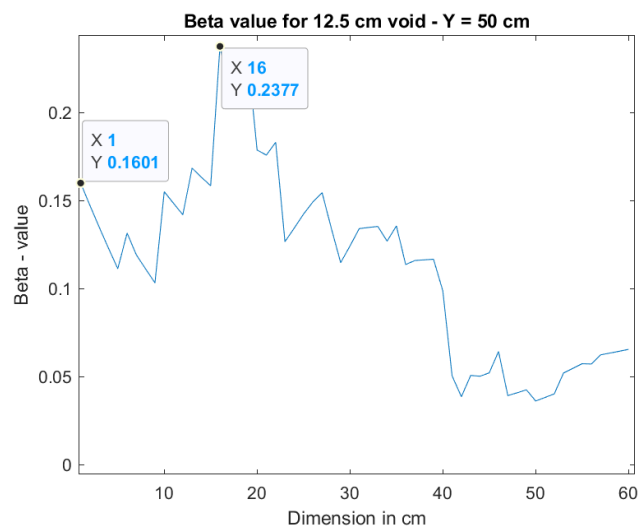
Figure 4.35: Minor Dimension Error on MATLAB Graphical Presentation.

4.5.3 Cross-Section Crack Imaging

A three-dimensional crack imaging model was built by integrating the surface crack imaging method and beta reflection method. Figure 4.36 (a) to Figure 4.41 (a) illustrates the 3D model that allows users to determine the concrete structure's defection. The cross-section is extracted for each model to identify the crack location, as shown in Figure 4.36 (b) to Figure 4.41 (b).

(a)   **(b)**
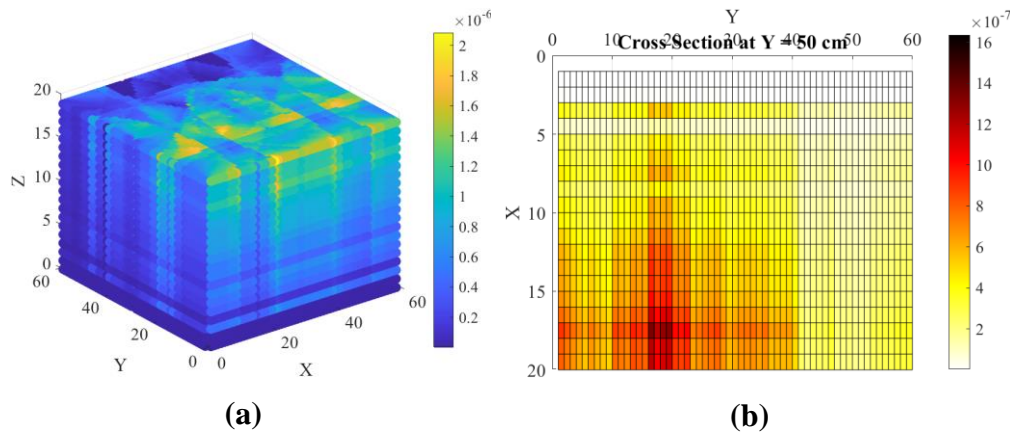
Figure 4.36: Crack Imaging for 15 cm Crack Deterministic Model: (a) Three-Dimensional Model and (b) Cross-Section Model at Y = 50 cm.

(a)   **(b)**
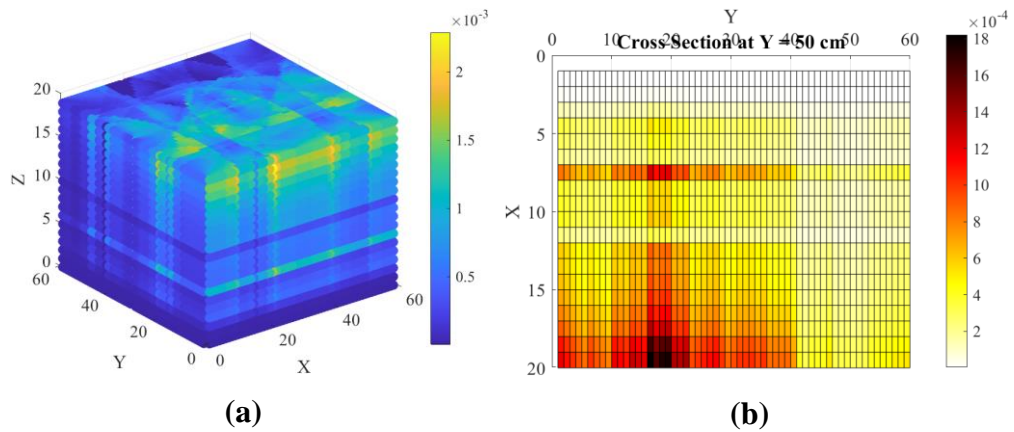
Figure 4.37: Crack Imaging for 15 cm Crack Stochastic Model: (a) Three-Dimensional Model and (b) Cross-Section Model at Y = 50 cm.

(a)   **(b)**
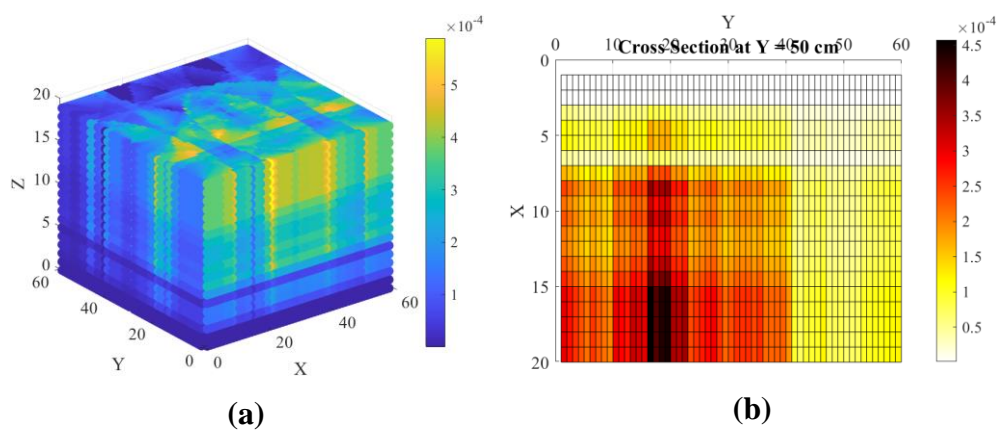
Figure 4.38: Crack Imaging for 10 cm Crack Deterministic Model: (a) Three-Dimensional Model and (b) Cross-Section Model at Y = 50 cm.

(a)   **(b)**
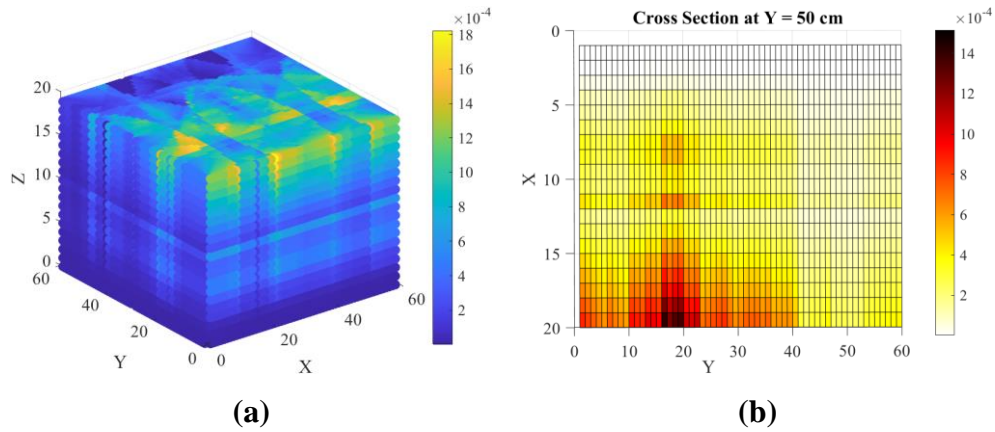
Figure 4.39: Crack Imaging for 10 cm Crack Stochastic Model: (a) Three-Dimensional Model and (b) Cross-Section Model at Y = 50 cm.

(a)   **(b)**
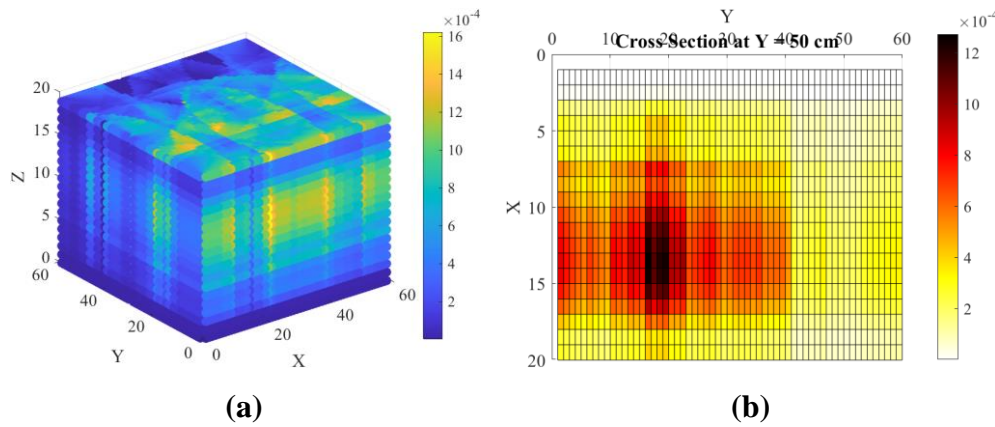
Figure 4.40: Crack Imaging for 12.5 cm Void Deterministic Model: (a) Three-Dimensional Model and (b) Cross- Section Model at Y = 50 cm.

(a)   **(b)**
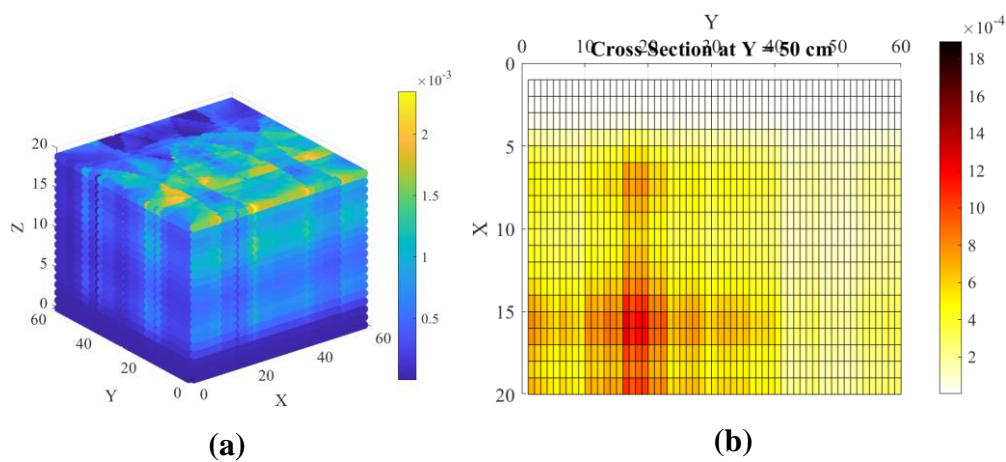
Figure 4.41: Crack Imaging for 12.5 cm Void Stochastic Model: (a) Three-Dimensional Model and (b) Cross-Section Model at Y = 50 cm.

The result from Fast Fourier Transform was multiplied by the beta value of each grid cell to study the crack depth at the cross-section. Figure 4.36 (b) to Figure 4.41 (b) demonstrate the colour map for each cross-section, indicating the crack propagation in the damaged specimen. The descriptions of each cross-section results were discussed in Table 4.4.

Table 4.4: Discussion of Results.

Model	Description
15 cm Crack Deterministic	The maximum value was discovered at grid [16, 17] which indicated the crack tip. The numeric result of the crack depth was 168.90 mm, which resulted in an 11.19 per cent error.
15 cm Crack Stochastic	The maximum value was found at grid [16,19] which indicated the crack tip. The numerical result of the crack depth was 187.74 mm, which led to a 20.10 per cent error.
10 cm Crack Deterministic	The maximum values were discovered at two locations: grid [16, 10], grid [16, 15-20] which indicated the crack tip and the boundary, respectively. The numerical result of the crack depth was 97.77, which resulted in a 2.28 per cent error.
10 cm Crack Stochastic	The maximum values were discovered at two locations: grid [16,11] and [16,20], indicating the crack tip and the boundary, respectively. The numerical result of crack depth was 110.42, which resulted in a 9.44 per cent error.
12.5 cm Crack Deterministic	The maximum value was found at grid [16, 13] which showed the void's location within the damaged specimen. The numerical result of void location was 132.69 mm, which led to a 5.78 per cent error.
12.5 cm Crack Stochastic	The maximum value was found at grid [16,16]. The numerical result of void location was 156.42, which led to a 20.09 per cent error.

According to the results, the percentage errors in the deterministic model were slightly smaller compared to the stochastic model. Despite the minor difference in the result, the models had done a great job identifying the location of crack associating with the estimation of crack depth. The high discrepancy in the stochastic model was caused by the random distribution of engineering properties in the specimen. The random distribution was employed to simulate the potential wave interfering materials such as distribution of aggregate, void and cement paste in the actual concrete specimen, which affects the accuracy of the crack imaging method. However, the stochastic model presented an excellent performance in assessing concrete condition by presenting the crack location and depth with low percentage errors.

4.6   Comparison to Preceding Model

This newly developed algorithm provides a vantage point where the limitation of configuration is removed. Most of the preceding crack mapping models consist of restriction where the crack sits at the centre of the oscillator and receiver. Though, this model can assess the concrete specimen under non-uniform crack condition. The position of the crack is not necessary to be present symmetrically between the oscillator and receiver. A slanted 15 cm crack line was proposed on the specimen's surface and assessed using the crack imaging model, as shown in Figure 4.42. The result agrees well with the theoretical assumption and clearly defines the predicted crack lines.
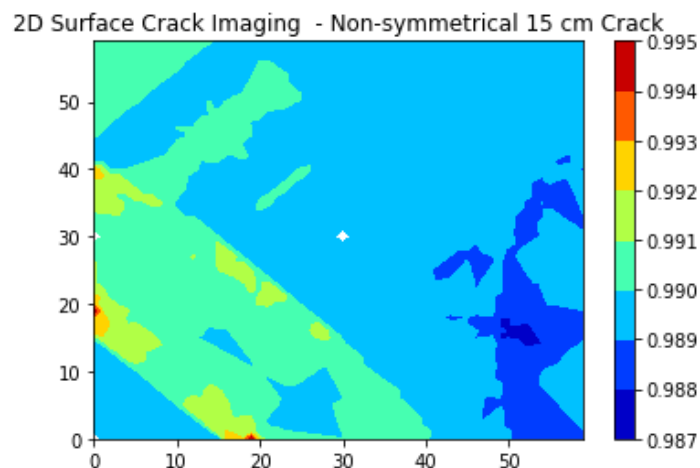
Figure 4.42: Non-Symmetrical Crack Line.

Furthermore, the beta reflection method improves the accuracy of the crack detecting approach comparing to the scanning SIBIE method. Both methods were contrasted in terms of the capability of estimating and visualized crack tips. With the same amount of testing required, a well-defined crack tip was observed in the conceptual formulation without any false result due to the symmetrical disturbance of one-point detection.

However, in the actual situation of defected concrete, a crack occurs with non-uniform depth, which turns the detecting work challenging. Therefore, the beta reflection method was tested against an inclining crack of 5 cm to 15 cm. The result is illustrated in Figure 4.43. A clear-cut crack region was observed. The crack region showed a higher variance at the left side of the specimen and decreasing along the crack line. Therefore, the proposed formulation could be used to detect concrete flaws with indiscriminate crack depth.
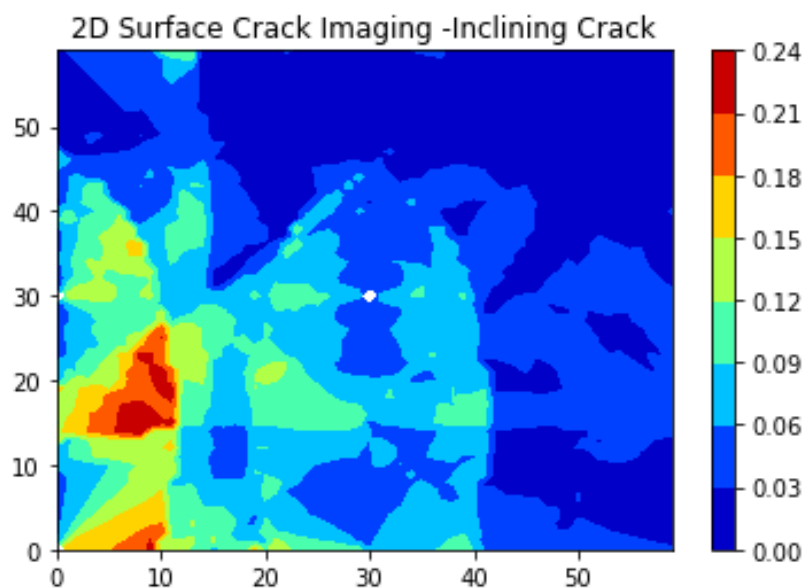
Figure 4.43: Crack Detection on Non-uniform Depth

The researchers proposed various existing crack detection techniques such as B- scan and C-scan techniques and the SIBIE method. In this paper, the author's novel crack mapping was contrasted with the existing technique and discussed in terms of the amount of test needed and their accuracy.

B-scan and C-scan methods provide a satisfactory result on detecting the crack on the surface and at the cross-section of the concrete specimen. However, the number of tests needed is enormous compared to the beta reflection method. The beta reflection method requires only nine iterations of the impact echo test. Despite the slight amount of tests needed associating with the former proposed technique, the beta reflection method delivers a well-defined crack line with low percentage error. The proposed model is compared with different models in Table 4.5.

Table 4.5: Comparison Between Existing Models.

Models	Level of Interest	Number of Tests	Reference
Beta Reflection Method	Three-dimensional Model	9	-
Scanning SIBIE Method	Two-dimensional Cross Section	3	(Tokai, et al., 2009)
B–scan / C–scan	Three-dimensional model	One Iteration for each 1 cm by 1 cm grid	(Yeh and Liu, 2009)

In short, it is not easy to compare the tangible accuracy between these three models as the availability of a numerical model is absent. However, the results of the models are contrasted based on the result from the respective journal. SIBIE method has presented a percentage error of around 10 per cent, but there is much noise from the crack image. Without the given location of the crack, a false message would be given due to the symmetrical error from the one point detection.

Moreover, B-scan and C-scan method work well in giving nearly identical crack depth. Nevertheless, it requires a vast amount of tests for the input of data. The proposed model overcomes most weaknesses from the preceding model as the stochastic process helps to determine the uncertainty of random variables with a low amount of input data. The percentage error of this model achieves around 10 per cent for the deterministic model. On the other hand, this is the first study considering the random distribution of concrete

properties in the numerical simulation. Hence, the discrepancy of result might be low when verifying with the actual specimen in the laboratory test.

4.7 Summary

In a nutshell, a conceptual formulation for crack mapping prediction is presented using deterministic and stochastic modelling. A complete three-dimensional model was constructed integrating the surface crack model and the crack depth detection technique. The results agree well with the proposed configuration of the theoretical concrete slab. The accuracy of the model was enhanced compared to existing models by other researchers with a lesser number of elastic wave tests.

CHAPTER 5

CONCLUSIONS AND RECOMMENDATIONS

5.1 Conclusions

A feasible crack mapping prediction formulation for concrete monitoring using a stochastic model is constructed. Several conclusions have been made regarding the objectives of the study.

Firstly, the integrated crack mapping model correlating with the Impact-echo method provides a novel solution for crack mapping prediction using stochastic modelling. The time-domain graph and frequency-domain graph was obtained from the ABAQUS wave simulation. The surface velocity tomography was attained using the ellipse-based spatial interpolation method in Python. The beta value was acquired, and it precisely presented the crack's location at $X = 15$ cm. After that, the beta reflection method constructed a three-dimensional crack mapping prediction model in MATLAB. The projected crack depths were 97.77 mm, 132.69 mm, and 168.90 mm for the 100 mm crack model, 125 mm crack model and 150 mm crack model, respectively. The corresponding percentage errors for each model were 2.28 %, 5.78 % and 11.19 %. It provides conclusive evidence where the crack mapping model can evaluate the concrete condition with the slightest discrepancies.

This study is the first to consider the heterogeneity properties of concrete during the prediction of crack mapping. The lognormal random field distribution of Young's Modulus and Poisson ratio is constructed to predict the concrete's actual condition in the mesoscale level of interest. This finding is significant as it considers the effect of disturbance on wave propagation in the sample. Despite considering the external effect on wave disruption, the beta value from the surface wave tomography is like a deterministic model indicating the crack location at $X = 15$ cm. The predicted crack depths were 110.42, 156.42 and 187.74 for the 100 mm crack model, 125 mm crack model and 150 mm crack model. The corresponding percentage errors for each model were 9.44 %, 20.09 % and 20.10 %. The model is versatile to predict the crack mapping in concrete structures considering the random distribution of concrete properties.

This novel crack mapping model features have been extended to detect various types of crack, including surface crack, internal void, non-symmetrical crack, and non-uniform crack. It significantly improves the preceding models, restricting by enormous limitations on the apparatus's configuration. The effectiveness of techniques in terms of accuracy has enhanced significantly. With the minimum iteration of field test required (9 sensors), the crack mapping model presented a clearly defined crack image indicating the location of defection.

In short, this finding has presented an integrated crack mapping prediction model, which is crucially important for the development of non-destructive test in terms of reliability, accuracy, and effectiveness.

5.2   Recommendations for Future Work

In this study, the impact echo method was modelled using the Delta method and wave simulation in ABAQUS software. Due to the pandemic situation, laboratory work is unavailable. Hence, it is uncertain if the replication of numerical models provides the wave propagation properties in a concrete sample. The result attained from the laboratory test might present a slight disparity affected by external factors. Future studies should consider the verification of simulation result with a laboratory test to extend the reliability of the proposed crack predicting model to address this limitation.

Besides, the construction of an automated Impact-echo instrument is an interesting area for future studies. This device had been proposed by Hashimoto, et al. (2019), which included a set of sensors associated with a laser droplet vibrometer. It introduces an automated procedure of hammering and receiving laser-doppler vibrometer processes, allowing remote-controlled non-destructive testing. Future research should attempt to modify and adapt the novel device with the integrated crack mapping model to improve the efficiency and performance of the non-destructive test.

Being an exploratory study of a stochastic crack mapping prediction model, this work employed four types of software, including Python, MATLAB, Microsoft Excel, and ABAQUS. Each type of software expresses its unique function, which facilitates the construction of a novel numerical model.

However, further study should consider assimilating the numerical models in particular software to establish a widely used technique in the construction field.

REFERENCES

Algernon, D. and Wiggenhauser, H., 2007. Impact echo data analysis based on Hilbert-Huang Transform. *Transportation Research Record: Journal of the Transportation Research Board,* [e-journal] 2028(2028), pp. 146-153. http://doi.org/10.3141/2028-16

Ari, W. et al., 2014. Crack depth measurement of reinforced concrete beams using UPV. *Jurnal Rekayasa Sipil,* 8(1), pp. 41-46.

ASTM C1383-15, 2015. *Standard Test Method for Measuring the P-Wave Speed and the Thickness of Concrete Plates Using the Impact-Echo Method.* West Conshohocken: ASTM International.

Base Concrete, n.d. *Different types of concrete grades and their uses.* [Online] Available at: <https://www.baseconcrete.co.uk/different-types-of-concrete-grades-and-their-uses/> [Assessed 11 September 2020]

Beal, D., n.d. Types and Causes of Cracks and Cracking. *Queensland University of Technologi,* pp. 1-6.

Bouden, T., Djerfi, F., Dib, S. and Nibouche, M., 2012. Hilbert Huang Transform for enhancing the impact-echo method of nondestructive testing. *J. Autom. Syst. Eng*, 6(4), pp.172-184.

Building and Constuction Authority, 2012. *A Guide on Concrete Usage Index.* Singapore: The Centre for Sustainable Buildings and Construction.

Carino, N., 2001. Impact echo: the fundamental. *International Symposium Non-Destructive Testing in Civil Engineering,* pp. 1-18.

Cement Concrete and Aggregates Australia, 2005. *Plastic Settlement Cracking.* [Online] Available at: <https://www.ccaa.com.au/imis_prod/documents/Library%20Documents/CCAA%20Datasheets/DS2005Settlement.pdf> [Accessed 13 August 2020].

Chai, H.K., Liu, K.F., Behnia, A., Yoshikazu, K. and Shiotani, T. 2016. Development of a tomography technique for assessment of the material condition of concrete using optimized elastic wave parameters. *Material (Basel)*, [e-journal] 9(4), pp. 291. http://doi.org/10.3390/ma9040291

Chin, W.Z., 2019. *Forecasting of Concrete Strength During the Hardening Process by Means of Elastic Wave Method.* Final Year Project, Universiti Tunku Abdul Rahman.

Chou, H.-C., 2019. Concrete object anomaly detection using a nondestructive automatic oscillating impact-echo device. *Applied Science 9*, 11 January, [e-journal] 9(5), p. 904. http://doi.org/10.3390/app9050904.

Constantine, P., 2012. *Random Field Distribution.* [Online] Available at: <https://www.mathworks.com/matlabcentral/fileexchange/27613-random-field-simulation> [Accessed 3 September 2020].

Cyber Logic, Inc, 2015. *Wave2000.* [Online] Available at: <https://www.cyberlogic.org/wave2000.html> [Accessed 3 September 2020].

Department of Standard Malaysia, 2010. *Eurocode 2: Design of Concrete Structure- Part 1-1: General Rules and Rules for Building.* MS EN 1992-1-1: 2010 ed. Selangor: Standards Malaysia.

Dutt, A., 2015. Effect of mesh size on finite element analysis of beam. *SSRG International Journal of Mechanical Engineering (SSRG-IJME)*, [e-jounal] 2(12), pp. 8-10. http://doi.org/10.14445/23488360/IJME-V2I12P102.

Du, X. C. et al., 2015. Stress wave tomography of wood internal defects using ellipse-based spatial interpolation and velocity compensation. *Bioresources,* [e-jounal] 10(3), pp. 3948-3962. http://doi.org/10.15376/biores.10.3.3948-3962.

Eliáš, J., Vorechovsky, M., Skocek, J. and P.Bazant, Z., 2015. Stochastic discrete meso-scale simulations of concrete fracture: Comparison to experimental data. *Engineering Fracture Mechanics ,* [e-jounal] Volume 135, pp. 1-16. https://doi.org/10.1016/j.engfracmech.2015.01.004.

Fan, Q., Gao, Q., Huang, Z. and Ji, L., 2012. *Crack detection in an infinite beam based on the amplitudes of the wave reflection coefficients.* In: PROCEEDINGS OF ISMA2012-USD2012, 2012 Leuven Conference on Noise and Vibration Engineering. Leuven, Belgium. September 2012. Leuven, Belgium.

Federal Highway Administration, 2005. *Chapter 7. Using The Hilbert-Huang Transform For Substructure Damage Evaluation.* [Online] Available at: <https://www.fhwa.dot.gov/publications/research/infrastructure/geotechnical/03089/chapt7.cfm> [Accessed 27 August 2020].

Feng, H., Li, G., Fu, S. and Wang, X., 2014. Tomographic image reconstruction using an interpolation method for tree decay location. *Bioresource,* [e-jounal] 9(2), pp. 3248-3263. http://doi.org/10.15376/biores.9.2.3248-3263.

FPrimeC, 2019. *How to Test Concrete Using Impact-Echo Method.* [Online] Available at: <https://www.fprimec.com/how-to-test-concrete-using-impact-echo-method/> [Accessed 1 September 2020].

Fujita, Y. and Hamamoto, Y., 2011. A robust automatic crack detection method from noisy concrete surfaces. *Machine Vision and Application,* 22(2), pp. 245-254.

Ganguli, A., Rappaport, C., Abramo, D. and Wadia-Fascetti, S., 2012. Synthetic aperture imaging for flaw detection in a concrete medium. *NDTandE International ,* [e-journal] Volume 45, pp. 79-90. http://doi.org/10.1007/s00138-009-0244-5

Giatec Scientific Inc, 2019. *Evaluating cracking in concrete: Procedure.* [Online] Available at: <https://www.giatecscientific.com/education/cracking-in-concrete-procedures/> [Accessed 13 August 2020].

Graham, D.L., Smith, S.D. and Dunlop, P., 2005. Lognormal distribution provides an optimum representation of the concrete delivery and placement process. *Journal of construction engineering and management*, *131*(2), pp.230-238.

Godfrey, E. and Henry, N. C., 2016. *Comparison of non-destructive and destructive examinations in today´s inspection practices.* In 19th World Conference on Non-Destructive Testing 2016. Delta State, Nigeria, 13-17 June 2016.

Hashimoto, K., Shiotani, T., Nishida, T. and Okude, N., 2019. Repair inspection technique based on elastic-wave tomography applied for deteriorated concrete structures. In: Gunay, Ezgi, eds. 2019. *Elasticity of Materials - Basic Principles and Design of Structures,*.

Hashimoto, K., Shiotani, T. and Ohtsu, M., 2020. Application of impact-echo method to 3D SIBIE procedure for damage detection in concrete. *Appl Sci,* 10(8), p. 2729.

Hlavac, Z., 2009. Detection of crack in a concrete element by impact-echo method. *Ultragaras "Ultrasound",* 64(2), pp. 12-16.

Hoang, N.-D., 2018. Detection of surface crack in buidling structure using image processing technique with an imporved otsu method for image thresholding. *Advances in Civil Engineering 2018.* [e-journal] https://doi.org/10.1155/2018/3924120.

HyperPhysics., n.d. *Seismic Wave* [Online] Available at: <http://hyperphysics.phy-astr.gsu.edu/hbase/Waves/seismic.html> [Assessed 11 September 2020]

Krüger, M. and Grosse, C.U., 2006, September. Crack depth determination using advanced impact-echo techniques. *In Proceedings of the 9th European Conference on Nondestructive Testing*, Berlin, Germany, pp. 25-29.

Kumar, S. A. and Santhanam, M., 2006. Detection of concrete damage using ultrasonic pulse velocity method. *Indian Society for Non-Destructive Testing Hyderabad Chapter.*

Lee, F., Chai, H. and Lim, K., 2016. Assessment of reinforced concrete surface breaking crack using rayleigh wave measurement. *Sensors,* 16(3), [e-jounal] p. 337. http://doi.org/10.3390/s16030337.

Lee, R., 2019. *ABAQUS for Engineers: A Practical Tutorial Book.* 1st ed. s.l.:BW Publishers.

Lee, Y. and Oh, T., 2016. The measurement of p-, s-, and r-wave velocities to evaluate the condition of reinforced and prestressed concrete slabs. *Advanced in Materials Science and Engineering,* [e-journal] p. 14. http://doi.org/10.1155/2016/1548215

Lim, Y., Kwong, K., Liew, W. and Soh, C., 2016. Non-destructive concrete strength evaluation using smart piezoelectric transducer - a comparative study. *Smart Materials and Structures,* 25(8), p. 085021.

Liu, P.-L. and Yeh, P.-L., 2012. Imaging methods of concrete structure based on impact-echo test. In: Omar, M, eds. *Nondestructive Testing Methods and New Applications,* p. 235.

Michael, D. M., 2006. Control of cracking in concrete: State of the art. In: *Transportation Research Circular.* Washington: Transportation Research Board, pp. 18-21.

Misra, S. and Li, H., 2019. Noninvasive fracture characterization based on the classification of sonic wave travel times. *Machine Learning for Subsurface Characterization,* pp. 243-285.

Most, T. and Bucher, C., 2006. Stochastic simulation of cracking in concrete structure using multiparameter random field. *International Journal of Reliability and Safety,* [e-journal] 1(1-2), pp. 168-187. https://doi.org/10.1016/C2018-0-01926-X

National Ready Mixed Concrete Association , n.d. *CIP 42 -Thermal Cracking of Concrete.* [Online] Available at: <https://www.crmca.com/wp-content/uploads/2016/08/CIP-42-Thermal-Cracking-of-Concrete.pdf> [Accessed 14 August 2020].

Nicholas, J., 2001. The impact-echo method: an overview 1. *InStructures 2001: A structural Engineering Odyssey,* [e-journal] pp. 1-18. http://doi.org/10.1061/40558(2001)15

Patrick, M. and Bridge, R.Q., 2002. Shear connection in composite beams incorporating profiled steel sheeting with narrow open or closed steel ribs. *In Advances in Steel Structures (ICASS'02)* pp. 511-518. Elsevier.

Pour-Ghaz, M., Barrett, T. and Ley, T., 2014. Wireless crack detection in concrete elements using conductive surface sensors and radio frequency identification technology. *Journal of Material in Civil Engineering,* 26(5), pp. 923-929.

Rabah, M., Elhattab, A. and Fayad, A., 2013. Automatic concrete cracks detection and mapping of terrestrial laser scan data. *NRIAG Journal of Astronomy and Geophysics,* [e-journal] 2(2), pp. 250-255. https://doi.org/10.1016/j.nrjag.2013.12.002.

Ryden, N., Park, C., Ulriksen, P. and Miller, R., 2004. Multimodal approach to seismic pavement testing. *Journal of Geotechnical and Geoenvironmental*

Engineering, [e-journal] 130(6), pp. 636-645. http://doi.org/10.1061/(ASCE)1090-0241(2004)130:6(636).

Sagar, R. V. and Prasad, B. R., 2009. Modelling heterogeneity of concrete using 2D lattice netwrok for concrete fracture and comparison with AE study. *Sadhana ,* [e-journal] 34(6), pp. 865-886. http://doi.org/10.1007/s12046-009-0052-7.

Seifi, R. and Mohammadi, R. M., 2018. Effects of tensile overload on crack initiation life and fatigue crack growth in notched specimens. *Transactions of the Indian Institude of Metals,* [e-journal] 71(9), pp. 2339-2348. http://doi.org/10.1007/s12666-018-1365-1.

Shah, J. K., Majhi, S. and Mukherjee, A., 2018. *Ultrasonic based crack imaging in concrete*. In: The 11th International Conference on Structural Integrity and Failure 2018. University of Western, Australia, 27 May 2018. London South Bank University

Shokouhi, P., Gucunski, N. and Maher, A., 2006. Time-frequency techniques for the impact echo data analysis and interpretations .*Aci Structural Journal,* 97(6), pp. 645-656.

Stawiski, B., 2012. The heterogeneity of mechanical properties of concrete in formed constructions horizontally. *Archives of Civil and Mechanical Engineering,* [e-journal] 12(1), pp. 90-94. http://doi.org/10.1016/j.acme.2012.03.006.

Sun, Y., Huang, P., Su, J. and Wang, T., 2018. Depth estimation of surface-opening crack in concrete beams using impact-echo and non-contact video-based methods. *EURASIP Journal on Image and Video Processing,* [e-journal] Volume 1, p. 144. http://doi.org/10.1186/s13640-018-0382-7.

Tasek Corporation Berhad, n.d. *Manufacture of Ordinary Portland Cement.* [Online] Available at: <http://www.tasekcement.com/index/cement_facts/manufacture_of_ordinary_portland_cement.html> [Assessed 10 August 2020]

The Engineering Toolbox, 2008. *Properties of normal strength Portland cement concrete.* [Online] Available at: < https://www.engineeringtoolbox.com/concrete-properties-d_1223.html>

Tokai, M., Ohkubo, T. and Ohtsu, M., 2009. Estimation of surface-crack depth in concrete by scanning SIBIE procedure. *Non-Destructive Testing in Civil Engineering,* [e-journal] 2(6), pp. 730-738, http://doi.org/10.1299/jmmp.2.730.

Tokai, M. and Ohtsu, M., n.d. Evaluation of the surface crack depth in concrete by Impact-Echo procedures (SIBIE). *Dimensions 400,* p. 250.

Torrent, R.J., 1978. The log-normal distribution: A better fitness for the results of mechanical testing of materials. *Matériaux et Construction*, *11*(4), [e-journal] pp.235-24. https://doi.org/10.1007/BF02551768

Wei, J., Di, B. R. and Ding, P. B., 2013. Effect of crack aperture on p-wave velocity and dispersion. *Applied Geophysics,* [e-journal] 10(2) , pp. 125-133. http://doi.org/10.1007/s11770-013-0379-z.

Wu, Z., Rong, H., Zheng, J. and Dong, W., 2013. Numerical method for Mixed-Mode i-ii crack propagation in concrete. *Journal of Engineering Mechanics ,* [e-jorunal] 139(11), pp. 1530-1538. http://doi.org/10.1061/(ASCE)EM.1943-7889.0000594.

Yan, J. et al., 2019. Concrete crack detection and monitoring using a capacitive dense sensor array. *Sensors,* [e-journal] 19(8), p. 1843. http://doi.org/10.3390/s19081843

Yeh, P. and Liu, P., 2009. Imaging of internal cracks in concrete structures using the surface rendering technique. *NDT and E International ,* [e-journal] 42(3)*,* pp. 181-187. http://doi.org/10.1016/j.ndteint.2008.09.003.

Zeng, Z., Chen, W. and Wang, W., 2019. A numerical mesoscopic method for simulating mechanical properties of fiber reinforced concrete. *In International Conference on Computational and Experiment Engineering and Sciences,* [e-journal] pp. 803-812. https://doi.org/10.1007/978-3-030-27053-7_68.

APPENDICES

APPENDIX A: Delta Method Result from Microsoft Excel

Table A.1: Stochastic Model – 15 cm crack.

Set	Input (m)	Output (m)	Time (s)	Velocity (m/s)	Depth(Try and error) (m)
1	0	0	0	0	NO CRACK
2	0.15	0.15	1.18E-04	3585.228	0.15
3	0.15	0.45	1.92E-04	3585.228	0.15
4	0.1677	0.5031	2.25E-04	3338.559	0.15
5	0.2121	0.6364	2.43E-04	3765.568	0.15
6	0.3354	0.3354	2.11E-04	3476.793	0.15
7	0.6	0	1.65E-04	3630.622	NO CRACK
8	0.3	0	8.26E-05	3630.622	NO CRACK
9	0.2121	0.2121	1.43E-04	3585.228	0.15
10	0.15	0.15	1.18E-04	3585.228	0.15
11	0	0	0	0	NO CRACK
12	0.3	0	8.36767E-05	3585.228	NO CRACK
13	0.4243	0	0.000114701	3699.193	NO CRACK
14	0.6708	0	0.000160205	4187.128	NO CRACK
15	0.6	0	0.000165172	3632.588	NO CRACK
16	0.3354	0.3354	1.96E-04	3757.712	0.15
17	0.2121	0.2121	1.39E-04	3742.532	0.15
18	0.3	0	8.02E-05	3742.532	NO CRACK
19	0.45	0.15	1.92E-04	3585.228	0.15
20	0.3	0	8.36767E-05	3585.228	NO CRACK
21	0	0	0	0	NO CRACK
22	0.3	0	8.18706E-05	3664.317	NO CRACK
23	0.6	0	0.000163741	3664.317	NO CRACK
24	0.6708	0	0.000168745	3975.226	NO CRACK
25	0.6364	0.2121	2.47E-04	3695.125	0.15
26	0.5031	0.1677	1.82E-04	4115.82	0.15

Table A.1 (Continued)

Set	Input (m)	Output (m)	Time (s)	Velocity (m/s)	Depth(Try and error) (m)
27	0.4243	0	1.03E-04	4115.82	NO CRACK
28	0.5031	0.1677	2.25E-04	3338.559	0.15
29	0.4243	0	0.000114701	3699.193	NO CRACK
30	0.3	0	8.18706E-05	3664.317	NO CRACK
31	0	0	0	0	NO CRACK
32	0.3	0	8.18706E-05	3664.317	NO CRACK
33	0.4243	0	0.000114835	3694.864	NO CRACK
34	0.5031	0.1677	2.31E-04	3251.206	0.15
35	0.45	0.15	1.8583619	3693.972	0.15
36	0.3	0	8.12134E-05	3693.972	NO CRACK
37	0.6364	0.2121	2.43E-04	3765.568	0.15
38	0.6708	0	0.000160205	4187.128	NO CRACK
39	0.6	0	0.000163741	3664.317	NO CRACK
40	0.3	0	8.18706E-05	3664.317	NO CRACK
41	0	0	0	0	NO CRACK
42	0.3	0	8.46828E-05	3542.632	NO CRACK
43	0.45	0.15	1.94E-04	3542.632	0.15
44	0.5031	0.1677	1.89E-04	3959.45	0.15
45	0.4243	0	1.07E-04	3959.45	NO CRACK
46	0.3354	0.3354	2.11E-04	3476.793	0.15
47	0.6	0	0.000165172	3632.588	NO CRACK
48	0.6708	0	0.000168745	3975.226	NO CRACK
49	0.4243	0	0.000114835	3694.864	NO CRACK
50	0.3	0	8.46828E-05	3542.632	NO CRACK
51	0	0	0	0	NO CRACK
52	0.15	0.15	1.20E-04	3542.632	0.15
53	0.2121	0.2121	1.44E-04	3609.749	0.15

Table A.1 (Continued)

Set	Input (m)	Output (m)	Time (s)	Velocity (m/s)	Depth(Try and error) (m)
54	0.3	0	8.31E-05	3609.749	NOCRACK
55	0.6	0	0.000165261	3630.622	NO CRACK
56	0.3354	0.3354	1.96E-04	3757.712	0.15
57	0.2121	0.6364	2.47E-04	3695.125	0.15
58	0.1677	0.5031	2.31E-04	3251.206	0.15
59	0.15	0.45	1.94E-04	3542.632	0.15
60	0.15	0.15	1.20E-04	3542.632	0.15
61	0	0	0	0	NO CRACK
62	0.3	0	8.26305E-05	3630.622	NO CRACK
63	0.2121	0.2121	1.43E-04	3630.622	0.15
64	0.3	0	8.26305E-05	3630.622	NO CRACK
65	0.2121	0.2121	1.39E-04	3742.532	0.15
66	0.1677	0.5031	1.82E-04	4115.82	0.15
67	0.15	0.45	1.86E-04	3693.972	0.15
68	0.1677	0.5031	1.89E-04	3959.45	0.15
69	0.2121	0.2121	1.44E-04	3609.749	0.15
70	0.3	0	8.26305E-05	3630.622	NO CRACK
71	0	0	0	0	NO CRACK
72	0.15	0.15	1.17E-04	3585.228	0.15
73	0.2121	0.2121	1.43E-04	3585.228	0.15
74	0.3	0	8.02E-05	3742.532	NO CRACK
75	0.4243	0	1.03E-04	4115.82	NO CRACK
76	0.3	0	8.12134E-05	3693.972	NO CRACK
77	0.4243	0	1.07E-04	3959.45	NO CRACK
78	0.3	0	8.31E-05	3609.749	NOCRACK
79	0.2121	0.2121	1.43E-04	3630.622	0.15
80	0.15	0.15	1.17E-04	3585.228	0.15
81	0	0	0	0	0.15

Table A.2: Stochastic Model – 10 cm crack.

Set	Input (m)	Output (m)	Time (s)	Velocity (m/s)	Depth(Try and error) (m)
1	0	0	0	0	NO CRACK
2	0.15	0.15	1.01E-04	3585.228	0.1
3	0.15	0.45	1.79E-04	3585.228	0.1
4	0.1677	0.5031	2.12E-04	3338.559	0.1
5	0.2121	0.6364	2.33E-04	3765.568	0.1
6	0.3354	0.3354	2.01E-04	3476.793	0.1
7	0.6	0	1.65E-04	3630.622	NO CRACK
8	0.3	0	8.26E-05	3630.622	NO CRACK
9	0.2121	0.2121	1.29E-04	3585.228	0.1
10	0.15	0.15	1.01E-04	3585.228	0.1
11	0	0	0	0	NO CRACK
12	0.3	0	8.36767E-05	3585.228	NO CRACK
13	0.4243	0	0.000114701	3699.193	NO CRACK
14	0.6708	0	0.000160205	4187.128	NO CRACK
15	0.6	0	0.000165172	3632.588	NO CRACK
16	0.3354	0.3354	1.86E-04	3757.712	0.1
17	0.2121	0.2121	1.25E-04	3742.532	0.1
18	0.3	0	8.02E-05	3742.532	NO CRACK
19	0.45	0.15	1.79E-04	3585.228	0.1
20	0.3	0	8.36767E-05	3585.228	NO CRACK
21	0	0	0	0	NO CRACK
22	0.3	0	8.18706E-05	3664.317	NO CRACK
23	0.6	0	0.000163741	3664.317	NO CRACK
24	0.6708	0	0.000168745	3975.226	NO CRACK
25	0.6364	0.2121	2.38E-04	3695.125	0.1
26	0.5031	0.1677	1.72E-04	4115.82	0.1
27	0.4243	0	1.03E-04	4115.82	NO CRACK
28	0.5031	0.1677	2.12E-04	3338.559	0.1
29	0.4243	0	0.000114701	3699.193	NO CRACK

Table A.2 (Continued)

Set	Input (m)	Output (m)	Time (s)	Velocity (m/s)	Depth(Try and error) (m)
30	0.3	0	8.18706E-05	3664.317	NO CRACK
31	0	0	0	0	NO CRACK
32	0.3	0	8.18706E-05	3664.317	NO CRACK
33	0.4243	0	0.000114835	3694.864	NO CRACK
34	0.5031	0.1677	2.18E-04	3251.206	0.1
35	0.45	0.15	1.74E-04	3693.972	0.1
36	0.3	0	8.12E-05	3693.972	NO CRACK
37	0.6364	0.2121	2.33E-04	3765.568	0.1
38	0.6708	0	0.000160205	4187.128	NO CRACK
39	0.6	0	0.000163741	3664.317	NO CRACK
40	0.3	0	8.18706E-05	3664.317	NO CRACK
41	0	0	0	0	NO CRACK
42	0.3	0	8.46828E-05	3542.632	NO CRACK
43	0.45	0.15	1.81E-04	3542.632	0.1
44	0.5031	0.1677	1.79E+00	3959.45	0.1
45	0.4243	0	1.07E-04	3959.45	NO CRACK
46	0.3354	0.3354	2.01E-04	3476.793	0.1
47	0.6	0	0.000165172	3632.588	NO CRACK
48	0.6708	0	0.000168745	3975.226	NO CRACK
49	0.4243	0	0.000114835	3694.864	NO CRACK
50	0.3	0	8.46828E-05	3542.632	NO CRACK
51	0	0	0	0	NO CRACK
52	0.15	0.15	1.02E-04	3542.632	0.1
53	0.2121	0.2121	1.30E-04	3609.749	0.1
54	0.3	0	8.31E-05	3609.749	NOCRACK
55	0.6	0	0.000165261	3630.622	NO CRACK
56	0.3354	0.3354	1.86E-04	3757.712	0.1
57	0.2121	0.6364	2.38E-04	3695.125	0.1

Table A.2 (Continued)

Set	Input (m)	Output (m)	Time (s)	Velocity (m/s)	Depth(Try and error) (m)
58	0.1677	0.5031	2.18E-04	3251.206	0.1
59	0.15	0.45	1.81E-04	3542.632	0.1
60	0.15	0.15	1.02E-04	3542.632	0.1
61	0	0	0	0	NO CRACK
62	0.3	0	8.26305E-05	3630.622	NO CRACK
63	0.2121	0.2121	1.29E-04	3630.622	0.1
64	0.3	0	8.26305E-05	3630.622	NO CRACK
65	0.2121	0.2121	1.25E-04	3742.532	0.1
66	0.1677	0.5031	1.72E-04	4115.82	0.1
67	0.15	0.45	1.74E-04	3693.972	0.1
68	0.1677	0.5031	1.79E-04	3959.45	0.1
69	0.2121	0.2121	1.30E-04	3609.749	0.1
70	0.3	0	8.26305E-05	3630.622	NO CRACK
71	0	0	0	0	NO CRACK
72	0.15	0.15	9.92E-05	3585.228	0.1
73	0.2121	0.2121	1.29E-04	3585.228	0.1
74	0.3	0	8.02E-05	3742.532	NO CRACK
75	0.4243	0	1.03E-04	4115.82	NO CRACK
76	0.3	0	8.12E-05	3693.972	NO CRACK
77	0.4243	0	1.07E-04	3959.45	NO CRACK
78	0.3	0	8.31E-05	3609.749	NOCRACK
79	0.2121	0.2121	1.29E-04	3630.622	0.1
80	0.15	0.15	9.92E-05	3585.228	0.1
81	0	0	0	0	0.1

Table A.3: Stochastic Model – 12.5 cm void.

Set	Input (m)	Output (m)	Time (s)	Velocity (m/s)	Depth(Try and error) (m)
1	0	0	0	0	NO CRACK
2	0.15	0.15	1.09E-04	3585.228	0.125
3	0.15	0.45	1.85E-04	3585.228	0.125
4	0.1677	0.5031	2.18E-04	3338.559	0.125
5	0.2121	0.6364	2.38E-04	3765.568	0.125
6	0.3354	0.3354	2.06E-04	3476.793	0.125
7	0.6	0	1.65E-04	3630.622	NO CRACK
8	0.3	0	8.26E-05	3630.622	NO CRACK
9	0.2121	0.2121	1.35E-04	3585.228	0.125
10	0.15	0.15	1.09E-04	3585.228	0.125
11	0	0	0	0	NO CRACK
12	0.3	0	8.36767E-05	3585.228	NO CRACK
13	0.4243	0	0.000114701	3699.193	NO CRACK
14	0.6708	0	0.000160205	4187.128	NO CRACK
15	0.6	0	0.000165172	3632.588	NO CRACK
16	0.3354	0.3354	1.91E-04	3757.712	0.125
17	0.2121	0.2121	1.32E-04	3742.532	0.125
18	0.3	0	8.02E-05	3742.532	NO CRACK
19	0.45	0.15	1.85E-04	3585.228	0.125
20	0.3	0	8.36767E-05	3585.228	NO CRACK
21	0	0	0	0	NO CRACK
22	0.3	0	8.18706E-05	3664.317	NO CRACK
23	0.6	0	0.000163741	3664.317	NO CRACK
24	0.6708	0	0.000168745	3975.226	NO CRACK
25	0.6364	0.2121	2.42E-04	3695.125	0.125
26	0.5031	0.1677	1.77E-04	4115.82	0.125
27	0.4243	0	1.03E-04	4115.82	NO CRACK
28	0.5031	0.1677	2.18E-04	3338.559	0.125
29	0.4243	0	0.000114701	3699.193	NO CRACK

Table A.3 (Continued)

Set	Input (m)	Output (m)	Time (s)	Velocity (m/s)	Depth(Try and error) (m)
30	0.3	0	8.18706E-05	3664.317	NO CRACK
31	0	0	0	0	NO CRACK
32	0.3	0	8.18706E-05	3664.317	NO CRACK
33	0.4243	0	0.000114835	3694.864	NO CRACK
34	0.5031	0.1677	2.24E-04	3251.206	0.125
35	0.45	0.15	1.79E-04	3693.972	0.125
36	0.3	0	8.12E-05	3693.972	NO CRACK
37	0.6364	0.2121	2.38E-04	3765.568	0.125
38	0.6708	0	0.000160205	4187.128	NO CRACK
39	0.6	0	0.000163741	3664.317	NO CRACK
40	0.3	0	8.18706E-05	3664.317	NO CRACK
41	0	0	0	0	NO CRACK
42	0.3	0	8.46828E-05	3542.632	NO CRACK
43	0.45	0.15	1.87E-04	3542.632	0.125
44	0.5031	0.1677	1.84E-04	3959.45	0.125
45	0.4243	0	1.07E-04	3959.45	NO CRACK
46	0.3354	0.3354	2.06E-04	3476.793	0.125
47	0.6	0	0.000165172	3632.588	NO CRACK
48	0.6708	0	0.000168745	3975.226	NO CRACK
49	0.4243	0	0.000114835	3694.864	NO CRACK
50	0.3	0	8.46828E-05	3542.632	NO CRACK
51	0	0	0	0	NO CRACK
52	0.15	0.15	1.10E-04	3542.632	0.125
53	0.2121	0.2121	1.36E-04	3609.749	0.125
54	0.3	0	8.31E-05	3609.749	NOCRACK
55	0.6	0	0.000165261	3630.622	NO CRACK
56	0.3354	0.3354	1.91E-04	3757.712	0.125
57	0.2121	0.6364	2.42E-04	3695.125	0.125

Table A.3 (Continued)

Set	Input (m)	Output (m)	Time (s)	Velocity (m/s)	Depth(Try and error) (m)
58	0.1677	0.5031	2.24E-04	3251.206	0.125
59	0.15	0.45	1.87E-04	3542.632	0.125
60	0.15	0.15	1.10E-04	3542.632	0.125
61	0	0	0	0	NO CRACK
62	0.3	0	8.26305E-05	3630.622	NO CRACK
63	0.2121	0.2121	1.36E-04	3630.622	0.125
64	0.3	0	8.26305E-05	3630.622	NO CRACK
65	0.2121	0.2121	1.32E-04	3742.532	0.125
66	0.1677	0.5031	1.77E-04	4115.82	0.125
67	0.15	0.45	1.79E-04	3693.972	0.125
68	0.1677	0.5031	1.84E-04	3959.45	0.125
69	0.2121	0.2121	1.36E-04	3609.749	0.125
70	0.3	0	8.26305E-05	3630.622	NO CRACK
71	0	0	0	0	NO CRACK
72	0.15	0.15	1.07E-04	3585.228	0.125
73	0.2121	0.2121	1.35E-04	3585.228	0.125
74	0.3	0	8.02E-05	3742.532	NO CRACK
75	0.4243	0	1.03E-04	4115.82	NO CRACK
76	0.3	0	8.12E-05	3693.972	NO CRACK
77	0.4243	0	1.07E-04	3959.45	NO CRACK
78	0.3	0	8.31E-05	3609.749	NOCRACK
79	0.2121	0.2121	1.36E-04	3630.622	0.125
80	0.15	0.15	1.07E-04	3585.228	0.125
81	0	0	0	0	0.125

Table A.4: Deterministic Model – 15 cm crack.

Set	Input (m)	Output (m)	Time (s)	Velocity (m/s)	Depth(Try and error) (m)
1	0	0	0	0	NO CRACK
2	0.15	0.15	1.20E-04	3585.228	0.15
3	0.15	0.45	1.94E-04	3585.228	0.15
4	0.1677	0.5031	2.12E-04	3338.559	0.15
5	0.2121	0.6364	2.58E-04	3765.568	0.15
6	0.3354	0.3354	2.08E-04	3476.793	0.15
7	0.6	0	1.70E-04	3630.622	NO CRACK
8	0.3	0	8.48E-05	3630.622	NO CRACK
9	0.2121	0.2121	1.47E-04	3585.228	0.15
10	0.15	0.15	1.20E-04	3585.228	0.15
11	0	0	0	0	NO CRACK
12	0.3	0	8.48464E-05	3585.228	NO CRACK
13	0.4243	0	0.000120001	3699.193	NO CRACK
14	0.6708	0	1.90E-04	4187.128	NO CRACK
15	0.6	0	0.000169693	3632.588	NO CRACK
16	0.3354	0.3354	2.08E-04	3757.712	0.15
17	0.2121	0.2121	1.47E-04	3742.532	0.15
18	0.3	0	8.48E-05	3742.532	NO CRACK
19	0.45	0.15	1.94E-04	3585.228	0.15
20	0.3	0	8.48464E-05	3585.228	NO CRACK
21	0	0	0	0	NO CRACK
22	0.3	0	8.48464E-05	3664.317	NO CRACK
23	0.6	0	0.000169693	3664.317	NO CRACK
24	0.6708	0	0.000189717	3975.226	NO CRACK
25	0.6364	0.2121	2.58E-04	3695.125	0.15
26	0.5031	0.1677	2.12E-04	4115.82	0.15
27	0.4243	0	1.20E-04	4115.82	NO CRACK
28	0.5031	0.1677	2.12E-04	3338.559	0.15
29	0.4243	0	0.000120001	3699.193	NO CRACK

Table A.4 (Continued)

Set	Input (m)	Output (m)	Time (s)	Velocity (m/s)	Depth(Try and error) (m)
30	0.3	0	8.48464E-05	3664.317	NO CRACK
31	0	0	0	0	NO CRACK
32	0.3	0	8.48464E-05	3664.317	NO CRACK
33	0.4243	0	0.000120001	3694.864	NO CRACK
34	0.5031	0.1677	2.12E-04	3251.206	0.15
35	0.45	0.15	1.94E-04	3693.972	0.15
36	0.3	0	8.48E-05	3693.972	NO CRACK
37	0.6364	0.2121	2.58E-04	3765.568	0.15
38	0.6708	0	0.000189717	4187.128	NO CRACK
39	0.6	0	0.000169693	3664.317	NO CRACK
40	0.3	0	8.48464E-05	3664.317	NO CRACK
41	0	0	0	0	NO CRACK
42	0.3	0	8.48464E-05	3542.632	NO CRACK
43	0.45	0.15	1.94E-04	3542.632	0.15
44	0.5031	0.1677	2.12E-04	3959.45	0.15
45	0.4243	0	1.20E-04	3959.45	NO CRACK
46	0.3354	0.3354	2.08E-04	3476.793	0.15
47	0.6	0	1.70E-04	3632.588	NO CRACK
48	0.6708	0	1.90E-04	3975.226	NO CRACK
49	0.4243	0	1.20E-04	3694.864	NO CRACK
50	0.3	0	8.48E-05	3542.632	NO CRACK
51	0	0	0	0	NO CRACK
52	0.15	0.15	1.20E-04	3542.632	0.15
53	0.2121	0.2121	1.47E-04	3609.749	0.15
54	0.3	0	8.48E-05	3609.749	NOCRACK
55	0.6	0	1.70E-04	3630.622	NO CRACK
56	0.3354	0.3354	2.08E-04	3757.712	0.15
57	0.2121	0.6364	2.58E-04	3695.125	0.15

Table A.4 (Continued)

Set	Input (m)	Output (m)	Time (s)	Velocity (m/s)	Depth(Try and error) (m)
58	0.1677	0.5031	2.12E-04	3251.206	0.15
59	0.15	0.45	1.94E-04	3542.632	0.15
60	0.15	0.15	1.20E-04	3542.632	0.15
61	0	0	0	0	NO CRACK
62	0.3	0	8.48464E-05	3630.622	NO CRACK
63	0.2121	0.2121	1.47E-04	3630.622	0.15
64	0.3	0	8.48464E-05	3630.622	NO CRACK
65	0.2121	0.2121	1.47E-04	3742.532	0.15
66	0.1677	0.5031	2.12E-04	4115.82	0.15
67	0.15	0.45	1.94E-04	3693.972	0.15
68	0.1677	0.5031	2.12E-04	3959.45	0.15
69	0.2121	0.2121	1.47E-04	3609.749	0.15
70	0.3	0	8.48464E-05	3630.622	NO CRACK
71	0	0	0	0	NO CRACK
72	0.15	0.15	1.20E-04	3585.228	0.15
73	0.2121	0.2121	1.47E-04	3585.228	0.15
74	0.3	0	8.48464E-05	3742.532	NO CRACK
75	0.4243	0	0.000120001	4115.82	NO CRACK
76	0.3	0	8.48464E-05	3693.972	NO CRACK
77	0.4243	0	0.000120001	3959.45	NO CRACK
78	0.3	0	8.48464E-05	3609.749	NOCRACK
79	0.2121	0.2121	1.47E-04	3630.622	0.15
80	0.15	0.15	1.20E-04	3585.228	0.15
81	0	0	0	0	0.15

Table A.5: Deterministic Model – 10 cm crack.

Set	Input (m)	Output (m)	Time (s)	Velocity (m/s)	Depth(Try and error) (m)
1	0	0	0	0	NO CRACK
2	0.15	0.15	1.02E-04	3585.228	0.1
3	0.15	0.45	1.81E-04	3585.228	0.1
4	0.1677	0.5031	2.00E-04	3338.559	0.1
5	0.2121	0.6364	2.49E-04	3765.568	0.1
6	0.3354	0.3354	1.98E-04	3476.793	0.1
7	0.6	0	1.70E-04	3630.622	NO CRACK
8	0.3	0	8.48E-05	3630.622	NO CRACK
9	0.2121	0.2121	1.33E-04	3585.228	0.1
10	0.15	0.15	1.02E-04	3585.228	0.1
11	0	0	0	0	NO CRACK
12	0.3	0	8.48464E-05	3585.228	NO CRACK
13	0.4243	0	0.000120001	3699.193	NO CRACK
14	0.6708	0	1.90E-04	4187.128	NO CRACK
15	0.6	0	0.000169693	3632.588	NO CRACK
16	0.3354	0.3354	1.98E-04	3757.712	0.1
17	0.2121	0.2121	1.33E-04	3742.532	0.1
18	0.3	0	8.48E-05	3742.532	NO CRACK
19	0.45	0.15	1.81E-04	3585.228	0.1
20	0.3	0	8.48464E-05	3585.228	NO CRACK
21	0	0	0	0	NO CRACK
22	0.3	0	8.48464E-05	3664.317	NO CRACK
23	0.6	0	0.000169693	3664.317	NO CRACK
24	0.6708	0	0.000189717	3975.226	NO CRACK
25	0.6364	0.2121	2.49E-04	3695.125	0.1
26	0.5031	0.1677	2.00E-04	4115.82	0.1
27	0.4243	0	1.20E-04	4115.82	NO CRACK
28	0.5031	0.1677	2.00E-04	3338.559	0.1
29	0.4243	0	0.000120001	3699.193	NO CRACK

Table A.5 (Continued)

Set	Input (m)	Output (m)	Time (s)	Velocity (m/s)	Depth(Try and error) (m)
30	0.3	0	8.48464E-05	3664.317	NO CRACK
31	0	0	0	0	NO CRACK
32	0.3	0	8.48464E-05	3664.317	NO CRACK
33	0.4243	0	0.000120001	3694.864	NO CRACK
34	0.5031	0.1677	2.00E-04	3251.206	0.1
35	0.45	0.15	1.81E-04	3693.972	0.1
36	0.3	0	8.48E-05	3693.972	NO CRACK
37	0.6364	0.2121	2.49E-04	3765.568	0.1
38	0.6708	0	0.000189717	4187.128	NO CRACK
39	0.6	0	0.000169693	3664.317	NO CRACK
40	0.3	0	8.48464E-05	3664.317	NO CRACK
41	0	0	0	0	NO CRACK
42	0.3	0	8.48464E-05	3542.632	NO CRACK
43	0.45	0.15	1.81E-04	3542.632	0.1
44	0.5031	0.1677	2.00E-04	3959.45	0.1
45	0.4243	0	1.20E-04	3959.45	NO CRACK
46	0.3354	0.3354	1.98E-04	3476.793	0.1
47	0.6	0	1.70E-04	3632.588	NO CRACK
48	0.6708	0	1.90E-04	3975.226	NO CRACK
49	0.4243	0	1.20E-04	3694.864	NO CRACK
50	0.3	0	8.48E-05	3542.632	NO CRACK
51	0	0	0	0	NO CRACK
52	0.15	0.15	1.02E-04	3542.632	0.1
53	0.2121	0.2121	1.33E-04	3609.749	0.1
54	0.3	0	8.48E-05	3609.749	NOCRACK
55	0.6	0	1.70E-04	3630.622	NO CRACK
56	0.3354	0.3354	1.98E-04	3757.712	0.1
57	0.2121	0.6364	2.49E-04	3695.125	0.1

Table A.5 (Continued)

Set	Input (m)	Output (m)	Time (s)	Velocity (m/s)	Depth(Try and error) (m)
58	0.1677	0.5031	2.00E-04	3251.206	0.1
59	0.15	0.45	1.81E-04	3542.632	0.1
60	0.15	0.15	1.02E-04	3542.632	0.1
61	0	0	0	0	NO CRACK
62	0.3	0	8.48464E-05	3630.622	NO CRACK
63	0.2121	0.2121	1.33E-04	3630.622	0.1
64	0.3	0	8.48464E-05	3630.622	NO CRACK
65	0.2121	0.2121	1.33E-04	3742.532	0.1
66	0.1677	0.5031	2.00E-04	4115.82	0.1
67	0.15	0.45	1.81E-04	3693.972	0.1
68	0.1677	0.5031	2.00E-04	3959.45	0.1
69	0.2121	0.2121	1.33E-04	3609.749	0.1
70	0.3	0	8.48464E-05	3630.622	NO CRACK
71	0	0	0	0	NO CRACK
72	0.15	0.15	1.02E-04	3585.228	0.1
73	0.2121	0.2121	1.33E-04	3585.228	0.1
74	0.3	0	8.48464E-05	3742.532	NO CRACK
75	0.4243	0	0.000120001	4115.82	NO CRACK
76	0.3	0	8.48464E-05	3693.972	NO CRACK
77	0.4243	0	0.000120001	3959.45	NO CRACK
78	0.3	0	8.48464E-05	3609.749	NOCRACK
79	0.2121	0.2121	1.33E-04	3630.622	0.1
80	0.15	0.15	1.02E-04	3585.228	0.1
81	0	0	0	0	0.1

Table A.6: Deterministic Model – 12.5 cm Void.

Set	Input (m)	Output (m)	Time (s)	Velocity (m/s)	Depth(Try and error) (m)
1	0	0	0	0	NO CRACK
2	0.15	0.15	1.10E-04	3585.228	0.125
3	0.15	0.45	1.87E-04	3585.228	0.125
4	0.1677	0.5031	2.06E-04	3338.559	0.125
5	0.2121	0.6364	2.53E-04	3765.568	0.125
6	0.3354	0.3354	2.02E-04	3476.793	0.125
7	0.6	0	1.70E-04	3630.622	NO CRACK
8	0.3	0	8.48E-05	3630.622	NO CRACK
9	0.2121	0.2121	1.39E-04	3585.228	0.125
10	0.15	0.15	1.10E-04	3585.228	0.125
11	0	0	0	0	NO CRACK
12	0.3	0	8.48464E-05	3585.228	NO CRACK
13	0.4243	0	0.000120001	3699.193	NO CRACK
14	0.6708	0	1.90E-04	4187.128	NO CRACK
15	0.6	0	0.000169693	3632.588	NO CRACK
16	0.3354	0.3354	2.02E-04	3757.712	0.125
17	0.2121	0.2121	1.39E-04	3742.532	0.125
18	0.3	0	8.48E-05	3742.532	NO CRACK
19	0.45	0.15	1.87E-04	3585.228	0.125
20	0.3	0	8.48464E-05	3585.228	NO CRACK
21	0	0	0	0	NO CRACK
22	0.3	0	8.48464E-05	3664.317	NO CRACK
23	0.6	0	0.000169693	3664.317	NO CRACK
24	0.6708	0	0.000189717	3975.226	NO CRACK
25	0.6364	0.2121	2.53E-04	3695.125	0.125
26	0.5031	0.1677	2.06E-04	4115.82	0.125
27	0.4243	0	1.20E-04	4115.82	NO CRACK
28	0.5031	0.1677	2.06E-04	3338.559	0.125
29	0.4243	0	0.000120001	3699.193	NO CRACK

Table A.6 (Continued)

Set	Input (m)	Output (m)	Time (s)	Velocity (m/s)	Depth(Try and error) (m)
30	0.3	0	8.48464E-05	3664.317	NO CRACK
31	0	0	0	0	NO CRACK
32	0.3	0	8.48464E-05	3664.317	NO CRACK
33	0.4243	0	0.000120001	3694.864	NO CRACK
34	0.5031	0.1677	2.06E-04	3251.206	0.125
35	0.45	0.15	1.87E-04	3693.972	0.125
36	0.3	0	8.48E-05	3693.972	NO CRACK
37	0.6364	0.2121	2.53E-04	3765.568	0.125
38	0.6708	0	0.000189717	4187.128	NO CRACK
39	0.6	0	0.000169693	3664.317	NO CRACK
40	0.3	0	8.48464E-05	3664.317	NO CRACK
41	0	0	0	0	NO CRACK
42	0.3	0	8.48464E-05	3542.632	NO CRACK
43	0.45	0.15	1.87E-04	3542.632	0.125
44	0.5031	0.1677	2.06E-04	3959.45	0.125
45	0.4243	0	1.20E-04	3959.45	NO CRACK
46	0.3354	0.3354	2.02E-04	3476.793	0.125
47	0.6	0	1.70E-04	3632.588	NO CRACK
48	0.6708	0	1.90E-04	3975.226	NO CRACK
49	0.4243	0	1.20E-04	3694.864	NO CRACK
50	0.3	0	8.48E-05	3542.632	NO CRACK
51	0	0	0	0	NO CRACK
52	0.15	0.15	1.10E-04	3542.632	0.125
53	0.2121	0.2121	1.39E-04	3609.749	0.125
54	0.3	0	8.48E-05	3609.749	NOCRACK
55	0.6	0	1.70E-04	3630.622	NO CRACK
56	0.3354	0.3354	2.02E-04	3757.712	0.125
57	0.2121	0.6364	2.53E-04	3695.125	0.125

111

Table A.6 (Continued)

Set	Input (m)	Output (m)	Time (s)	Velocity (m/s)	Depth(Try and error) (m)
58	0.1677	0.5031	2.06E-04	3251.206	0.125
59	0.15	0.45	1.87E-04	3542.632	0.125
60	0.15	0.15	1.10E-04	3542.632	0.125
61	0	0	0	0	NO CRACK
62	0.3	0	8.48464E-05	3630.622	NO CRACK
63	0.2121	0.2121	1.39E-04	3630.622	0.125
64	0.3	0	8.48464E-05	3630.622	NO CRACK
65	0.2121	0.2121	1.39E-04	3742.532	0.125
66	0.1677	0.5031	2.06E-04	4115.82	0.125
67	0.15	0.45	1.87E-04	3693.972	0.125
68	0.1677	0.5031	2.06E-04	3959.45	0.125
69	0.2121	0.2121	1.39E-04	3609.749	0.125
70	0.3	0	8.48464E-05	3630.622	NO CRACK
71	0	0	0	0	NO CRACK
72	0.15	0.15	1.10E-04	3585.228	0.125
73	0.2121	0.2121	1.39E-04	3585.228	0.125
74	0.3	0	8.48464E-05	3742.532	NO CRACK
75	0.4243	0	0.000120001	4115.82	NO CRACK
76	0.3	0	8.48464E-05	3693.972	NO CRACK
77	0.4243	0	0.000120001	3959.45	NO CRACK
78	0.3	0	8.48464E-05	3609.749	NOCRACK
79	0.2121	0.2121	1.39E-04	3630.622	0.125
80	0.15	0.15	1.10E-04	3585.228	0.125
81	0	0	0	0	0.125

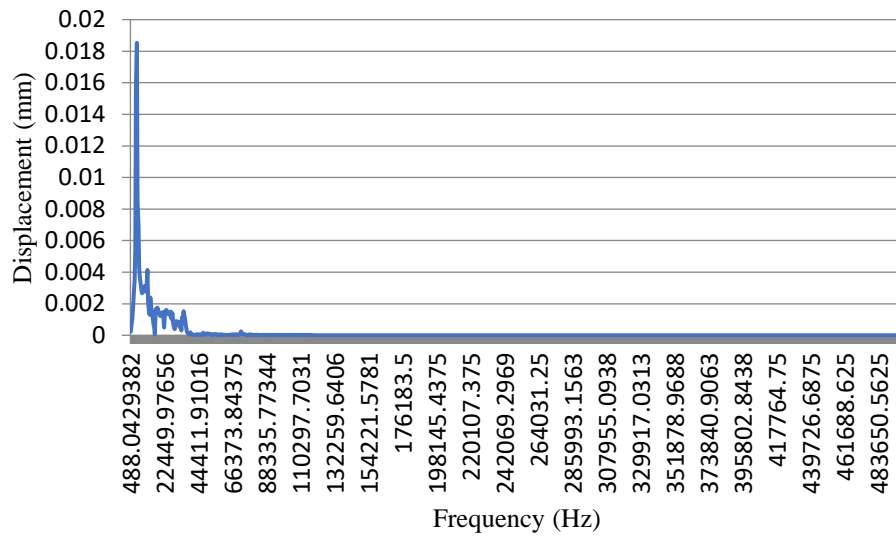**APPENDIX B: Fast Fourier Transform Graph**

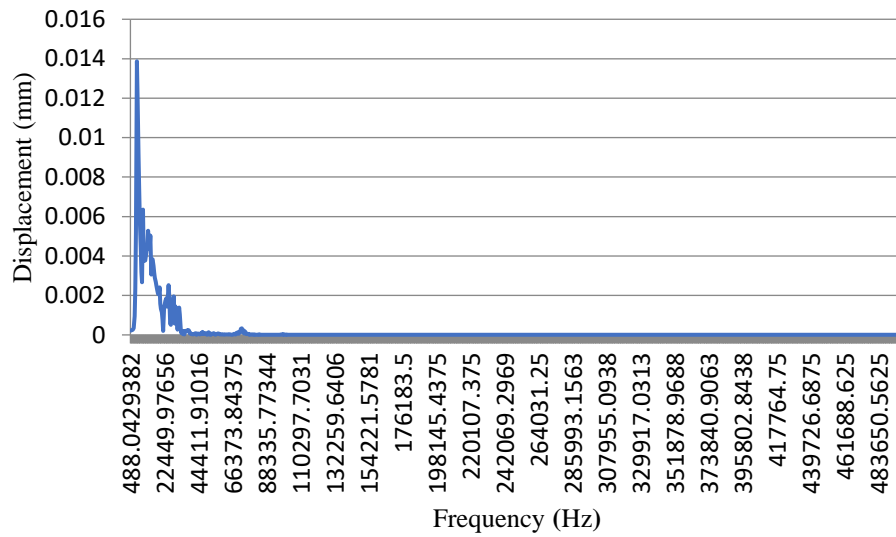Figure B.1: FFT graph for 10 cm Crack Model (Deterministic).

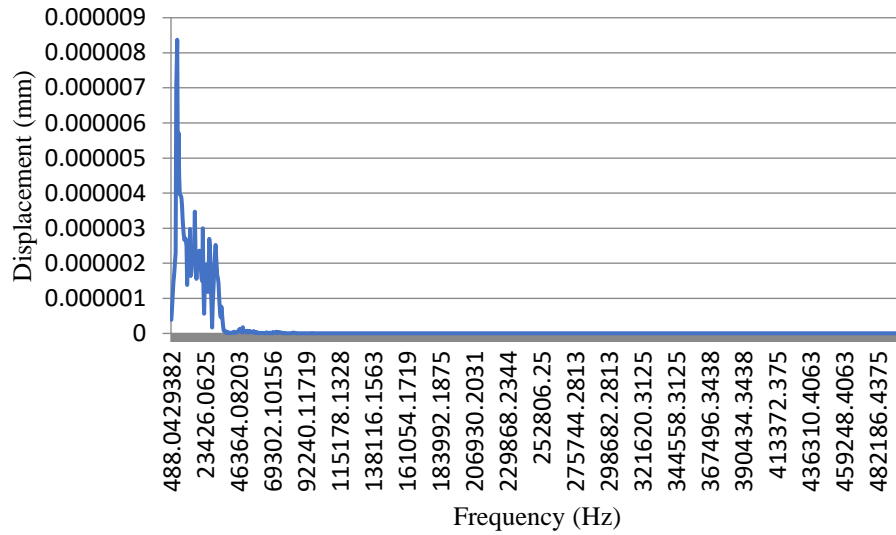Figure B.2: FFT graph for 10 cm Crack Model (Stochastic).

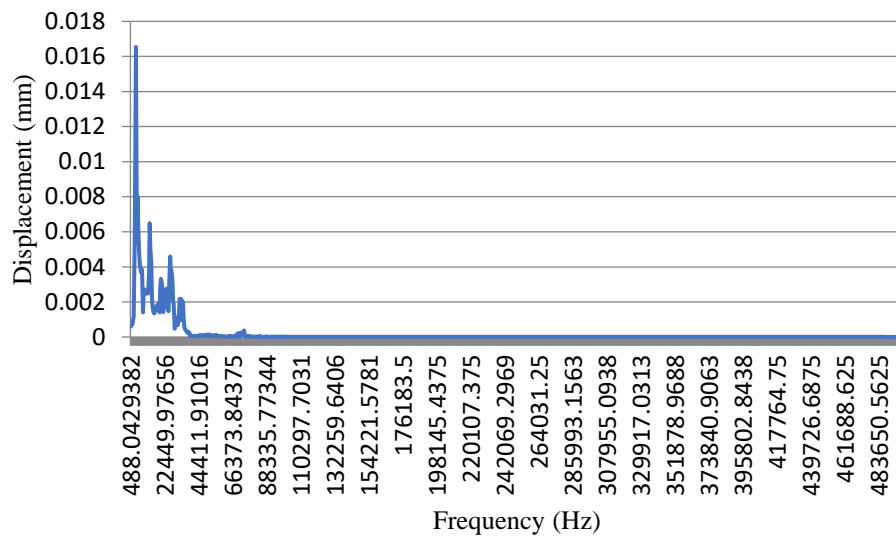Figure B.3: FFT graph for 15 cm Crack Model (Deterministic).

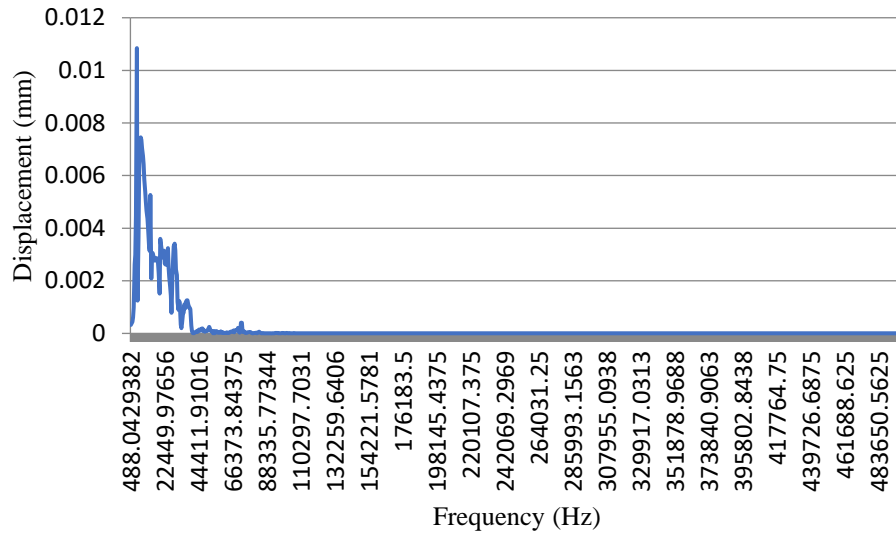Figure B.4: FFT graph for 15 cm Crack Model (Stochastic).

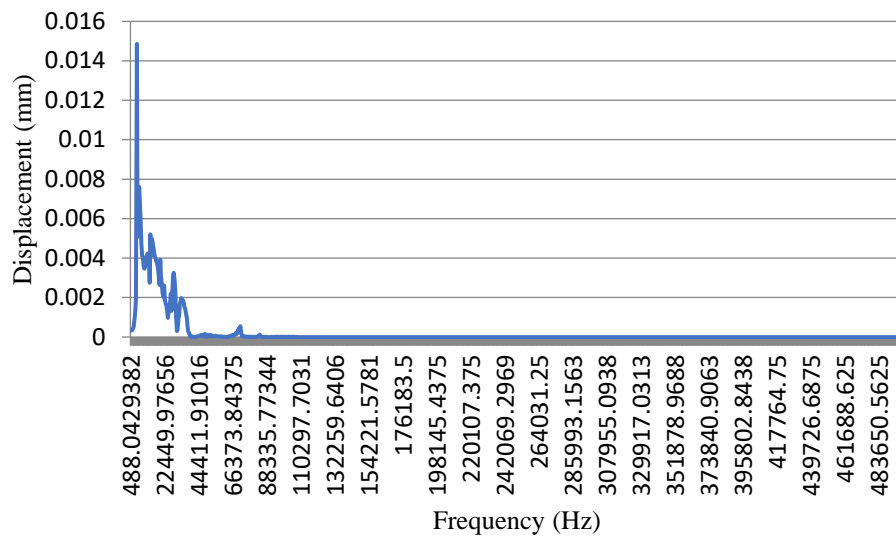Figure B.5: FFT graph for 12.5 cm Void Model (Deterministic).

Figure B.6: FFT graph for 12.5 cm Void Model (Stochastic).

APPENDIX C: Surface Tomography Function

```
7
8    import numpy as np
9    import pandas as pd
10   import matplotlib.pyplot as plt
11   import math
12   from numpy import genfromtxt
13
14   specimen = np.zeros((60,60))
15   s1=np.array([0,60])
16   s2=np.array([30,60])
17   s3=np.array([60,60])
18   s4=np.array([60,30])
19   s5=np.array([60,0])
20   s6=np.array([30,0])
21   s7=np.array([0,0])
22   s8=np.array([0,30]) #sensors
23
24   time_data = genfromtxt('fixdata.csv', delimiter=',')
25   stochastic_data = genfromtxt('file.csv', delimiter=',')
26   velocity = np.zeros((64,))
27
28
29   sensors = np.array([[[s1,s1],[s1,s2],[s1,s3],[s1,s4],[s1,s5],[s1,s6],[s1,s7],[s1,s8]],
30                       [[s2,s1],[s2,s2],[s2,s3],[s2,s4],[s2,s5],[s2,s6],[s2,s7],[s2,s8]],
31                       [[s3,s1],[s3,s2],[s3,s3],[s3,s4],[s3,s5],[s3,s6],[s3,s7],[s3,s8]],
32                       [[s4,s1],[s4,s2],[s4,s3],[s4,s4],[s4,s5],[s4,s6],[s4,s7],[s4,s8]],
33                       [[s5,s1],[s5,s2],[s5,s3],[s5,s4],[s5,s5],[s5,s6],[s5,s7],[s5,s8]],
34                       [[s6,s1],[s6,s2],[s6,s3],[s6,s4],[s6,s5],[s6,s6],[s6,s7],[s6,s8]],
35                       [[s7,s1],[s7,s2],[s7,s3],[s7,s4],[s7,s5],[s7,s6],[s7,s7],[s7,s8]],
36                       [[s8,s1],[s8,s2],[s8,s3],[s8,s4],[s8,s5],[s8,s6],[s8,s7],[s8,s8]]]) #sensorsarray
37
38   y = -1 #coordinate for grid cell
39   x = 0
40   gcell = 0
41
42   for horicell in specimen:
43       for verticell in specimen:
44           totallength = 0
45           y += 1
46           if y == 60:
47               y = 0
```

Figure C.1: Sample Environment in Spyder (Python)

```
---grid  43 ---coordinate of sensor from 3  to  4
[60 60]
[60 30]
location of grid 0       42
The value of a =  30.0
The value of c =  0.75
The value of b =  11.25
The value of da >> 60.0
(60.0, 45.0)
the value of db 3.0
0 ------- 19 ----- distance between point to sensor 62.6418390534633 ... 0.0
---grid  43 ---coordinate of sensor from 3  to  5
[60 60]
[60  0]
location of grid 0       42
The value of a =  60.0
The value of c =  0.5
The value of b =  15.0
The value of da >> 60.0
```

Figure C.2: Console for Check Condition